



**IAEA**

International Atomic Energy Agency

INDC(CCP)-0446

Distr. Web only

## **INDC International Nuclear Data Committee**

### **Study of the multiplication and kinetic effects of salt mixtures and salt blanket micromodels on thermal neutron spectra of heavy water MAKET facility:**

Yu. E. Titarenko

Institute for Theoretical and Experimental Physics (ITEP)

Co-authors: V.F. Batyaev, S.P. Borovlev, N.G. Gladkikh, M.M. Igumnov,

V.O. Legostaev, E.I. Karpikhin, V.N. Konev, Yu.T. Kushnerev,

V.I. Ryazhsky, V.G. Spiridonov, E.V. Chernyavsky, O.V. Shvedov

Institute for Theoretical and Experimental Physics (ITEP)

October 2009

Selected INDC documents may be downloaded in electronic form from  
*[http://www-nds.iaea.org/indc\\_sel.html](http://www-nds.iaea.org/indc_sel.html)* or sent as an e-mail attachment.  
Requests for hardcopy or e-mail transmittal should be directed to [services@iaeand.iaea.org](mailto:services@iaeand.iaea.org)  
or to:

Nuclear Data Section  
International Atomic Energy Agency  
Vienna International Centre  
PO Box 100  
A-1400 Vienna  
Austria

Printed by the IAEA in Austria

October 2009

## **Study of the multiplication and kinetic effects of salt mixtures and salt blanket micromodels on thermal neutron spectra of heavy water MAKET facility:**

Yu. E. Titarenko

Institute for Theoretical and Experimental Physics (ITEP)

Co-authors: V.F. Batyaev, S.P. Borovlev, N.G. Gladkikh, M.M. Igumnov,  
V.O. Legostaev, E.I. Karpikhin, V.N. Konev, Yu.T. Kushnerev,  
V.I. Ryazhsky, V.G. Spiridonov, E.V. Chernyavsky, O.V. Shvedov  
Institute for Theoretical and Experimental Physics (ITEP)

### Abstract

The main goal of the Project is to study and evaluate nuclear characteristics of materials and isotopes involved in processes of irradiated nuclear fuel transmutation. This principal task is subdivided into 9 subtasks subject to the neutron or proton source used, the type of the nuclear process under study, isotope collection, characteristics of which are to be investigated, etc. In the presented extract of the Project Activity report the measurements there were used the MAKET zero-power heavy-water reactor in the measurements there was employed a large set of minor actinide samples highly enriched with the main isotope. The samples were obtained with mass-separator SM-2 (VNIIEF).

At the heavy-water reactor MAKET (ITEP) there were measured multiplying and kinetic characteristics of salt mixtures basing on the spectra of fast and thermal neutrons. The salt mixtures of zirconium and sodium fluorides were available in salt blanket models (SBM) of cylindrical shape. There were measured the neutron spectra formed by this micro-model as well as the effective fission cross-sections of neptunium, plutonium, americium and curium isotopes caused by SBM neutrons. The neutron spectra in the measurement positions were determined from activation reaction rates.

Keywords: salt blanket, fluorides, transuranium isotopes, critical assembly, nuclear reactor, proton accelerator.

October 2009

## CONTENTS

<b>C -</b>	<b>STUDY OF THE REACTIVITY EFFECTS OF THE SALT BLANKET MICROMODELS USING THE MAKET FACILITY .....</b>	<b>4</b>
1.	General approach to determining the accuracy requirements of the minor actinide cross sections .....	4
2.	Formulation of the problem .....	4
3.	Experimental facility .....	7
4.	Description of the containers used to irradiate the experimental samples .....	14
5.	Formation and optimization of the fuel lattice .....	16
6.	The preparatory steps for the SBM to be mounted in the MAKET core and for heavy water to be chemically purified; monitoring of the heavy water state in the experiments .....	21
7.	Monitoring the MAKET facility power .....	28
8.	Meters .....	30
9.	The measured parameters .....	33
9.1	The $\gamma$ -spectrometry method .....	33
9.2	The SSNTD techniques .....	38
10.	Determination of the absolute power of the MAKET facility with the experimental lattices .....	39
11.	Experimental results .....	60
12.	Determination of neutron spectra in the SBM channels .....	65
13.	The computational model of the MAKET facility; the calculation results .....	68
14.	Comparison between the experimental and calculated reaction rates .....	74
15.	Certification of fuel .....	90
	References .....	92

## C - STUDY OF THE REACTIVITY EFFECTS OF THE SALT BLANKET MICROMODELS USING THE MAKET FACILITY

### 1. General approach to determining the accuracy requirements of the minor actinide cross sections

The accuracy requirements for the knowledge of the neutron cross sections of the minor actinides (MA) are determined by the scope of the tasks to be tackled, namely,

- knowledge of the spectrum-averaged cross sections of Np to 10%, Am to 15-20%, and Cm to 30-50% is quite sufficient when studying the radiation balance of nuclear power production and when predicting the radiation property variations in the irradiated fuel of thermal and fast reactors and in the fuel of ADS facilities;
- 5-10% accurate MA cross sections seem to be quite proper when designing nuclear reactors with side MA transmutation, i.e., small MA addends (1-3% of the basic fuel mass) to the reactor core;
- the MA cross sections must be known to at least the same accuracy as in the case of  $^{235}\text{U}$  (0.2-0.3%) and  $^{239}\text{Pu}$  (0.5%) in the design studies of the job-oriented reactors (transmitters), wherein MAs constitute the major portion of fuel (molten-salt reactors, ADS facility blankets).

### 2. Formulation of the problem

The various international scientific meetings and publications reverted repeatedly to expressing a necessity for the integral experiments that would make use of a salt blanket model coupled to an ADS facility. The experiments are expected to permit validation for adequacy of the nuclear constants and of the simulation codes used to calculate them, as well as optimization of the loading and reprocessing performance for the nuclides to be transmuted. Numerous relevant technological matters are also expected to settle.

As of nowadays, however, designing and manufacturing a full-scale salt blanket model are very expensive and can hardly be financed in any foreseeable future.

The optimal alternative, which has been selected in Project 1145, is to carry out the integral experiments with the salt (0.52NaF+0.48ZrF<sub>4</sub>) blanket micromodels (SBM) of different-geometries (a sphere at VNIIEF, Sarov, and a cylinder at ITEP, Moscow). The neutron spectrum variations were simulated by two different methods. At VNIIEF, 2.5% UF<sub>4</sub> (90%  $^{235}\text{U}$  enrichment) was inserted into the spherical model. At ITEP, a fuel channel with the bushing-type fuel elements of 90%  $^{235}\text{U}$  enrichment was inserted in the center of the cylinder-shaped micromodel.

At ITEP, the salt blanket experiments were made using the MAKET zero-power heavy-water reactor. Conforming to the Project 1145 research schedule, the following experiments were planned:

- ◇ determining the space distribution of the fission reaction rates (see Table 1) by  $\gamma$ -spectrometry;
- ◇ determining the space distribution of the radiative capture reaction rates and the threshold reaction rates by  $\gamma$ -spectrometry for the isotopes of well-known cross sections (see Table 1);

- ◇ determining the fission reaction rates for  $^{237}\text{Np}$ ,  $^{238}\text{Pu}$ ,  $^{240}\text{Pu}$ ,  $^{241}\text{Pu}$ ,  $^{242\text{m}}\text{Am}$ ,  $^{243}\text{Cm}$ , and  $^{245}\text{Cm}$  at different points of the SBM (see Table 1) by the SSNTD method;
- ◇ determining the power of the MAKET critical facility;
- ◇ studying the reactivity effects in the SBM.

The experimental (MAKET-measured) reaction rates (see Table 1) were simulated by the ML45, NJOY-94(99), and MCNP-4B codes using the ENDF/B-VI (rev.7) and JENDL3.2 libraries.

The following preparatory steps preceded the experiments:

- ◇ the SBM has been designed;
- ◇ the SBM was manufactured at the Chepets Mechanical Plant (Glazov);
- ◇ ~70 kg of the  $0.52\text{NaF}+0.48\text{ZrF}_4$  salt was built up;
- ◇ the SBM volumes were filled with the salt;
- ◇ the fuel channel, whereon the SBM is fixed, was mounted inside the MAKET facility tank;
- ◇ different fuel lattices were formed around the SBM.

Table 1. The nuclear reactions to be measured with the MAKET facility.

Reactions	FKBN-2M		MAKET						
	Micromodel								
	Salt*	Salt+U**	Salt*				Salt**+fuel channel		
	Experimental sample position (mm)								
	Ball center	Ball center	0	46.5	72	96.5	46.5	72	96.5
<sup>235</sup> U(n,f) (репер)	x	x	x +	x +	x +	x +	x +	x +	x +
<sup>237</sup> Np(n,f)	x	x	X	-	-	-	x	-	-
<sup>238</sup> Pu(n,f)	x	x	X	-	-	-	x	-	-
<sup>239</sup> Pu(n,f)	x	x	X	x	x	x	x		x
<sup>240</sup> Pu(n,f)	x	x	X	-	-	-	x	-	-
<sup>241</sup> Pu(n,f)	x	x	X	-	-	-	x	-	-
<sup>242</sup> Pu(n,f)	x	x	-	-	-	-	-	-	-
<sup>244</sup> Pu(n,f)	x	x	-	-	-	-	-	-	-
<sup>241</sup> Am(n,f)	x	x	-	-	-	-	-	-	-
<sup>242m</sup> Am(n,f)	x	x	X	-	-	-	x	-	-
<sup>243</sup> Am(n,f)	x	x	-	-	-	-	-	-	-
<sup>243</sup> Cm(n,f)	x	x	X	-	-	-	x	-	-
<sup>244</sup> Cm(n,f)	x	x	-	-	-	-	-	-	-
<sup>245</sup> Cm(n,f)	x	x	X	-	-	-	x	-	-
<sup>246</sup> Cm(n,f)	x	x	-	-	-	-	-	-	-
<sup>247</sup> Cm(n,f)	x	x	x****	-	-	-	x****	-	-
<sup>248</sup> Cm(n,f)	x	x	-	-	-	-	-	-	-
<sup>238</sup> U(n,f)	-	-	+****	+****	+****	+****	+****	+****	+****
<sup>238</sup> U(n,γ)	-	-	+	+	+	+	+	+	+
<sup>55</sup> Mn(n,γ)	+	+	+	+	+	+	+	+	+
<sup>63</sup> Cu(n,γ)	+	+	+	+	+	+	+	+	+
<sup>197</sup> Au(n,γ)	+	+	+	+	+	+	+	+	+
<sup>176</sup> Lu(n,γ)	+	+	+	+	+	+	+	+	+
<sup>115</sup> In(n,n')	+	+	+	+	+	+	+	+	+
<sup>32</sup> S(n,p)	+	+	-	-	-	-	-	-	-
<sup>58</sup> Ni(n,p)	+	+	-	-	-	-	-	-	-
<sup>27</sup> Al(n,a)	+	+	+	+	+	+	+	+	+
<sup>19</sup> F(n,2n)	+	+	-	-	-	-	-	-	-
<sup>64</sup> Zn(n,p)	-	-	+	+	+	+	+	+	+
<sup>64</sup> Zn(n,2n)	-	-	+****	+****	+****	+****	+****	+****	+****

x –SSNTD measurements,

+ - γ-spectrometry,

\* - 0.52NaF+0.48ZrF<sub>4</sub>,

\*\* - 0.505NaF+0.47ZrF<sub>4</sub>+0.025UF<sub>4</sub> (90%- <sup>235</sup>U),

\*\*\* -not warranted because of the restricted MAKET facility power.

### 3. Experimental facility

Fig. 1 shows the MAKET critical heavy-water facility used in the experiments [1, 2].

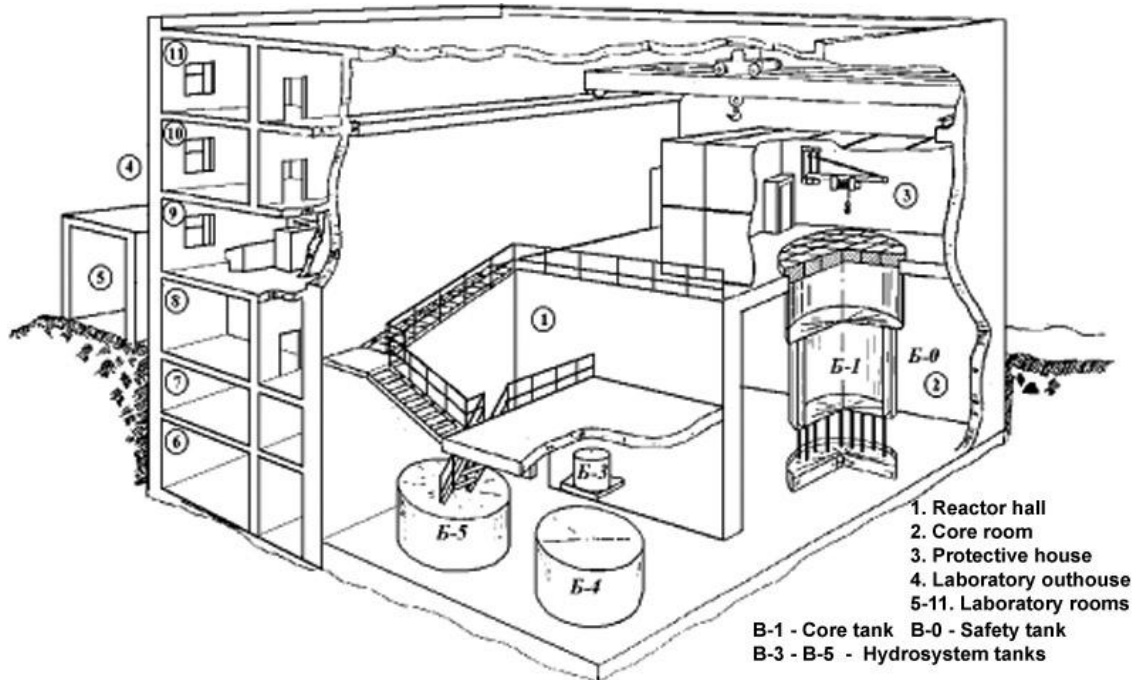


Fig. 1. The MAKET facility.

A separate building of the ITEP premises houses the MAKET facility. As seen from Fig. 1, the biological shielding parts the MAKET building into the outfit (rooms 1-3) and laboratory (rooms 4-10) sectors. The given housing of the laboratories and equipment prevents the personnel and the environment from being exposed to radiation during preparatory works and when experimenting.

The outfit sector houses the critical facility and its support systems. The critical facility is assembled in the core tank placed in a box and is shielded atop by the protective house, which is a “conditionally air-tight” premise separated from the rest rooms of the building. The access to the protective house is only possible via an airlock.

The MAKET hydraulic system is located in the MAKET reactor hall and in the reactor core room. The hydraulic system consists essentially of heavy water tanks, namely,

- ◇ the main tank (B-1) of the core, wherein the critical facility and experimental lattices are placed;
- ◇ the protective tank (B-0) to collect heavy water in case B-1 gets decompressed;
- ◇ the metering tank (B-3) to pump the strictly metered heavy water batches to B-1;
- ◇ the collection tanks (B-4 and B-5) to store all heavy water.

Tank B-1 is placed on the bottom of tank B-0, which is at least 2 m distant from the box walls and floor and is supported by tubular jacks. This arrangement minimizes the impact of the leak neutron backscatter. Table 2 presents the B-0 and B-1 technical data.



Table 2. The B-0 and B-1 technical data.

Tank	External diameter, mm	Wall thickness, mm	Height, mm	Bottom thickness, mm	Volume, m <sup>3</sup>	Material, weight %
B-1	2600	10	3650	16	19	Al-98.3 Mg-0.7, Si - 1.0
B-0	3400	10	3700	16	33	

Two supporting lattices are placed inside tank B-1. The 25-mm thick lower lattice lies right on the tank bottom. The 50-mm thick upper lattice is supported by the B-1 shell and is rigorously fixed by the B-0 inside diameter. The lattice material can be found in Table 2. Tank B-0 is closed atop by the additional biological shield, which is a cell-structured lattice welded of massive duralumin beams filled with borated paraffin. The cells are of 600×400 mm dimensions and are covered with thin-wall duralumin cavity blocks filled with borated paraffin. The safety rod drives are fastened to the lattice points.

The upper supporting lattice has an “insert” with a 259-mm diameter orifice at its center to provide for mounting the central zirconium channel, which carries the experimental SBM. The centers of B-1 (cell 34-20) and of the insert (cell 34-18) are shifted by two cells with respect to one another, i.e., the shift equals  $100 \cdot \sqrt{3} \cong 173$  mm (see Figs. 4, 5, and 25). The actual “channel-SBM” design has made it possible to firmly fix the SBM in the fuel lattice. Fig. 2 is the drawing of the SBM assembly.

The fuel channels are placed around the SBM to form a 100-mm step hexagonal lattice. The channels are tubes of 60×57.6 mm outside and inside diameters, respectively, filled with the bushing-type fuel elements. When in a tube, the fuel elements are supported with the channel bottom (see Fig. 24). The total length of the fuel elements in a channel is 1268 mm. In simulations, a fuel element is conveniently divided into eight zones, whose composition and dimensions are presented in Table 30. The tube material is indicated in Table 2. Each of the fuel elements contained high-enriched uranium.

Either an additional salt insert or the above-mentioned fuel elements can be placed inside the central channel. The central model and the SBM have been made of E125 and E110 zirconium alloys, respectively. Tables 3 and 4 show the chemical compositions of the alloys and the impurity amounts therein.

As seen from Fig. 2, the central channel and the SBM have been designed to include the salt tank and the knockdown fuel channel that consists of its upper, central, and lower parts. The salt tank is placed in the central part. The operations of preparing the 0.52NaF+0.48ZrF<sub>4</sub> molten fluoride mixture and filling the salt tank with the mixture are described in the ARRICT Technical Report.

Table 3. Elemental composition of the zirconium alloys.

E-125		E-110	
Element	Content, %	Element	Content, %
Nb	2.6	Nb	1
Zr	97.24	Zr	98.87

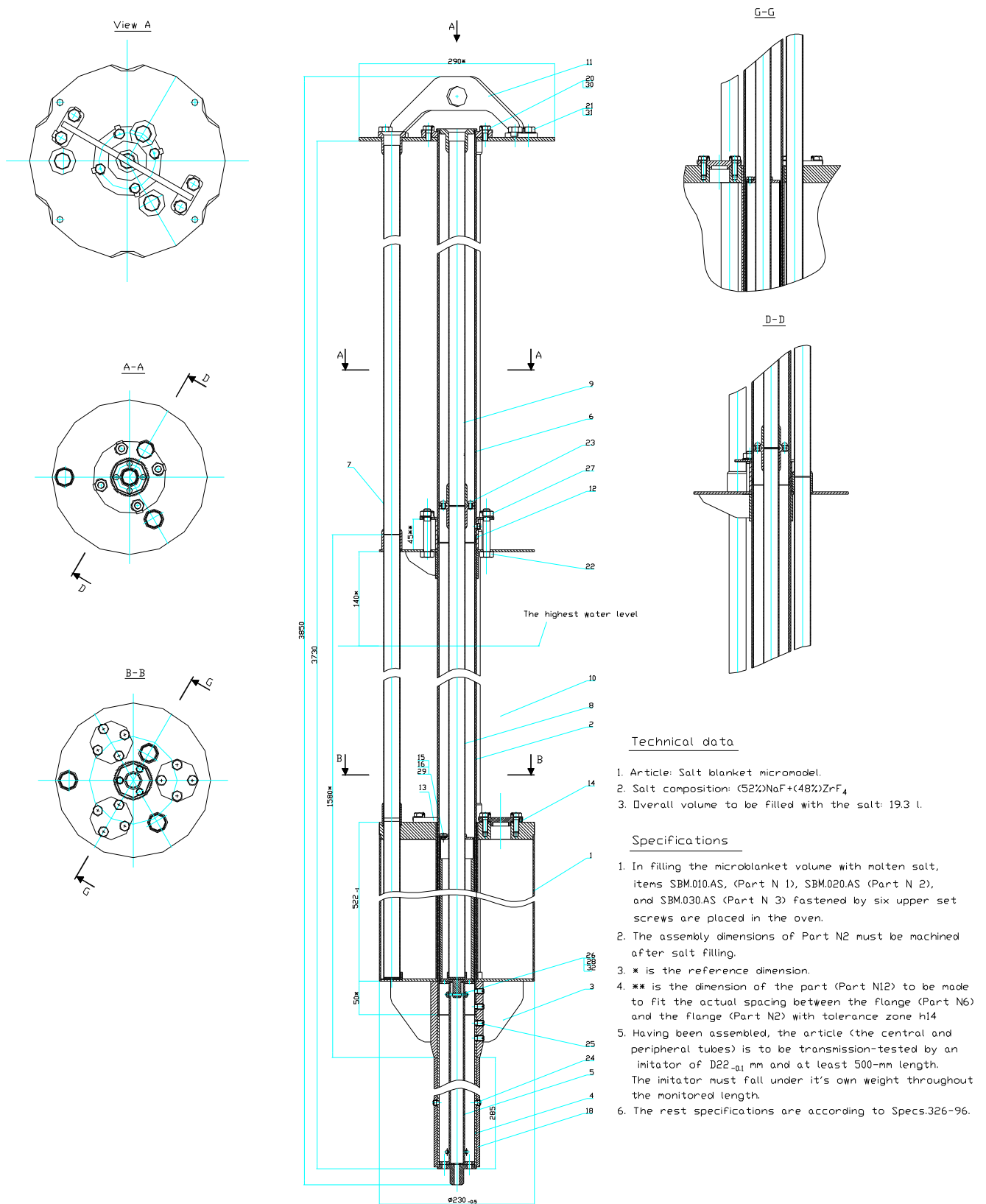


Fig. 2. The SBM.

Table 4. Chemical impurity content of the zirconium alloys.

E-125		E-110	
Element	Content, ppm	Element	Content, ppm
Fe	Fe	Fe	0.0064
Cu	<0.001	Cu	<0.001
Ni	0.0036	Ni	<0.003
Mn	<0.0003	Mn	<0.0003
N	0.00305	N	<0.002
B	<0.00004	B	<0.00004
C	0.0045	C	0.00505
Si	0.0457	Si	0.00565
Sn	<0.01	Sn	<0.01
Cd	<0.00003	Cd	<0.00003
Pb	<0.003	Pb	<0.003
Li	<0.0007	Li	0.00015
Hf	0.0285	Hf	0.0345
Ti	<0.003	Ti	<0.003
O	0.0555	O	<0.03
Al	<0.003	Al	<0.003
Cr	<0.003	Cr	<0.003
Be	<0.0003	Be	<0.0003
K	<0.003	K	<0.003
Ca	<0.01	Ca	<0.01
Mo	<0.003	Mo	<0.003
Cl	<0.0007	Cl	<0.0007
F	<0.003	F	<0.003

First, the ready components (powders of sodium and zirconium fluorides) were mixed thoroughly to maintain the desired mix proportion. After that, the mixture was melt at 640°C and held at that temperature for 30 min in the argon-filled graphite crucibles. A few 0.52 NaF+0.48 ZrF<sub>4</sub> ingots were prepared. Having been cooled, the ingot surfaces were cleaned mechanically to remove any graphite trace. After that, the ingots were crushed into ≤0.6-mm grains. The resultant powder was stirred thoroughly to fill the entire volume of the salt tank with the mixture. The salt tank, together with the fuel channel central part (which was used also as a support when transporting and mounting the facility), was placed in an airtight stainless steel retort. Having been trice “washed” with argon (vacuumed to 0.1 mm Hg and argon-filled to 1.1 abs. bars), the retort was placed into a shaft kiln with a Ni-Cr heater.

Table 5. The characteristics of the melt in the salt tank, the central insert, and the containers.

	Mass, g	Volume, ml	Density, g/cm <sup>3</sup>	Content of elements, mass%			
				Zr	F	Na	
Salt tank	63650 ± 100	17296 ± 5	3.68	42.67	44.71	11.99	0.522NaF+ 0.478ZrF <sub>4</sub>
Central insert	1680 ± 5	493 ± 5	3.41	42.51	44.52	11.46	0.517NaF+ 0.478ZrF <sub>4</sub>
Single-segment containers							
Container (0)	483 ± 1	141.9 ± 0.5	3.45	42.51	44.52	11.46	--''--
Container (46.5)	475 ± 1	142.4 ± 0.5	3.45	42.51	44.52	11.46	--''--
Container (72.0)	479 ± 1	141.3 ± 0.5	3.45	42.51	44.52	11.46	--''--
Container (96.5)	475 ± 1	140.7 ± 0.5	3.45	42.51	44.52	11.46	--''--
Three-segment containers							
Container (0)	375 ± 1	104.3 ± 0.5	3.45	42.51	44.52	11.46	--''--
Container (46.5)	371 ± 1	103.8 ± 0.5	3.45	42.51	44.52	11.46	--''--
Container (72.0)	381 ± 1	104.9 ± 0.5	3.45	42.51	44.52	11.46	--''--
Container (96.5)	376 ± 1	104.6 ± 0.5	3.45	42.51	44.52	11.46	--''--

After being heated to 640–650°C and held at that temperature for 30 min, the retort was taken from the kiln and then cooled. The salt tank having been cooled, the melt level therein lowered. After that, another grained melt portion was added to fill up the tank (the input grained melt density was 2.6 g/cm<sup>3</sup>), whereupon the melting process was repeated.

A significant increase of the melt volume during the melting process ( $\Delta V = 6-8\%$ ) and the equal decrease during the cooling afterwards gave rise to some troubles when filling the upper part of the salt tank. Therefore, the final operation was to add the hot (640-650°C) NaF+ZrF<sub>4</sub> melt to the cooled salt tank, so as the voids in the vat upper part would be packed. Table 5 presents the characteristics of the melt that fills the SBM.

The impurity content of the melt was determined by the atom-emission spectroscopy with induction-bound plasma using the Baird Co. (USA)-made Plasma Spektromet spectrometer. Table 6 presents the analysis results.

The SBM and central channel can be described briefly as follows.

The fuel channel upper part (SBM.060.AS), together with the clamp (SBM.000.11), consists of the lower flange (SBM.060.001), the tube (SBM.060.002), the plate (SBM.060.003), and the upper flange (SBM.060.004). The upper flange (SBM.060.004), together with the plate (SBM.060.003) and the lower flange (SBM.060.001), are welded to the load-bearing tube (SBM.060.002). The clamp is fastened to the plate with bolts M10-7gx20 (Ref. No. 21; 4 pieces) and washers 10.E110 (Ref. No. 31). The plate is fastened to the MAKET critical facility lattice with bolts M10-7gx20 (Ref. No. 21; 4 pieces) and washers 10.E110 (Ref. No. 31). The plate (SBM.060.003) is fastened to the flange (SBM.060.004) with bolts M10-7gx20 (Ref. No. 20; 4 pieces) and washers 8.E110 (Ref. No. 30). Three experimental channels (SBM.070.AS) of 1878-mm length each are inserted into the upper flange (SBM.060.004).

Table 6. Impurity content of the 0.52NaF+0.4ZrF<sub>4</sub> melt.

Element	Content, mass%	Element	Content, mass%	Element	Content, mass%
K	$\leq 5 \cdot 10^{-3}$	Al	$8 \cdot 10^{-2}$	Ni	$1 \cdot 10^{-3}$
Ba	$2.8 \cdot 10^{-2}$	Fe	$5 \cdot 10^{-3}$	Cu	$8 \cdot 10^{-4}$
Mg	$4 \cdot 10^{-3}$	Zn	$2 \cdot 10^{-3}$	V	$< 1 \cdot 10^{-3}$
Ca	$3 \cdot 10^{-2}$	Cr	$7 \cdot 10^{-3}$	Cd	$1 \cdot 10^{-3}$
Sr	$2.5 \cdot 10^{-3}$	Mn	$1.5 \cdot 10^{-4}$	Ti	$2.4 \cdot 10^{-3}$

The oxygen content in the melt is  $10^{-3}$  before melting and  $4 \cdot 10^{-2}$  after melting and filling.

The fuel channel central part (SBM.020.AS) consists of the tube (SBM.020.001), the flange (SBM.020.002), three bushings (SBM.020.003), the bushing (SBM.020.004), and three ribs (SBM.020.005). In its lower part, the tube (SBM.020.001) has a 0.5-mm deep, 574-mm long groove to fix the position of the salt tank (SBM.010.AS). The flange (SBM.020.002) is welded to three ribs (SBM.020.005), which are welded to the bushing (SBM.020.004), which is welded to the fuel channel upper part. Three bushings (SBM.020.003) ensure fastening and alignment of the dry experimental channels (tubes) (SBM.010.001), which are welded to the flange (SBM.020.002).

The fuel channel central part (SBM.020.AS) is connected to the fuel channel upper part SBM.060.AS through the fixer bushing (SBM.000.012) with four bolts M10-7gx65 and washers 10.E110 (Ref. No. 31). The bushing is fastened to the fuel channel upper part with the setscrews M8-7gx14 (3 pieces).

The salt tank (SBM.010.AS) consists of six tubes (SBM.010.001, 3 pieces, and SBM.010.009, 3 pieces), the lid (SBM.010.002), the shell (SBM.010.003), the bottom (SBM.010.004), then inner wall (SBM.010.005), two cut rings (SBM.010.006), three stoppers (SBM.010.007), the ring (SBM.010.008), three bushings (SBM.010.010), and three lids (SBM.010.013). The salt tank is shaped of two coaxial cylinders. The external cylinder (the shell, SBM.010.003) is of 229×224-mm diameter and 506-mm length and the internal cylinder (the inner wall, SBM.010.005) is of 62×58-mm diameter and 522-mm length. The bottom (SBM.010.004) and the lid (SBM.010.002) are welded to the shell (SBM.010.003) and to the inner wall (SBM.010.005). Two cut rings (SBM.010.006) and the ring (SBM.010.008) are welded to the bottom (SBM.010.004), thereby securing the geometric position of the dry experimental channels (tubes, SBM.010.009). The lid (SBM.010.002) has three orifices to fill the tank with the melt of fluorides (0.52NaF+0.8ZrF<sub>4</sub>). The orifices are covered with the small lids (SBM.000.013) to pressurize the salt tank with twelve bolts M8-7gx20 (Ref. No. 20, 12 pieces) with the washers 8.E110 (Ref. No. 30) and the airtight scrubber fillers (SBM.000.014). Each of three salt tank channels consists of two 25×23-mm diameter tubes (SBM.010.001 and SBM.010.009) joined together with the bushing (SBM.010.001) welded to the salt tank lid. When assembling the salt tank, three tubes (SBM.010.009) with the welded bottom stoppers (SBM.010.007) are fixed in the rings (SBM.010.006, 2 pieces, and SBM.010.008, 1 piece), with a 105-mm gap secured between the tank bottom and the channel bottom to permit a thermal extension of the channels when heated in the oven up to 600°C.

In assembling the SBM, the bottom sector of the fuel channel central part (SBM.020.AS) is free to enter the inner wall of the salt tank (SBM.010.AS). The fuel channel lower part (SBM.040.AS) consists of the tube (SBM.040.001) and the bottom (SBM.040.002). The support (SBM.030.AS) is mounted on the upper part of the tube (SBM.040.001) to secure fastening

between the fuel channel central (SBM.020.AS) and lower (SBM.040.AS) parts with twelve setscrews B.M8-7gx14 (Ref. No. 25, 12 pieces). The supporting tube (SBM.000.018) is mounted on the tube lower part (SBM.040.001) and is fastened with stud screws B.M8-7gx10 (Ref. No. 24, 2 pieces). The salt insert (SBM.080.AS) is placed in the fuel channel (SBM.060.002, SBM.020.001, SBM.040.001) together with the dry experimental channel to increase the salt volume.

The salt insert (SBM.080.AS) consists of the bushing (SBM.080.001), the tube (SBM.080.002, the 4<sup>th</sup> 1504-mm long experimental channel), the lid (SBM.080.003), the tube (SBM.080.004), and the bottom (SBM.080.005). The 50×43-mm diameter, 497-mm long tube (SBM.080.004) has a 30-mm long internal groove to reach a 48-mm diameter for securing free filling of the tube with the salt. The lid (SBM.080.003) is welded from above, and the bottom (SBM.080.005) from below, to the tube (SBM.080.004).

The bottom has a settling ring to preserve the geometry of the dry experimental channel (the tube SBM.080.02). The tube (SBM.080.02) has the bottom stopper (SBM.010.07) welded thereto. When assembling the salt insert, the channel descended through the upper orifice down to the bottom, its resultant position in the ring was fixed, and then it was lifted by 1.5 m and welded to the upper lid (SBM.080.03).

A 1.5-mm gap is secured between the tank bottom and the channel bottom to permit thermal extension of the channels when heated up to 6000°C in the oven. The lid (SBM.080.03) has three orifices to receive screws M6 for filling the insert with the 0.52NaF+0.48ZrF<sub>4</sub> salt. The orifices are covered up with the stoppers (SBM.000.015; Ref. No. 15, 3 pieces) and gaskets (SBM.000.016; Ref. No. 16, 3 pieces).

Before placing the salt insert (SBM.080.AS) into the fuel channel (SBM.060.002, SBM.020.001, SBM.040.001), it is connected to the spacer (SBM.050.AS) to be fixed in the central channel. The spacer is connected to the salt insert with the stud M4-7gx35 (Ref. No. 32), two nuts M4-7H (Ref. No. 26), and washers 4 (Ref. No. 28).

The spacer (SBM.050.AS) consists of the support tube (SBM.050.001), to which two flanges (SBM.050.002) are welded.

The containers with the samples therein are moved to the dry experimental channels through four experimental channels (SBM.070.AS, 3 pieces, and SBM.090.AS). The external channels (SBM.070.AS) are connected to the salt tank channels (SBM.010.001; 3 pieces) through bushings. The central channel (SBM.090.AS) is connected to the salt insert tube (SBM.080.002) by screws B.M5-7gx10 (Ref. No. 23, 4 pieces).

The 25×23-mm diameter, 3200-mm long experimental channels are placed between the upper layer of biological shielding and the plate (SBM.060.003).

The SBM having been filled with the 0.52NaF+0.48ZrF<sub>4</sub> melt, it was subjected again to a leakage test. The He-based leak finder indicated that the channel located on the 72-cm radius had lost its tightness inside the SBM. This property of the given channel was used, therefore, to provide for additional monitoring of the SBM tightness. With that purpose, 1.3 abs. bars compressed helium was fed from the gas supply unit to the channel throughout the measurement period.

A minor variation of the He pressure in the system made sure that the SBM did not lose its tightness. To secure the tightness, the Zr tube emerging from the salt tank at the 72-mm radius (SBM.010.001 of 935 mm length) was welded to the tube passing through the upper flange (SBM.070.AS of 1878 mm length). Helium was prevented from being supplied to the SBM in the only case of simultaneous irradiation of four single-segment (three-segment) containers at radii of 0 mm, 46.5 mm, 72 mm, and 96.5 mm, or three single-segment (three-segment) containers at radii of 46.5 mm, 72 mm, and 96.5 mm.

#### 4. Description of the containers used to irradiate the experimental samples

Two types of containers have been designed for irradiating the experimental samples listed in Table 1. The single-segment containers are used to irradiate the integral chambers (the  $^{235}\text{U}$ ,  $^{240}\text{Pu}$ , and  $^{237}\text{Np}$  layers) and the metallic foil samples (the  $^{235}\text{U}$  and  $^{\text{depl.}}\text{U}$  foils and the many-component  $^{27}\text{Al}+^{55}\text{Mn}+^{\text{nat.}}\text{Cu}+^{197}\text{Au}+^{\text{nat.}}\text{Lu}$ ,  $^{115}\text{In}$ ,  $^{27}\text{Al}$ ,  $^{64}\text{Zn}$  alloy foil). The three-segment containers are used to irradiate the shutter chambers (the  $^{238}\text{Pu}$ ,  $^{240}\text{Pu}$ ,  $^{241}\text{Pu}$ ,  $^{242\text{m}}\text{Am}$ ,  $^{243}\text{Cm}$ ,  $^{245}\text{Cm}$ , and  $^{247}\text{Cm}$  layers; the  $^{235}\text{U}$  and  $^{239}\text{Pu}$  benchmarks).

The single-segment container is a 20×22-mm diameter, 500-mm long Zr tube with top and bottom screw caps. The tube is filled with ten small rods of 19.75-mm diameter, ~50-mm depth each made of the alloy, whose characteristics are indicated in Table 5.

The elongate top cap has a hole to fasten a synthetic cord used to load the container to the SBM experimental channel. In total, four single-segment containers have been manufactured for simultaneous irradiating the experimental samples in four SBM channels (0 mm, 46.5 mm, 72.0 mm, and 96.5 mm), in the fuel lattice with the additional salt insert, or in three SBM channels (46.5 mm, 72.0 mm, and 96.5 mm) in the fuel lattice with the uranium fuel elements placed instead of the salt insert in the central channel.

The integral chamber consists of a 19.75-mm diameter, 8.0 mm height casing, a collimator, a nut, and an experimental isotope layer. The detector and the experimental “layer” are strictly placed coaxially and in parallel to one another and are spaced strictly 6 mm apart. The collimator formed a 6-mm diameter detection ring on the detector surface. All the dimensions in the chambers were monitored to be exact using a microscope. A separate integral chamber was used for each of the experimental isotopes. The chambers were always loaded:

- ◇ between the fourth and fifth small multi-salt rods,  $^{240}\text{Pu}$  (a 596-mm vertical distance from the upper surface of the lower supporting lattice to the top butt of the fourth rod);
- ◇ between the fifth and sixth small multi-salt rods,  $^{235}\text{U}$  (a 654-mm vertical distance);
- ◇ between the sixth and seventh multi-salt rods,  $^{237}\text{Np}$  (a 711-mm vertical distance).

The bottom screw cap having been unscrewed, with the appropriate tilt of the channel, the multi-salt rods gravitated downwards and left the zirconium tube. After emerging from the tube, a small multi-salt rod was taken out and, then, sent to the glove box for being temporary stored there. In such a way, five multi-salt rods are extracted. The integral chambers were extracted after the fourth, fifth, and sixth rods. The integral chambers and the multi-salt rods were loaded retrogradely, in reverse order.

Having been extracted, each chamber was disassembled as follows. The container with an experimental layer was taken from the safe. The container surface was checked for  $\alpha$ -activity. The lid was screwed from the container and was placed nearby with its inner surface up. Forceps was used to take away the container stop ring and put it down onto the lid. Again with forceps, the experimental layer was taken from the container via its side slot. In the case of the integral chamber, the “layer” was downed to the chamber bottom using a thin holder inserted into the fabrication hole of the chamber bottom to avoid any abrupt displacement. After that, the collimator and detector were placed in the chamber, whereupon the nut was screwed on. Radiation contamination was monitored in each of the operation steps.

The three-segment container consists of three 20×22-mm diameter zirconium tubes of 206-mm (the upper and lower tubes) and 75-mm (the central tube) lengths. The three tubes are connected to each other with screw bushings. The upper and lower tubes have the screw caps

identical to those of the single-segment channel. The upper tube was filled with the  $0.52\text{NaF}+0.48\text{ZrF}_4$  melt through an orifice. The central tube was filled with the  $0.52\text{NaF}+0.48\text{ZrF}_4$  small rods. The shutter chamber was mounted in the central channel. The shutter chamber differs from the integral chamber in that it is doubled to irradiate two layers simultaneously and has a metal plate with an orifice (a shutter) inserted between the detectors and layers. During the irradiations, the shutter moved upwards, permitting the fission fragments to reach the detector. The metal plates were set to motion by an electromagnet remote-controlled from the MAKET facility control board. The control permitted independent switching of the shutters in each of the containers, thus attaining the necessary irradiation time for each pair of layers in the respective container. The control elements and the power were supplied through a  $4\times 2.5$ -mm diameter zirconium tube of 174-mm length.

In total, four three-segment containers were manufactured for being irradiated simultaneously in four experimental channels of the SBM when placed in the lattice with salt insert in the central channel, or in three experimental channels in the lattice with eight fuel elements in the central channel. Simultaneous irradiation in all four (or three) three-segment containers was made only for the  $^{235}\text{U}$  and  $^{239}\text{Pu}$  layers. The rest layers ( $^{237}\text{Np}$ ,  $^{238}\text{Pu}$ ,  $^{240}\text{Pu}$ ,  $^{241}\text{Pu}$ ,  $^{242\text{m}}\text{Am}$ ,  $^{243}\text{Cm}$ ,  $^{245}\text{Cm}$ , and  $^{247}\text{Cm}$ ) were irradiated at radial distance "0" in the lattice with salt insert in the central channel, and "46.5" in the lattice with eight fuel elements in the central channel.

As mentioned above, two layers were simultaneously loaded in the shutter chamber. One of the two (either  $^{235}\text{U}$  or  $^{239}\text{Pu}$ ) was used as benchmark; besides, both layers could be irradiated together. Before loading the layers, the chamber was disassembled into its halves. Either of the halves has an 18-mm diameter, 0.2-mm deep "seat" to place a layer. Having been taken from its container, a layer was fastened in its seat of the shutter chamber, whereupon forceps was used to try out the fastening. The procedure was then repeated with the second layer. After that, the shutter chamber halves were tightened together with screws and the shutters were inserted. The assembled shutter chamber was inserted against the stop in the central segment of a three-segment container. The bottom screw cap was then screwed tight. The layers were placed back-to-back in the chamber. The chamber was ready to operate after the screw caps connect all three segments.

The shutter chamber was loaded into, and taken from the central segment of a three-segment container after unscrewing the lower screw connector of the latter. The chamber emergence rate was adjusted by the angle of the tube tilt with respect to a horizontal surface.

The fission fragments were recorded with SSNTDs, which are  $12\times 12\times 15$ -mm silicate glass (in the integral chamber) and 12-mm diameter, 25- $\mu\text{m}$  thick polycarbonate film of molecular mass 9000 (in the shutter chamber). The SSNTDs are insensitive to  $\alpha$ -,  $\beta$ -, and  $\gamma$ -emissions and, given the appropriate conditions, show 100% efficiency in recording the fragments. To build up the desired statistics, the shutter and integral chambers were unloaded from the three- or single-segment channel after each irradiation run; a detector was taken away and was then replaced with a fresh detector. This operation was repeated five times for each of the layers.

After the full measurement cycle of the shutter or integral chamber, the layers were replaced. The operation began with monitoring the layer "scale-off". In case the  $\alpha$ -count was null on the detector surface, the scale-off was regarded as absent. After that, the fastening screws were unscrewed and a chamber was disassembled. A layer was then lifted from its seat with a small needle and carried to its open container with forceps.



The operation having been complete, the instruments, the tools, the gloves, and the chamber and container surfaces were dosimetered.

### **5. Formation and optimization of the fuel lattice**

The fuel lattices were formed by the criterion of radial and axial (lattice depth) symmetry, which is the basic lattice geometry criterion. Besides, the difference of the true salt and heavy water parameters from the parameters used in the approximate analysis was allowed for.

Radial bisymmetry of the lattices (a  $\frac{1}{2}$  symmetry coefficient) was selected, so that the geometry of the SBM location in the MAKET core tank proves to be correct in terms of description by a mathematical model.

The axial symmetry is much more difficult to attain because the critical heavy water level, which essentially defines the axial symmetry, is determined by the design and composition of the fuel channels with fuel elements, by the heavy water composition, and by the SBM design and composition. As noted above, the parameters were all included in the approximate analysis and design study aimed at designing the SBM whose center would coincide with the core center in height.

Allowance was made for the specificity of the critical experiments, in which the upper and lower end-face heavy water reflectors appear in the axial lattice structure. The design features of the fuel channels have determined a 15-mm height of the lower] end-face reflector. The upper end face reflector was formed as the critical state was reached; the critical level of the lattice determined the height of the upper end face reflector. The axial symmetry of the lattice is secured when the height of the upper end face reflector also approaches 15 mm.

Conforming to the approximate analysis study, the first fuel lattice 21-2 was assembled of 32 standard fuel channels. The critical lattice level was 1700 mm, which determined a 417-mm height of the upper reflector. Fig. 3 presents the lattice cartogram. Further optimization of the lattice was aimed at lowering its critical level. This can most effectively be reached by mounting additional fuel channels. Formation of new lattices has made it possible to obtain some critical compositions, whose cartograms are also shown in Fig. 3. The parameters of all the lattices are summarized in Table 7.

Table 7. Parameters of critical lattices 21-1 and 21-2.

Nos.	Lattice	T(D <sub>2</sub> O), °C	C(D <sub>2</sub> O), %	D <sub>2</sub> O level, cm	K <sub>eff</sub>	Note
1*	21-1	8.5	94.19	1700 ±10	1.00216±0.00051	Without containers, He
2	21-1-1	8.8	94.18	1514 ±2	1.00218±0.00052	Without containers, He
3	21-1-2	8.7	94.18	1448 ±2	1.00204±0.00052	Without containers, He
4	21-1-3	10.7	94.15	1396 ±2	1.00138±0.00052	Without containers, He
5	21-1-4	10.7	94.15	1351 ±2	1.00135±0.00052	Without containers, He
6	21-1-5	10.3	94.15	1358 ±2	1.00037±0.00043	Containers Nos. 1,2,4(1), He
7**	21-1-5(M2)	11.3	94.04	1382.5 ±2		Containers Nos. 1,2,3,4(1)
8	21-1-5(M2)	10.3	93.97	1385.5 ±2		Containers Nos. 1,2,3,4(1)
9	21-1-5(M2)	11.6	93.94	1391.5 ±2		Containers Nos. 1,2,3,4(1)
10	21-1-5(M2)	11.8	93.94	1388 ±2		Containers Nos. 1,2,3,4(1)
11	21-1-5(M2)	11.0	93.93	-		Containers Nos. 1,2,3,4(1)
12	21-1-5(M2)	12.4	93.92	1401 ±3		Containers Nos. 1,2,3,4(3x)
13	21-1-5(M2)	13.0	93.91	1408 ±2		Containers Nos. 1,2,3,4(3x)
14	21-1-5(M2)	12.8	93.90	1382.5 ±2		Containers Nos. (3x),2,3,4(1)
15	21-1-5(M2)	12.4	93.90	1398 ±2		Containers Nos. (3x),2,3(He),4(1)
16	21-1-5(M2)	12.4	93.89	1398 ±2		Containers Nos. (3x),2,3(He),4(1)
17	21-1-5(M2)	12.1	93.89	1398 ±2		Containers Nos. (3x),2,3(He),4(1)
18	21-1-5(M2)	13.1	93.87	1400 ±2		Containers Nos. 1(3x),2,3(He),4(1)
19	21-1-5(M2)	13.0	93.87	-		Containers Nos. 1,2,3(He),4(1)
20	21-1-5(M2)	12.8	93.86	1393 ±2		Containers Nos. 1,2,3(He),4(1)
21**	21-2	12.8	93.83	1307 ± 2	1.00431±0.00015	Containers Nos. 2,3(He),4(1)
22	21-2-1	12.9	93.83	1301 ± 2	1.00243±0.00033	Without containers (He)
23	21-2(M1)	13.7	93.76	1319 ± 2		Containers Nos. 2,3,4(1)
24	21-2	12.9	93.75	1319 ± 2		Containers Nos.2,3,4(3x)
25	21-2	12.4	93.75	1319 ± 2		Containers Nos. 2,3,4(3x)
26	21-2	12.1	93.74	1316 ± 2		Containers Nos. 2(3x),3(He),4(1)
27	21-2	10.9	93.73	1316 ± 2		Containers Nos. 2(3x),3(He),4(1)
28	21-2	11.1	93.72	1317 ± 2		Containers Nos. 2(3x),3(He),4(1)
29	21-2	11.6	93.72	1316 ± 2		Containers Nos. 2(3x),3(He),4(1)

30	21-2	11.6	93.72	1316 ± 2		Containers Nos. 2(3x),3(He),4(1)
31	21-2	11.8	93.69	1317 ± 2		Containers Nos. 2,3,4(1)
32	21-2	11.9	93.69	1317 ± 2		Containers Nos. 2,3,4(1)
33	21-2	11.9	93.68	1317 ± 2		Containers Nos. 2,3,4(1)
34	21-2	11.9	93.67	1320 ± 2		Containers Nos. 2,3,4(1)
35	21-2	12.2	93.65	1318 ± 2		Containers Nos. 2,3,4(1)

\* - The critical state was not reached because of D<sub>2</sub>O<sub>2</sub> deficit. The critical level was determined by extrapolating the dependence 1/N from the D<sub>2</sub>O<sub>2</sub> level.

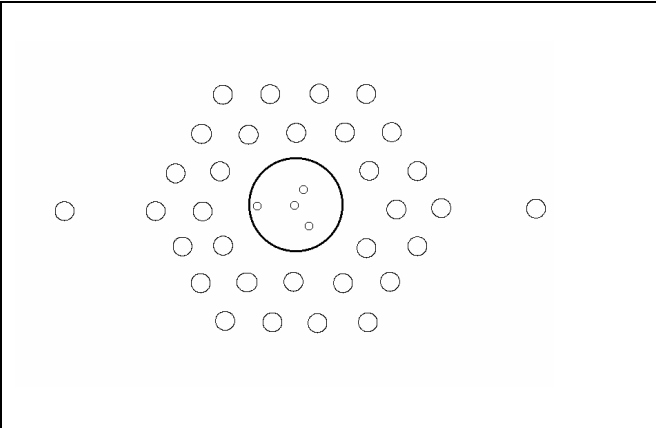
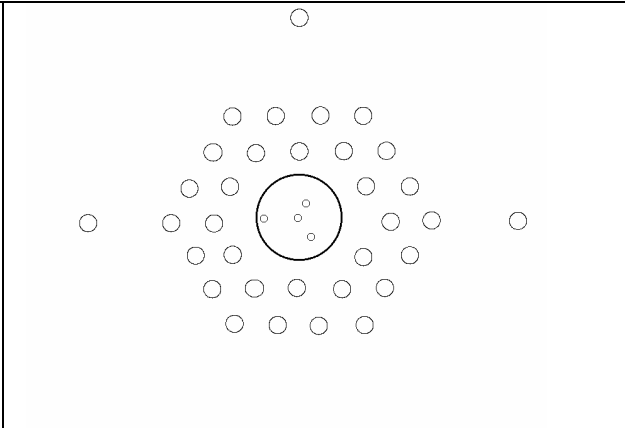
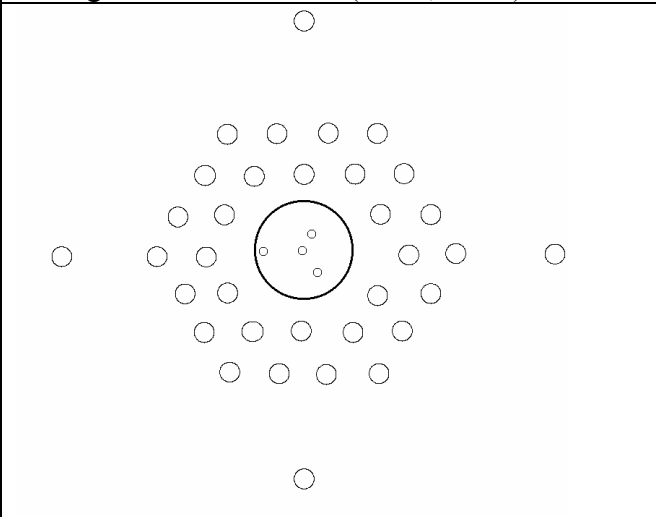
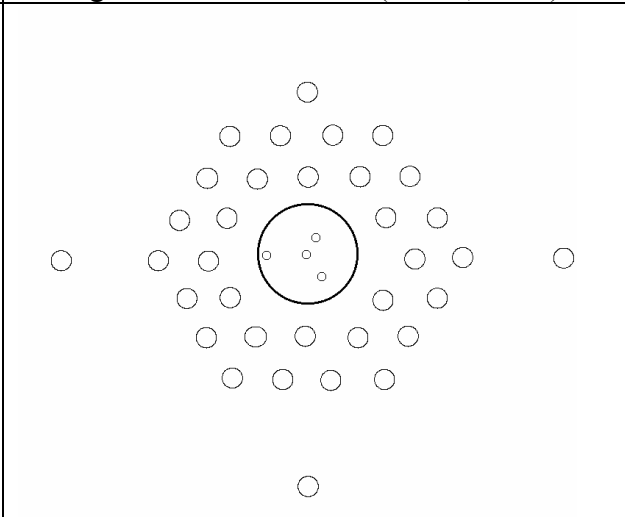
\*\* Base lattice.

Notation in brackets:

(1) Single-segment container,

(3x) Three-segment container,

(He) A 1.3 abs. bars He surplus pressure in SBM.

	
Cartogram of lattice 21-1 (32FC, SBM)	Cartogram of lattice 21-1-1 (33 FC, SBM)
	
Cartogram of lattice 21-1-2 (34 FC, SBM)	Cartogram of lattice 21-1-3 (34 FC, SBM)

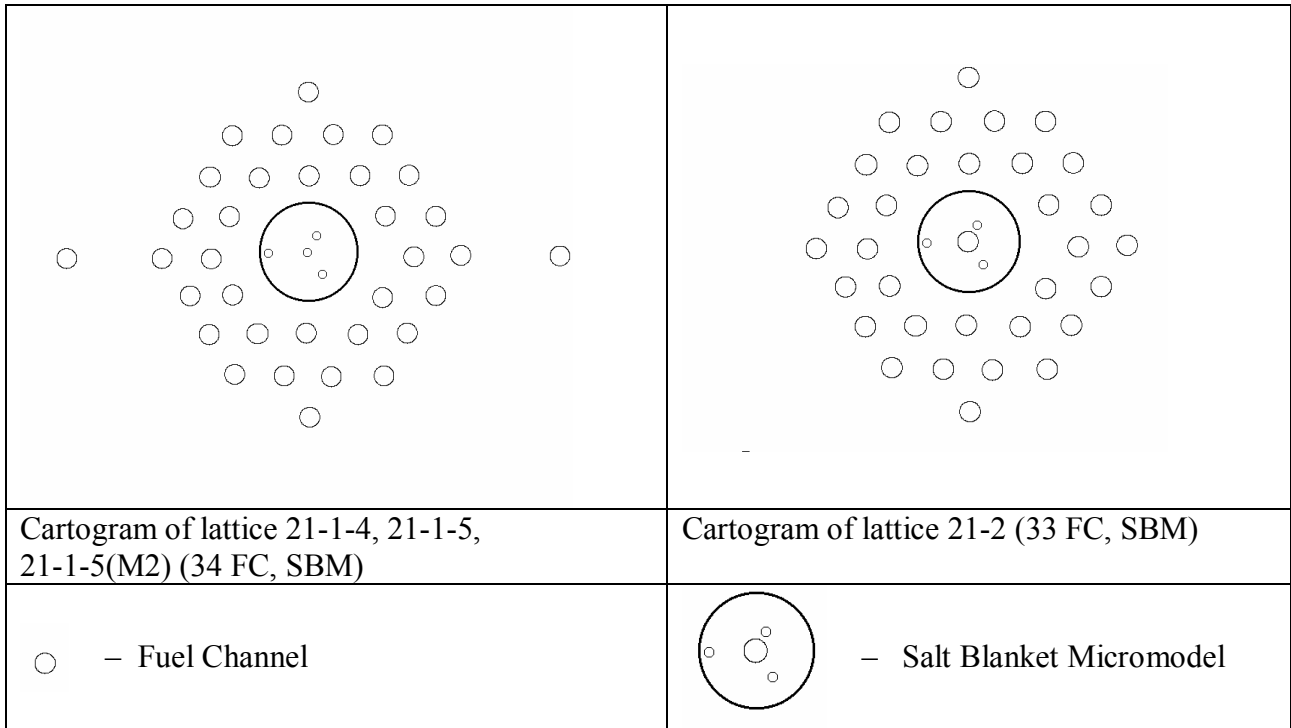


Fig. 3. Modification of lattices 21-1 and 21-2.

As seen from Table 7, the optimization of the fuel lattices has led to the formation of lattice 21-1-5(M2) with radial bisymmetry  $\frac{1}{2}$  and a 1382.5-mm critical level, thus securing a 99.5-mm height of the upper reflector. Further optimization of the lattice did not prove to be effective because its radial symmetry got distorted.

The final version of the first base fuel lattice 21-1-5(M2) consisted of 34 standard fuel channels and the central Zr-made fuel channel with the SBM and four single-segment containers inserted therein. According to Table 5, the  $0.52\text{NaF}+0.48\text{ZrF}_4$  salt mass in the fuel lattice was 67 242 g. Fig. 4 is a detailed cartogram of the MAKET core with lattice 21-1-5(M2).

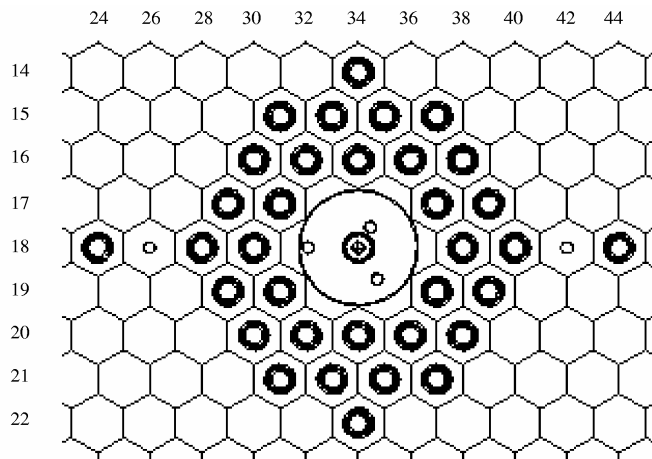


Fig. 4. Cartogram of lattice 21-1-5(M2).

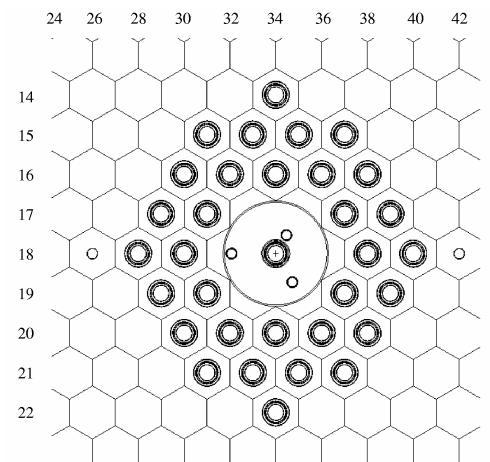


Fig. 5. Cartogram of lattice 21-2.

The second fuel lattice (21-2, see Fig. 3) had to be formed with the view to the second measurement run in the SBM with a changed neutron spectrum, i.e., introduction of fissile materials into the SBM was imitated. With that purpose, the additional salt insert was removed

from the central fuel channel and was replaced by the bushing-type fuel elements of 1268-mm total length. The resultant lattice was optimized by taking fuel channels 24-18 and 44-18 from the MAKET core. In accordance with Table 5, the  $0.52\text{NaF}+0.48\text{ZrF}_4$  salt mass was 65 079 g in the optimized second fuel lattice with the SBM and three single-segment containers. Table 7 presents the parameters of all the lattices. Fig. 5 is a detailed cartogram of the core with lattice 21-2.

The reactivity effects induced by the single- and three-segment containers were estimated using the critical parameters of lattices 21-1-5(M2) and 21-1-4, as well as 21-2 and 21-2-1, together with the experimental dependence  $d\rho/dh$  (the lattice reactivity behaviour as a function of heavy water level of the core tank). The results are presented in Table 8. In view of the significant negative reactivity induced by SBM in lattices 21-1-5(M2) and 21-2 (the  $\Delta K_{\text{eff}}$  values with the SBM taken out were estimated to be  $0.0580\pm 0.0003$  and  $0.0669\pm 0.0004$  in the two lattices, respectively), its value was not determined experimentally by varying the heavy water level of the core tank.

Table 8. Weights of the experimental containers.

Lattice	Number of containers	Container type	Weight, %
21-1-5(M2)	4	Single segment	$0.13\pm 0.05$
	4	Three segments	$0.23\pm 0.09$
21-2	3	Single segment	$0.09\pm 0.04$
	3	Three segments	$0.12\pm 0.06$

## **6. The preparatory steps for the SBM to be mounted in the MAKET core and for heavy water to be chemically purified; monitoring of the heavy water state in the experiments**

The reported researches are featured by denial of a dry channel when placing the SBM in the MAKET core. In return, strict constraints are imposed on the purity requirements of the SBM surface in case the core is devoid of the dry channel intended for being used as an additional protective barrier between heavy water and SBM. The requirements were dictated by the necessity of preserving the desired quality of heavy water in the MAKET facility during the experiments.

In view of the above, the SBM surface was cleaned to remove all possible dirt in a number of additional operations that fall outside the Project 1145 Workplan.

First, the SBM surface was degreased with toluene and, then, washed thoroughly with acetone and distilled water. The SBM surface was checked for cleanness by placing it into a 60-liter polyethylene tank filled with distilled water of conductivity  $\chi = 2.3 \mu\text{S}/\text{cm}$  (at  $24^\circ\text{C}$ ; the same temperature hereafter). The target was immersed in water.

Simultaneously, a 19.75-mm diameter, 50-mm thick  $0.52\text{NaF}+0.48\text{ZrF}_4$  pellet was placed in a glass filled with distilled water of the same conductivity as above. The quality of water was monitored for a few days by measuring the water conductivity. The sampled water was analyzed by a KL-12 conductivity meter, whose measurement accuracy is  $\pm 0.025 \mu\text{S}/\text{cm}$ . The analysis results are displayed in Figs. 6 and 7.

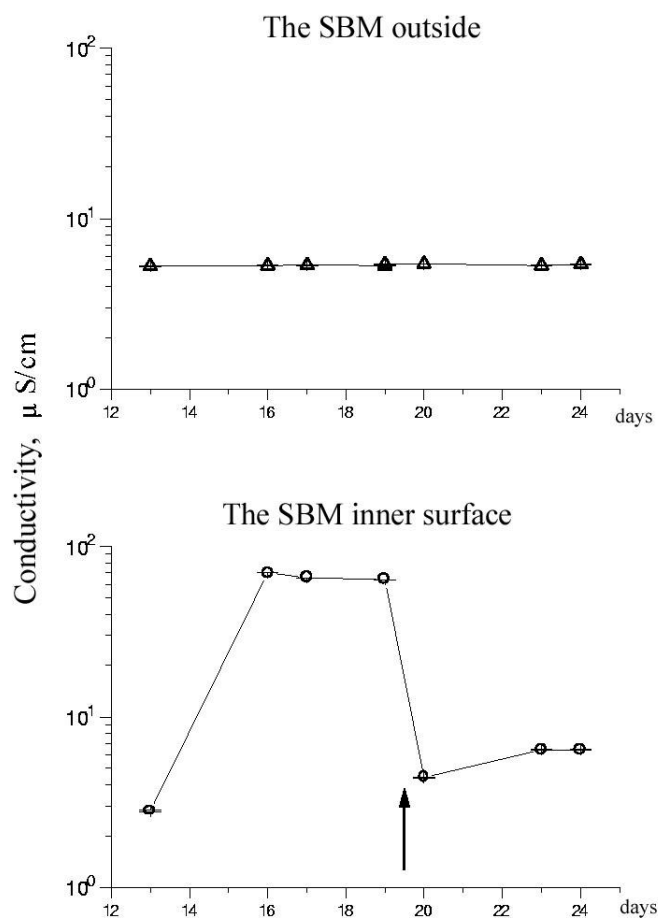


Fig. 6. The estimated dirt on the SBM inside and outside surfaces.

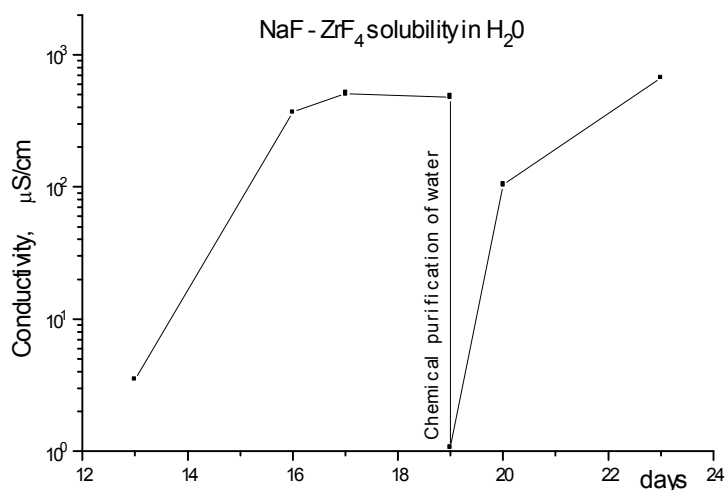


Fig. 7. The estimated feasible pollution of water by the 0.52NaF+0.48ZrF<sub>4</sub> salt.

From Figs. 6 and 7 it follows that the conductivity in the glass and in the polyethylene tank (for the SBM outside surface) increases significantly compared with its initial level. The conductivity in the glass after stirring the solution increased actually by two orders. After that, the increase rate lowered somewhat. In three days, as seen from Fig. 7, the water conductivity in

the glass got stabilized at  $\sim 500 \mu\text{S}/\text{cm}$ . It should be noted right away that water from the glass with the pellet was filtrated through AV-17-8CS and KU-2-8CS ionites taken to be 2:1 by volume. From Fig. 7 it is seen that the above procedure has actually purified water to reach  $\chi = 1.06 \mu\text{S}/\text{cm}$ . When the same  $0.52\text{NaF}+0.48\text{ZrF}_4$  pellet was immersed in the purified water, the quality of the latter got much deteriorated again.

From Fig. 6 it is seen that the conductivity increased also in the tank with the SBM to reach a steady 60-70  $\mu\text{S}/\text{cm}$  level, with the conductivity rise being characteristic of the SBM inner channel only. As to the water sampled from the outside volume, its conductivity was  $\sim 5.3$ – $5.5 \mu\text{S}/\text{cm}$ .

The above results were sheer evidence of dirt on the surface of the SBM inner channel. Most probably, the dirt was the remains of the melt that appeared on the inner surface when the SBM was filled with the  $0.52\text{NaF}+0.48\text{ZrF}_4$  salt. It should be emphasized that Al plates were deliberately immersed into the SBM inner channel water of 60-70  $\mu\text{S}/\text{cm}$  to imitate interaction of the so dirtied surface of the MAKET facility Al tank B-1.

After the plates were taken from water, their surfaces showed white-pale spots of the crumbly Al corrosion products, thus indicating a high corrosive activity of polluted water.

In six days after the experiment start, with the view to a more representative dataset, water was sampled for the purpose of the element-by-element analysis by the atom-emission spectroscopy with induction-bound plasma using the Baird Co. (USA)-made Plasma Spektromet spectrometer. The analysis results are presented in Table 9, where n0 is the distilled water check sample; nI is water from the inner channel of the SBM; nII is water from the outside volume of the tank; nIII is water from glass with pellet (prior to purification by the ionites).

From Table 9 it follows that the sampling shows a marked increase in the Na and Zr concentrations compared with the distilled water check sample, with the resultant concentration values correlating quite properly to the conductivity data. It should be noted also that an increased Si concentration was observed throughout the sampling. The increase is most probably due to the  $\text{F}^-$  ion interactions with the material of the glass used in the sampling for analysis. A good correlation to the conductivity data was observed in that case too.

The data obtained have shown that the SBM is applicable to the MAKET facility experiments if only the SBM surface (inner surface in particular) is additionally cleaned, just what was done during the preparatory work stage. The desired SBM surface cleanness was attained by repeated mechanical cleaning the surface of the SBM inner channel, by degreasing the SBM surface with ethanol, and by washing it with distilled water. This can be seen clearly in Fig. 6.

In line with cleaning the SBM surface, heavy water proper was purified to remove impurities. With that purpose, heavy water was pumped from tank B-4 to tank B-1. The MAKET facility water purification column was filled with the AV-17-8CS and KU-2-8CS ionites taken to be 2:1 by volume. Small portions of the  $\text{H}^+$  and  $\text{OH}^-$  forms of the cation and anion exchangers were mixed. Next, the column was filled with heavy water of a  $\sim 65\%$  deuterium content and was then held as such for  $\sim 2$  days. After that, the column was emptied and was then filled anew with  $\sim 90\%$  and  $\sim 98\%$  deuterium-enriched waters in turn. In such a manner, a 94-95% deuterium concentration was reached, which was close to the initial deuterium content of the tank B-1 water (according to the analysis results as of the column filling day).



Table 9. Impurity content in the H<sub>2</sub>O samples.

Element	Results of analyzing the H <sub>2</sub> O samples, mass %			
	n.0	n.I	n.II	n.III
Fe	$5 \cdot 10^{-8}$	$5 \cdot 10^{-5}$	$2 \cdot 10^{-6}$	$2 \cdot 10^{-4}$
Co	$<5 \cdot 10^{-8}$	$1 \cdot 10^{-6}$	$<5 \cdot 10^{-8}$	$3 \cdot 10^{-6}$
Mn	$<1 \cdot 10^{-8}$	$5 \cdot 10^{-7}$	$4 \cdot 10^{-8}$	$3 \cdot 10^{-6}$
Cr	$<5 \cdot 10^{-8}$	$1.5 \cdot 10^{-6}$	$<5 \cdot 10^{-8}$	$7 \cdot 10^{-5}$
Mg	$4 \cdot 10^{-7}$	$3 \cdot 10^{-6}$	$3 \cdot 10^{-6}$	$1 \cdot 10^{-4}$
Sr	$<3 \cdot 10^{-6}$	$2 \cdot 10^{-7}$	$2 \cdot 10^{-7}$	$2 \cdot 10^{-6}$
Na	$4 \cdot 10^{-6}$	$5 \cdot 10^{-4}$	$2 \cdot 10^{-5}$	$5 \cdot 10^{-3}$
Sn	$<5 \cdot 10^{-7}$	$<5 \cdot 10^{-7}$	$<5 \cdot 10^{-7}$	$3 \cdot 10^{-5}$
Zn	$1 \cdot 10^{-6}$	$1 \cdot 10^{-5}$	$2 \cdot 10^{-5}$	$1 \cdot 10^{-5}$
Au	$<1 \cdot 10^{-8}$	$<1 \cdot 10^{-8}$	$<1 \cdot 10^{-8}$	$<1 \cdot 10^{-8}$
In	$<5 \cdot 10^{-7}$	$<5 \cdot 10^{-7}$	$<5 \cdot 10^{-7}$	$<1 \cdot 10^{-6}$
B	$<1 \cdot 10^{-7}$	$1 \cdot 10^{-7}$	$<1 \cdot 10^{-7}$	$3 \cdot 10^{-6}$
Mo	$<2 \cdot 10^{-7}$	$<2 \cdot 10^{-7}$	$<2 \cdot 10^{-7}$	$<5 \cdot 10^{-7}$
Zr	$<2 \cdot 10^{-8}$	$6 \cdot 10^{-4}$	$1 \cdot 10^{-5}$	$1.5 \cdot 10^{-2}$
Li	$<5 \cdot 10^{-8}$	$<5 \cdot 10^{-8}$	$<5 \cdot 10^{-8}$	$<1 \cdot 10^{-7}$
Ni	$<1 \cdot 10^{-7}$	$2 \cdot 10^{-6}$	$<1 \cdot 10^{-7}$	$2 \cdot 10^{-5}$
V	$<5 \cdot 10^{-8}$	$<5 \cdot 10^{-8}$	$<5 \cdot 10^{-8}$	$1 \cdot 10^{-6}$
Cu	$<5 \cdot 10^{-8}$	$2 \cdot 10^{-6}$	$<5 \cdot 10^{-8}$	$<1 \cdot 10^{-6}$
Ca	$4 \cdot 10^{-6}$	$1 \cdot 10^{-5}$	$1 \cdot 10^{-5}$	$1 \cdot 10^{-4}$
Ba	$4 \cdot 10^{-8}$	$1.5 \cdot 10^{-6}$	$1 \cdot 10^{-6}$	$3 \cdot 10^{-5}$
Al	$2 \cdot 10^{-7}$	$6 \cdot 10^{-5}$	$5 \cdot 10^{-6}$	$1.2 \cdot 10^{-4}$
K	$<2 \cdot 10^{-6}$	$<2 \cdot 10^{-6}$	$<2 \cdot 10^{-6}$	$<5 \cdot 10^{-6}$
Pb	$<5 \cdot 10^{-7}$	$<5 \cdot 10^{-7}$	$<5 \cdot 10^{-7}$	$<1 \cdot 10^{-6}$
Bi	$<2 \cdot 10^{-7}$	$<2 \cdot 10^{-7}$	$<2 \cdot 10^{-7}$	$<1 \cdot 10^{-6}$
Cd	$<2 \cdot 10^{-8}$	$<2 \cdot 10^{-8}$	$<2 \cdot 10^{-8}$	$<1 \cdot 10^{-7}$
Ag	$<1 \cdot 10^{-7}$	$4 \cdot 10^{-6}$	$<1 \cdot 10^{-7}$	$<5 \cdot 10^{-7}$
Ga	$<5 \cdot 10^{-7}$	$<5 \cdot 10^{-7}$	$<5 \cdot 10^{-7}$	$<1 \cdot 10^{-6}$
Sb	$<5 \cdot 10^{-7}$	$<5 \cdot 10^{-7}$	$<5 \cdot 10^{-7}$	$<1 \cdot 10^{-6}$
Ti	$<2 \cdot 10^{-8}$	$8 \cdot 10^{-8}$	$2 \cdot 10^{-8}$	$1 \cdot 10^{-6}$
Be	$<1 \cdot 10^{-8}$	$<1 \cdot 10^{-8}$	$<1 \cdot 10^{-8}$	$<1 \cdot 10^{-8}$
Si	$<5 \cdot 10^{-7}$	$4 \cdot 10^{-4}$	$5 \cdot 10^{-5}$	$7 \cdot 10^{-3}$
Cl	$<5 \cdot 10^{-5}$	$<5 \cdot 10^{-5}$	$<5 \cdot 10^{-5}$	$5 \cdot 10^{-5}$

The water purification techniques included the water passage through the ionite-filled column at the rate determined experimentally by testing the water sample for conductivity and for pH. Water was sampled in the beginning of the purification cycle after each interval of 1-1.5 hours and, then, after some longer intervals. Use was made of a KL-2 conduction meter and a pH-673M pH meter, whose abs. metering accuracy is 0.05. Figs. 8 and 9 show the measurement results.

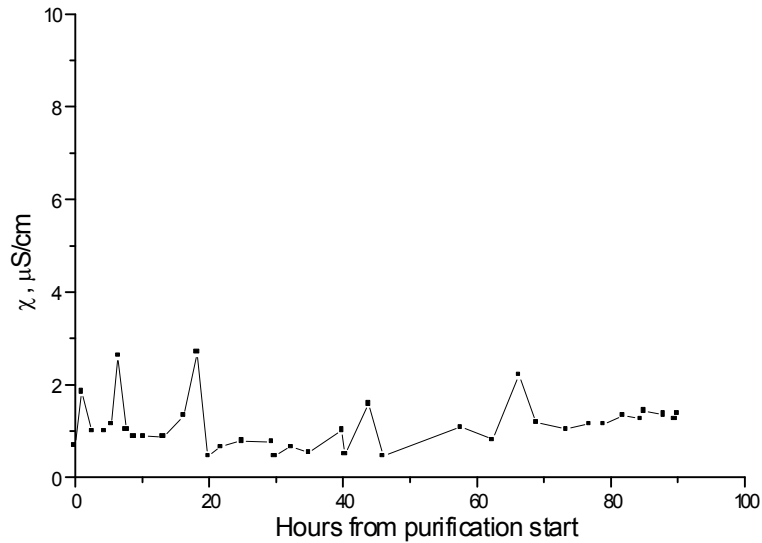


Fig. 8. Heavy water conductivity variations throughout purification cycle.

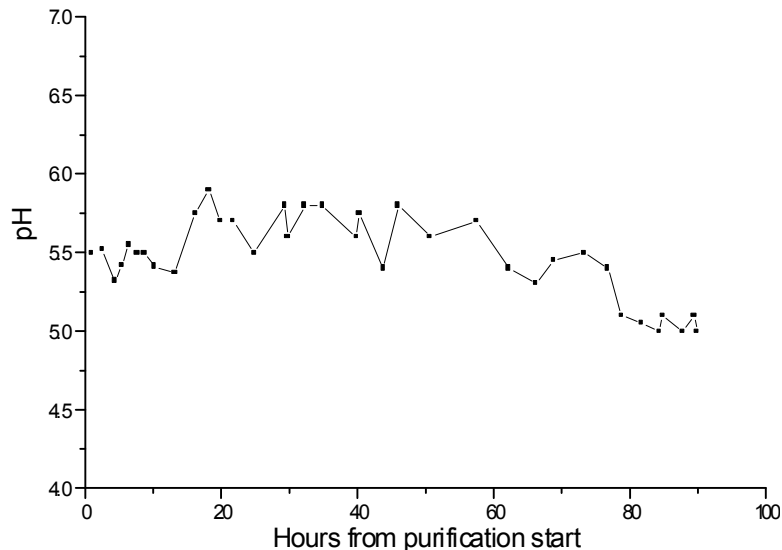


Fig. 9. Heavy water pH variations throughout purification cycle.

The purified water was supplied to tank B-4. The resultant parameters of the purified water sampled from tank B-4 were a  $1.18 \mu\text{S}/\text{cm}$  conductivity ( $24.5^\circ\text{C}$ ),  $\text{pH}=5.2$ , and a  $2.7 \cdot 10^{-3}$  Curie/l tritium oxide concentration.

In the further experiments scheduled by the Project 1145 Workplan, the heavy water quality was tested for the content of isotope D, for conductivity, and for pH.

The D concentration was determined up to  $\pm 0.06\%$  mol. in the  $3400 \text{ cm}^{-1}$  HDO peak using an IKS-26 infrared spectrometer, and up to  $\pm 0.03\%$  mol. by the differential pycnometer test. The conductivity was determined using a KL-2 meter. The pH value was determined using a pH-673 meter. The measurement results are displayed in Figs. 10-12. The deuterium concentration in the MAKET facility heavy water decreased steadily (Fig. 10). The conductivity and the pH value varied within admissible limits (Figs. 11 and 12).

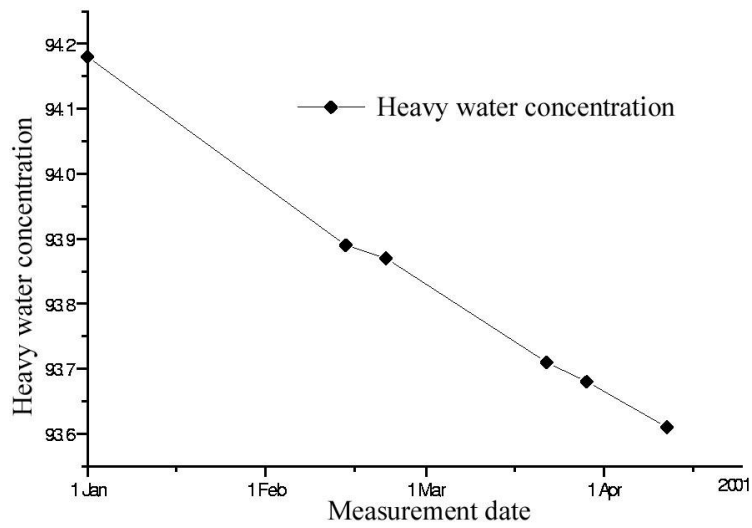


Fig. 10. Variations of heavy water concentration throughout the experiments.

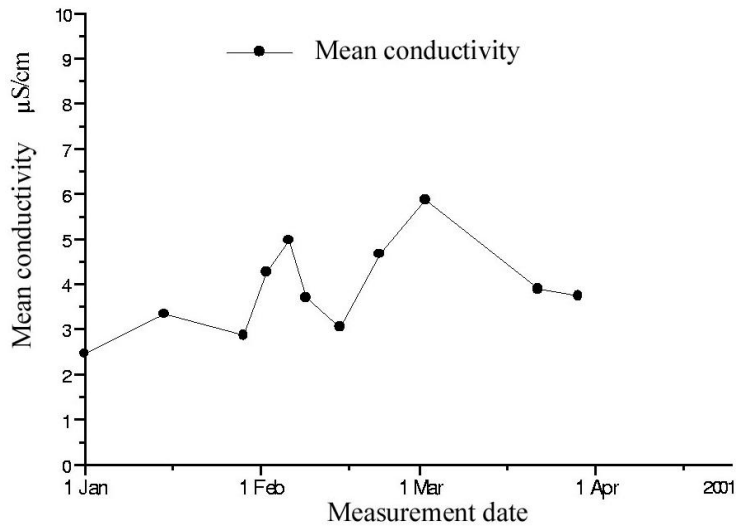


Fig. 11. Conductivity variations in heavy water samples throughout the experiments.

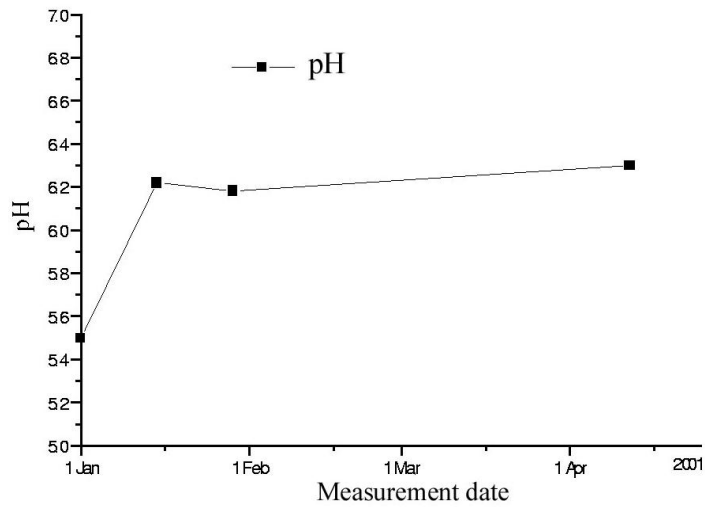


Fig. 12. Variations of pH value in heavy water samples throughout the experiments.

Table 10. The D<sub>2</sub>O analysis results.

Element	Results of analyzing the D <sub>2</sub> O samples, mass %				
	Plasma Spektromet			PLASMA-40	The mean
	28-34	29-27	32-22		
Fe	4·10 <sup>-6</sup>	6·10 <sup>-6</sup>	7·10 <sup>-6</sup>	-	6·10 <sup>-6</sup>
Co	2·10 <sup>-8</sup>	1·10 <sup>-7</sup>	<1·10 <sup>-8</sup>	-	4·10 <sup>-8</sup>
Mn	6·10 <sup>-8</sup>	1·10 <sup>-7</sup>	1·10 <sup>-7</sup>	-	9·10 <sup>-8</sup>
Cr	<3·10 <sup>-8</sup>	1·10 <sup>-7</sup>	<3·10 <sup>-8</sup>	-	5·10 <sup>-8</sup>
Mg	8·10 <sup>-7</sup>	1·10 <sup>-6</sup>	5·10 <sup>-7</sup>	-	8·10 <sup>-7</sup>
Sr	2·10 <sup>-8</sup>	2·10 <sup>-8</sup>	<1·10 <sup>-8</sup>	-	2·10 <sup>-8</sup>
Na	8·10 <sup>-5</sup>	1.6·10 <sup>-4</sup>	1·10 <sup>-4</sup>	0.9·10 <sup>-5</sup>	9·10 <sup>-5</sup>
Sn	<3·10 <sup>-7</sup>	<3·10 <sup>-7</sup>	<3·10 <sup>-7</sup>	-	3·10 <sup>-7</sup>
Zn	2·10 <sup>-6</sup>	2·10 <sup>-6</sup>	1·10 <sup>-6</sup>	-	2·10 <sup>-6</sup>
Au	<1·10 <sup>-7</sup>	<1·10 <sup>-7</sup>	<1·10 <sup>-7</sup>	-	<1·10 <sup>-8</sup>
In	<3·10 <sup>-7</sup>	<3·10 <sup>-7</sup>	<3·10 <sup>-7</sup>	-	<3·10 <sup>-7</sup>
B	5·10 <sup>-7</sup>	1·10 <sup>-6</sup>	5·10 <sup>-7</sup>	3.6·10 <sup>-7</sup>	8·10 <sup>-7</sup>
Mo	<1·10 <sup>-7</sup>	<3·10 <sup>-7</sup>	<1·10 <sup>-7</sup>	-	<2·10 <sup>-7</sup>
Zr	2·10 <sup>-8</sup>	3·10 <sup>-8</sup>	2·10 <sup>-8</sup>	1.8·10 <sup>-6</sup>	5·10 <sup>-7</sup>
Li	<2·10 <sup>-8</sup>	<2·10 <sup>-8</sup>	<2·10 <sup>-8</sup>	-	2·10 <sup>-8</sup>
Ni	<1·10 <sup>-7</sup>	<1·10 <sup>-7</sup>	<1·10 <sup>-7</sup>	-	<1·10 <sup>-7</sup>
V	<3·10 <sup>-8</sup>	<3·10 <sup>-8</sup>	<3·10 <sup>-8</sup>	-	<3·10 <sup>-8</sup>
Cu	2·10 <sup>-7</sup>	8·10 <sup>-7</sup>	1·10 <sup>-7</sup>	< 9·10 <sup>-7</sup>	5·10 <sup>-7</sup>
Ca	3·10 <sup>-6</sup>	5·10 <sup>-6</sup>	3·10 <sup>-6</sup>	-	4·10 <sup>-6</sup>
Al	8·10 <sup>-6</sup>	2·10 <sup>-5</sup>	5·10 <sup>-6</sup>	-	1·10 <sup>-5</sup>
K	<1·10 <sup>-6</sup>	<1·10 <sup>-6</sup>	<1·10 <sup>-6</sup>	-	<1·10 <sup>-6</sup>
Pb	<1·10 <sup>-7</sup>	<1·10 <sup>-7</sup>	<1·10 <sup>-7</sup>	-	<1·10 <sup>-7</sup>
Cd	4·10 <sup>-8</sup>	5·10 <sup>-8</sup>	<2·10 <sup>-8</sup>	< 9·10 <sup>-7</sup>	<5·10 <sup>-7</sup>
Ag	<1·10 <sup>-7</sup>	<1·10 <sup>-7</sup>	<1·10 <sup>-7</sup>	-	<1·10 <sup>-7</sup>
Ga	<5·10 <sup>-7</sup>	<5·10 <sup>-7</sup>	<5·10 <sup>-7</sup>	-	<5·10 <sup>-7</sup>
Ti	<1·10 <sup>-8</sup>	<1·10 <sup>-8</sup>	<1·10 <sup>-8</sup>	-	<1·10 <sup>-8</sup>
Sb	<3·10 <sup>-7</sup>	<3·10 <sup>-7</sup>	<3·10 <sup>-7</sup>	-	<3·10 <sup>-7</sup>
Be	<1·10 <sup>-8</sup>	<1·10 <sup>-8</sup>	<1·10 <sup>-8</sup>	-	<1·10 <sup>-8</sup>
La	<3·10 <sup>-7</sup>	<3·10 <sup>-7</sup>	<3·10 <sup>-7</sup>	-	<3·10 <sup>-7</sup>
Cl	<1·10 <sup>-4</sup>	<1·10 <sup>-4</sup>	≤1·10 <sup>-4</sup>	-	<1·10 <sup>-4</sup>
Gd	-	-	-	<6.1·10 <sup>-7</sup>	<6.1·10 <sup>-7</sup>
U	-	-	-	9.0·10 <sup>-6</sup>	9.0·10 <sup>-6</sup>
Dy	-	-	-	< 6.1·10 <sup>-7</sup>	<6.1·10 <sup>-7</sup>

Besides, to certify the heavy water quality, two heavy water samples were taken by a job-oriented probe for the element-by-element chemical analysis. The heavy water samples were also tested for content of metals by the emission spectroscopy method using the PERKIN-

ELMER Co.-made PLASMA-40 instrument and the Baird Co.-made Plasma Spektromet instrument (see Table 10). The samples for the latter instrument were taken on 29 March 2001 from cells 28-34 (the tank periphery,  $\chi=4.32 \mu\text{S/cm}$ ), 29-27 (the tank center,  $\chi=3.10 \mu\text{S/cm}$ ), and 32-22 (near the SBM,  $\chi=3.79 \mu\text{S/cm}$ ) to a quartz vessel. The samples for the former instrument were taken on 16 January 2001 from cell 38-26 to a quartz vessel; the initial conductivity was  $\chi=4.25 \mu\text{S/cm}$ .

The element-by-element analysis results have also confirmed a low content of the limiting impurities in the MAKET facility heavy water.

### 7. Monitoring the MAKET facility power

During the feasibility study stage of the MAKET facility experiments, the desired statistical accuracy of the eventual results were found to necessitate that the integral and shutter chambers with the sample-detector pairs should be irradiated at the MAKET power levels differing by two or three orders. With the view to reliable determination of the power levels, the job-oriented techniques were developed basing on the outfit that included the KIR reactometer counting unit in the KNT-54-3 pulsed fission chamber, “Vector” standard-based electronics, and IBM PC with a purpose-oriented data acquisition interface and software for online graphic mapping the data in each 5.05 s. The number of counts for each of the mapped dots was determined by averaging 23 measurements of equal accuracy.

To attain the desired accuracy in monitoring the neutron flux density throughout the experiments, the ionization chamber was fixed to a stiff hanger (the  $75 \times 1.5$ -mm diameter dry channel made of the alloy indicated in Table 2 and mounted in cell 34-34 at 3700 mm as marked from the top of the lower supporting lattice). The performance linearity of the KIR reactometer was checked by the reactor runaway technique. For that purpose, the MAKET critical facility was turned into its supracritical state with a 60-s runaway period. Fig. 3 shows the linearity preservation (on logarithmic scale) of the KIR counting unit, which visualizes the feasibility for the KIR counting unit to be used within a  $\sim 10^1$ - $10^6$  pulse/s range.

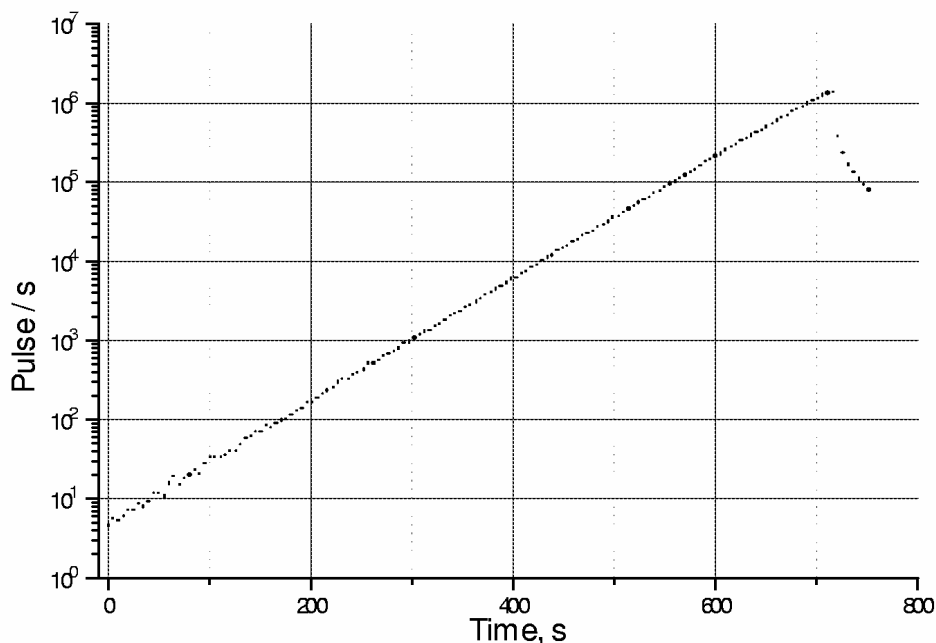


Fig. 13. The KIR reactometer reading under MAKET reactor runaway mode.

Figs. 14 and 15 exemplify different reactor operation modes, namely, at a high power level (the samples are irradiated for being  $\gamma$ -spectrometered) and at a low power level (the samples are irradiated for being SSNTD-measured).

The relative-to-absolute power measurement unit conversion was realized by the techniques based on determining the total number of the fission events in the  $^{235}\text{U}$  nuclei of the fuel channel in terms of the method described in Subsection 1.10 below.

In some experiments that necessitate a high neutron flux, the power level was additionally checked by the standard techniques for irradiating the many-component samples placed at a 569-mm height in cell 34-26. Tables 11 and 12 present the results of comparing between the power levels obtained with the KIR and by  $\gamma$ -spectrometry.

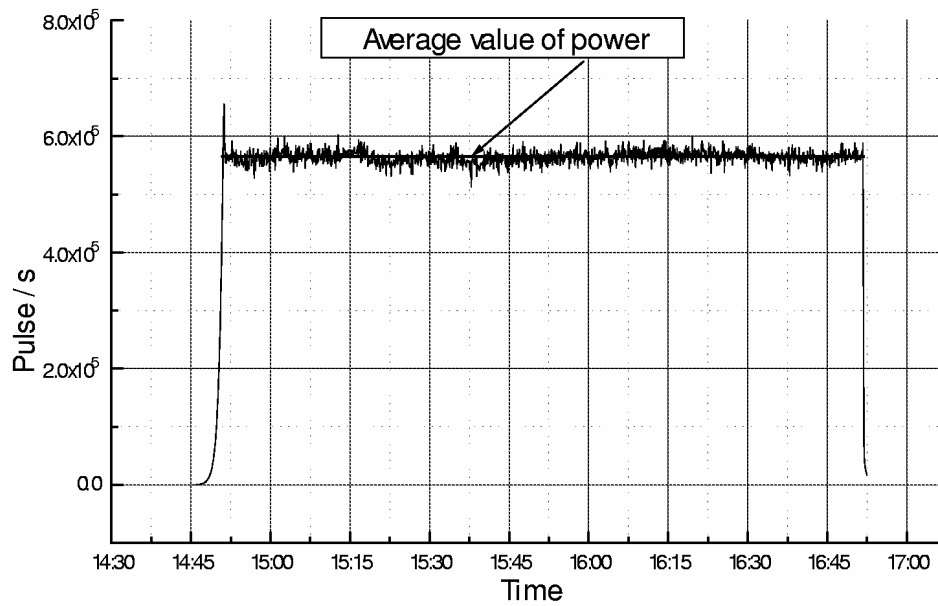


Fig. 14. Power level records when irradiating the samples to be  $\gamma$ -spectrometered.

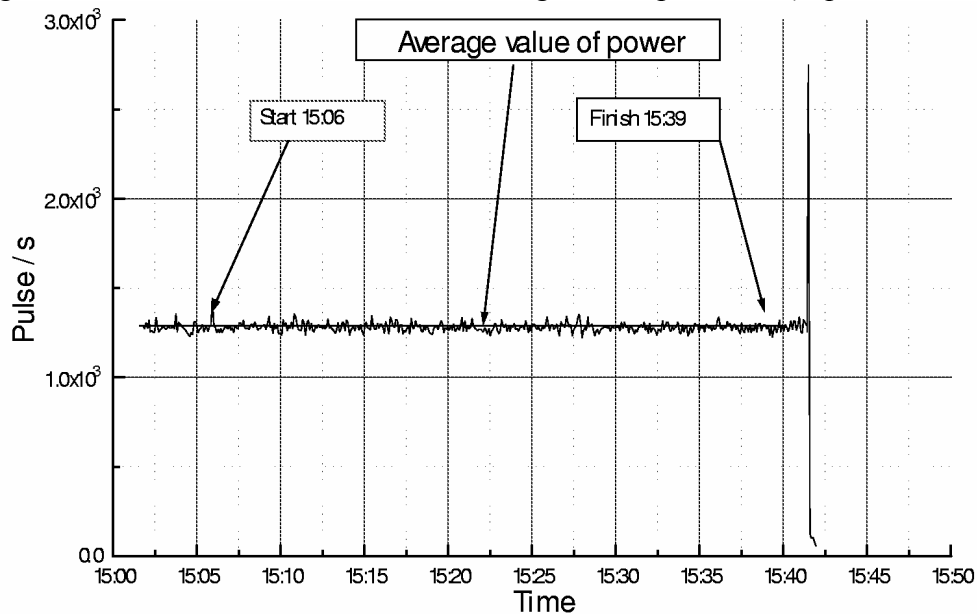


Fig. 15. Power level records when irradiating the SSNTDs in the shutter chambers.

Table 11. Comparison between the power levels obtained with KIR and by  $\gamma$ -spectrometry in lattice 21-1(M2).

	Experiment 7*	Experiment 8	Experiment 9	Experiment 10	Experiment 11
$^{176}\text{Lu}(n, \gamma)$	1	1.061±0.098	1.158±0.111	1.166±0.108	1.145±0.107
$^{196}\text{Au}(n, \gamma)$	1	1.048±0.046	1.108±0.051	1.183±0.054	1.117±0.049
$^{55}\text{Mn}(n, \gamma)$	1	1.067±0.045	1.137±0.049	1.172±0.049	1.100±0.044
The mean	1	1.058±0.030	1.126±0.034	1.176±0.034	1.111±0.032
KIR	1	1.008±0.001	1.069±0.001	1.041±0.000	1.091±0.000
Ratio	1	1.049±0.030	1.053±0.032	1.046±0.033	1.018±0.029

\* The experiment as numbered in Table 7.

Table 12. Comparison between the power levels obtained with KIR and by  $\gamma$ -spectrometry in lattice 21-2.

	Experiment 23*	Experiment 31	Experiment 32	Experiment 33	Experiment 34
$^{176}\text{Lu}(n, \gamma)$	1	1.066±0.093	0.986±0.092	0.977±0.092	0.981±0.092
$^{196}\text{Au}(n, \gamma)$	1	1.006±0.045	0.990±0.045	0.943±0.043	0.990±0.046
$^{55}\text{Mn}(n, \gamma)$	1	0.992±0.042	1.003±0.042	0.966±0.041	0.990±0.045
Среднее	1	1.005±0.029	0.996±0.029	0.957±0.028	0.989±0.030
KIR	1	0.965±0.001	0.972±0.001	0.965±0.000	0.976±0.000
Ratio	1	1.041±0.030	1.025±0.030	0.992±0.029	1.014±0.031

\* - The experiment as numbered in Table 7.

From Tables 11 and 12 it follows that the correlation between the KIR readings and the measured reaction rates is within the experimental errors, thus making sure that the KIR readings used in monitoring different power levels are reliable.

## 8. Meters

The numbers of radioactive nuclei produced in the irradiated experimental samples were determined by  $\gamma$ -spectrometry method using two CANBERRA Co.-made spectrometers, one with a Ge detector and another with a Ge-Li detector. The numbers of nuclei in non-irradiated samples were determined by gravimetric techniques using the SARTORIUS Co.-made BP-61 analytical balance.

The Ge detector-based spectrometer included a GC-2518 Ge detector, an integrated 1510 signal processor (a 6000V power supply, a spectrometric amplifier, and a 100-MHz 8192-channel ADC), a SYSTEM-100 board that emulates a multi-channel analyzer in IBM PC (the full card of the PC standard for 8192 channels with DMA memory). The energy resolution of the spectrometer was 1.8 keV in the  $^{60}\text{Co}$  1332 keV  $\gamma$ -line.

The Ge-Li detector based spectrometer included a DGDK-65B coaxial Ge-Li detector, a P-218 preamplifier, and the units of the NOKIA LP4900B analyzer (a LPA 4910.2 amplifier, a 4911.4 ADC, and a LPG 4931 high-voltage power supply). The energy resolution of the spectrometer was 2.5 keV in the  $^{60}\text{Co}$  1332 keV  $\gamma$ -line.

The measured  $\gamma$ -spectra were processed by the GENIE2000 code system [3]. The PCNUDAT nuclear database [4] was used to identify the produced nuclides and to calculate the reaction rates presented in Table 1.

The two  $\gamma$ -source method was used to determine the ultimate load of the two spectrometers, which did not exceed 5% for GC-2518 and 3% for DGDK-65B. To warrant these conditions, the experimental samples were measured with GC-2518 starting from different heights down to 40 mm to exclude the cascade summation effects. The DGDK-65B measurements were taken after the necessary cooling time at a 40-mm height only. The cascade summation effects were estimated for both detectors using  $^{24}\text{Na}$  and  $^{60}\text{Co}$  at a 40-mm height and were found to be within the statistical errors.

The absolute detection efficiency was determined using the  $\gamma$ -sources from the OSGI-3 #9402 set of sources certified by the D.I.Mendeleev State Metrology Institute. The set includes  $^{54}\text{Mn}$ ,  $^{57}\text{Co}$ ,  $^{60}\text{Co}$ ,  $^{88}\text{Y}$ ,  $^{109}\text{Cd}$ ,  $^{113}\text{Sn}$ ,  $^{133}\text{Ba}$ ,  $^{137}\text{Cs}$ ,  $^{139}\text{Ce}$ ,  $^{152}\text{Eu}$ ,  $^{228}\text{Th}$ , and  $^{241}\text{Am}$ . Use was also made of  $^{22}\text{Na}$  from the OSGI #237 set certified by the VNIIFTRI Scientific and Production Amalgamation. The certification dates, the activity, and the nuclear data used in calculating the absolute efficiency were taken to conform to the manufacturer's rated data.

In this case, the absolute detection effectiveness of the spectrometer for the energy, which corresponds to the  $\gamma$ -line energy of the measured source, can be presented as

$$\varepsilon_{abs}^E = \frac{SPA}{A \cdot \eta} , \quad (1)$$

where  $SPA$  is the count rate in the total absorption peak at energy  $E$  (count/s);

$\eta$  is the absolute  $\gamma$ -line  $\gamma$ -rays yield;

$A$  is the certified  $\gamma$ -source activity reduced to the measurement moment.

The analytical representation of the detection efficiency as a function of height and energy obtained for the GC-2518 detector by the least squares spline method is

$$\varepsilon(E, H) = \varepsilon(E)_{base} \cdot \left[ \frac{q_1 + q_2 \cdot \ln E + H_{base}}{q_1 + q_2 \cdot \ln E + H} \right]^2 \quad (2)$$

where  $\varepsilon_{base}$  is the detection efficiency for the 80-mm base height, whose analytical representation is the same as expression (3) with the appropriate coefficients;

$q_1, q_2$  are the parameters determined by least squares method.



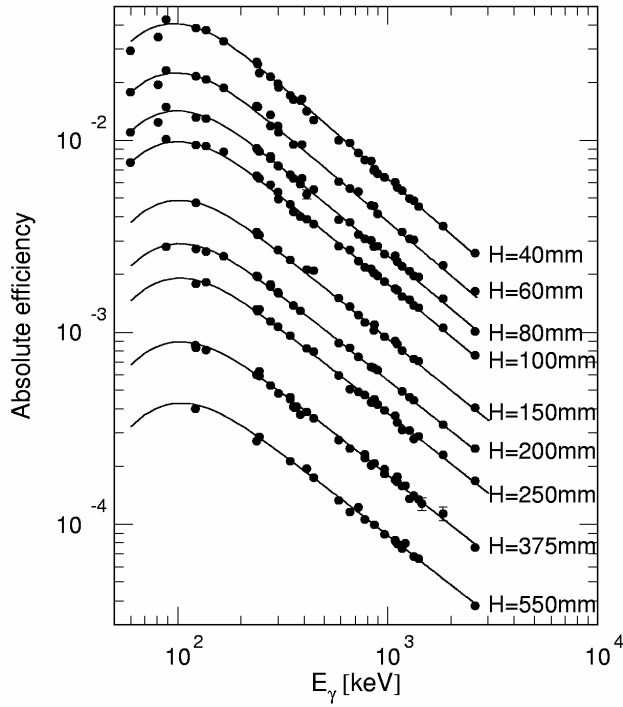


Fig. 16. The experimental values and the analytical dependences of the GC-2518 instrument detection efficiency at different heights.

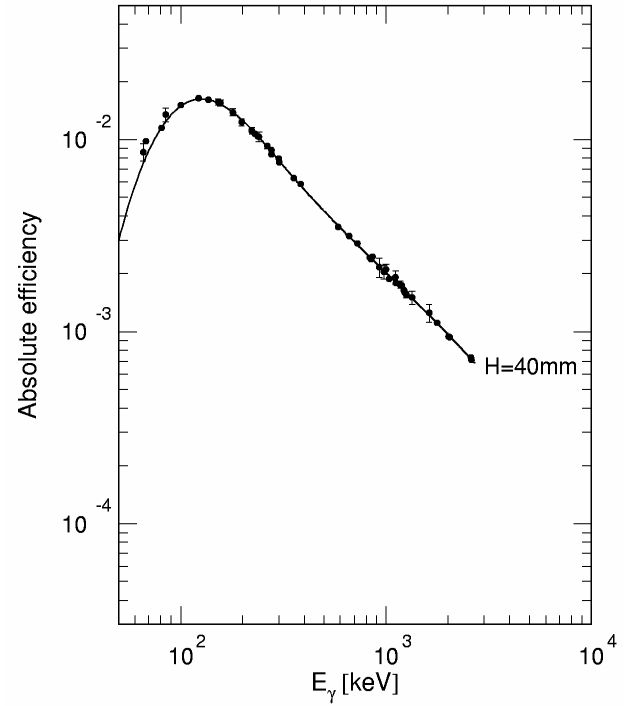


Fig. 17. The experimental values and the analytical dependences of the DGDK-65V instrument detection efficiency at a 40-mm height.

The analytical representation of the detection efficiency as a function of height and energy obtained for the DGDK-65V detector at a 40-mm height by the least squares spline method is

$$\varepsilon(E) = \exp \left[ \sum_{i=k}^{k+3} P_i \cdot (\ln E)^{i-k} \right], \quad (3)$$

where

$$k = \begin{cases} 1, & \text{at } \ln E < \ln E_0 \\ 5, & \text{at } \ln E > \ln E_0 \end{cases}$$

where  $E_0$  is the boundary point between two energy ranges;

$P_1, \dots, P_8$  are the polynomial coefficients;

Figs. 16 and 17 show the dependence character of the GC-2518 and DGDK-65V detection efficiency, respectively.

The above-described techniques were somewhat modified when determining the number of nuclei in the high U-enriched experimental samples ( $\sim 90\%$  of  $^{235}\text{U}$ ) used in the reported measurements and in determining the MAKET facility power. The modification was dictated primarily by the requirement of the least error in the  $^{235}\text{U}$  fission rate. Because of a great number of the samples to be calibrated (89 samples), the measurement geometry was altered, namely, the experimental samples were placed right on the cryostat surface at “zero” height, rather than at 40 mm. In such a way, the time of accumulating the necessary statistics for each sample was much reduced and the planned measurement accuracy was attained.

In that case, the number of  $^{235}\text{U}$  nuclei in the experimental samples was determined without using the absolute spectrometer efficiency; instead, use was made of the special-purpose standard certified by the VNIIFTRI Scientific and Production Amalgamation [5, 6]. The standard is a high-enriched U layer shaped to be a round spot of 8-mm diameter and  $174 \mu\text{g}/\text{cm}^2$  thickness, with number of nuclei  $N_{st.}^{235\text{U}} = 2.24 \cdot 10^{17} (\pm 2\%)$ . The layer is applied on a 200- $\mu\text{m}$  thick Al substrate. The isotopic composition of uranium is  $N_{st.}^{234\text{U}} = (1.240 \pm 0.008)\%$ ;  $N_{st.}^{235\text{U}} = (89.58 \pm 0.03)\%$ ;  $N_{st.}^{236\text{U}} = (0.26 \pm 0.004)\%$ ;  $N_{st.}^{238\text{U}} = (8.92 \pm 0.03)\%$ .

The measurement identity was preserved by placing the standard in the same geometry as in the case of experimental samples (i.e. with the U layer down) behind a 85- $\mu\text{m}$  Al foil shielding. In such a way, the equivalent Al thickness was preserved in the experimental sample and in the standard (see Tables 26 and 27). In the above standard, the count rate in the  $^{235}\text{U}$  total absorption peak at  $E_\gamma = 185.715$  was measured keV to be  $SPA_{st.}^{235\text{U}} = (0.800 \pm 0.002)$  count/s. In that case, the numbers of  $^{235}\text{U}$  nuclei and their errors in the experimental samples were calculated as

$$n_{\text{exp.samp.}}^{235\text{U}} = N_{st.}^{235\text{U}} \cdot \frac{SPA_{\text{exp.samp.}}^{235\text{U}}}{SPA_{st.}^{235\text{U}}}, \quad (4)$$

$$\Delta n_{\text{exp.samp.}}^{235\text{U}} = n_{\text{exp.samp.}}^{235\text{U}} \cdot \sqrt{\left(\frac{\Delta N_{st.}^{235\text{U}}}{N_{st.}^{235\text{U}}}\right)^2 + \left(\frac{\Delta SPA_{st.}^{235\text{U}}}{SPA_{st.}^{235\text{U}}}\right)^2 + \left(\frac{\Delta SPA_{\text{exp.samp.}}^{235\text{U}}}{SPA_{\text{exp.samp.}}^{235\text{U}}}\right)^2}$$

where  $n_{\text{exp.samp.}}^{235\text{U}}$  is the number of  $^{235}\text{U}$  in the experimental samples;

$N_{st.}^{235\text{U}}$  is the number of  $^{235}\text{U}$  in the standard;

$SPA_{\text{exp.samp.}}^{235\text{U}}$  is the count rate in the  $^{235}\text{U}$  total absorption peak at  $E_\gamma = 185.715$  keV in an experimental sample;

$SPA_{st.}^{235\text{U}}$  is the count rate in the  $^{235}\text{U}$  total absorption peak at  $E_\gamma = 185.715$  keV in the standard.

The techniques for chemical treatment of SSNTDs and for inspecting and counting the nuclear tracks have been realized at VNIIEF and is described in detail in other sections of this Report.

## 9. The measured parameters

Conforming to the Project 1145 Workplan (see Table 1), the parameters presented in the Table were measured by two techniques, namely, by  $\gamma$ -spectrometry and using SSNTDs.

### 9.1 The $\gamma$ -spectrometry method

The method is based on the presentation of the number of radioactive nuclei of a nuclide  ${}^A_{Z^*}B$

produced in an irradiated sample  ${}^A_Z B$  as

$$N_{Z^*B}^{A^*}(t) = \frac{SPA_{Z^*B}^{A^*}(t)}{(\lambda \cdot \eta \cdot \varepsilon_{\text{abs}})_{Z^*B}^{A^*}}, \quad (5)$$

where  $N_{z^*B}^{A^*}(t)$  is the number of the produced nuclei at moment  $t$ ;

$SPA_{z^*B}^{A^*}(t)$  - is the count rate in the total absorption peak of nuclide  $_{z^*B}^{A^*}$  at energy  $E$  at moment  $t$ (count/s);

$\lambda_{z^*B}^{A^*}$  - is the decay constant of nuclide  $_{z^*B}^{A^*}$ ;

$\eta_{z^*B}^{A^*}$  - is the absolute  $\gamma$ -rays yield of a measured  $\gamma$ -line;

$\mathcal{E}_{abs}^{A^*B}$  - is the detection efficiency for a measured  $\gamma$ -line;

On the other hand, the nuclide  $_{z^*B}^{A^*}$  production rate when irradiating the nuclide  $_{z^*B}^{A^*}$  in the neutron flux due to the (n, $\gamma$ )-reaction ( $A^* = A + 1, Z^* = Z$ ), (n,2n)-reaction ( $A^* = A - 1, Z^* = Z$ ), (n,p)-reaction ( $A^* = A, Z^* = Z - 1$ ), (n, $\alpha$ )-reaction ( $A^* = A - 3, Z^* = Z - 2$ ), and (n,n')-reaction ( $A^* = A, Z^* = Z$ ) is calculated by solving the differential equation

$$\frac{dN_{z^*B}^{A^*}(t)}{dt} = -\lambda_{z^*B}^{A^*} \cdot N_{z^*B}^{A^*}(t) + N_{z^*B}^{A^*} \cdot \int_0^{\infty} \sigma_{z^*B}^{A^*}(E) \cdot \varphi(E) dE \quad (6)$$

with the initial condition  $N_{z^*B}^{A^*}(0) = 0$ ,

where  $N_{z^*B}^{A^*}$  is the number of nuclei produced;

$N_{z^*B}^{A^*}$  is the number of nuclei in an irradiated sample;

$\sigma_{z^*B}^{A^*}(E)$  is the cross section of the measured reaction, which may be a (n, $\gamma$ ) radiative trapping reaction; a (n,f) fission reaction, as well as a (n, n'), (n, p), (n, 2n), or (n,  $\alpha$ ) reaction;

$\varphi(E)$  is the neutron flux density.

In this case,

$$R_x = \int_0^{\infty} \sigma_{z^*B}^{A^*}(E) \cdot \varphi(E) dE \quad (7)$$

is defined to be a respective reaction rate.

Since the critical facility is used in irradiating the experimental samples, the latter were loaded before the facility reached its rated power. In such a way, a definite uncertainty arises due to the parameters of reaching the steady-state power. If  $t_1$  is taken to be the moment of starting the steady-state operation conditions, and  $t_3$  to be the irradiation stop moment, then the neutron flux variation before reaching the steady-state irradiation mode can be presented as

$$\varphi(E, t) = \varphi_0(E) \cdot e^{\frac{t-t_2}{T}} \quad (8)$$

where  $t$  is the current time within a  $t_1 - t_2$  interval;

$T$  is the critical facility runaway period;

$\varphi_0(E)$  is the neutron flux density at the sample irradiation point under steady-state operation conditions.

Using (7) and (8), the equation (6) can be presented as

$$\frac{d N_{z^*B}^{A^*}}{dt} = -\lambda_{z^*B}^{A^*} \cdot N_{z^*B}^{A^*} + N_{zB}^A \cdot e^{\frac{t-t_2}{T}} \cdot R_{x_0}^{AB} \quad (9)$$

Solving (9) with initial conditions  $N_{z^*B}^{A^*}(0) = 0$  gives

$$N_{z^*B}^{A^*}(t) = R_{x_0}^{AB} \cdot N_{zB}^A \cdot \frac{T \cdot e^{-\frac{t_2}{T}} \cdot (e^{\frac{t}{T}} - e^{-\lambda_{z^*B}^{A^*} \cdot t})}{1 + \lambda_{z^*B}^{A^*} \cdot T} \quad (10)$$

Under the steady-state operation conditions, the nuclide buildup within the interval from  $t_2$  to  $t_3$  is described as

$$\frac{d N_{z^*B}^{A^*}(t)}{dt} = -\lambda_{z^*B}^{A^*} \cdot N_{z^*B}^{A^*}(t) + N_{zB}^A \cdot R_{x_0}^{AB} \quad (11)$$

with the initial condition

$$N_{z^*B}^{A^*}(t_2) = R_{x_0}^{AB} \cdot N_{zB}^A \cdot \frac{T \cdot e^{-\frac{t_2}{T}} \cdot (e^{\frac{t_2}{T}} - e^{-\lambda_{z^*B}^{A^*} \cdot t_2})}{1 + \lambda_{z^*B}^{A^*} \cdot T} \quad (12)$$

Solution for (11) with initial condition (12) is

$$N_{z^*B}^{A^*}(t_3) = R_{x_0}^{AB} \cdot N_{zB}^A \cdot F(t_2, t_3) \quad (13)$$

In this case, the expression for  $F(t_2, t_3)$  can be presented as

$$F(t_2, t_3) = \frac{1}{\lambda^{Z^*B}} \left\{ \left[ \frac{\lambda^{Z^*B} \cdot T}{1 + \lambda^{Z^*B} \cdot T} \cdot \left( 1 - e^{-\frac{1 + \lambda^{Z^*B} \cdot T}{T} \cdot t_2} \right) - 1 \right] \cdot e^{-\lambda^{Z^*B} \cdot (t_3 - t_2)} + 1 \right\} \quad (14)$$

If the rated power is reached instantaneously, i.e.,  $T \rightarrow 0$ , the expression (14) turns into the standard relation

$$F(t_2, t_3) = \frac{1 - e^{-\lambda^{Z^*B} \cdot (t_3 - t_2)}}{\lambda^{Z^*B}} \quad (15)$$

The number of the produced nuclei  $N^{Z^*B}$  is determined by  $\gamma$ -spectrometry, while the number of nuclei in an experimental sample  $N^{AB}$ , is determined by the gravimetric techniques using a SARTORIUS Co.-made BP61 analytical balance. In this case, the Workplan-scheduled (n, $\gamma$ ), (n,n'), (n,p), (n,2n), and (n, $\alpha$ ) reaction rates are calculated as

$$R_{x_0}^{Z^*B} = \frac{N^{Z^*B}}{N^{AB} \cdot F(t_2, t_3)} = \left( \frac{SPA(t_3)}{\lambda \cdot \eta \cdot \varepsilon_{abs} \cdot F(t_2, t_3)} \right)^{Z^*B} \cdot \left( \frac{M}{m \cdot x \cdot y} \right)^{Z^*B} \cdot \frac{1}{N_{Av}} \quad (16)$$

where  $SPA(t_3)$  is the count rate in the total absorption peak at energy  $E$  recorded as a result of the produced nuclide decay and reduced to the irradiation stop moment ( $t_3$ );

$\lambda$  is the decay constant of a produced nuclide;

$\eta$  is the absolute  $\gamma$ -rays yield at a given energy of a produced nuclide;

$\varepsilon_{abs}$  is the relative or absolute spectrometer efficiency at the measured  $\gamma$ -line energy;

$M$  is molecular weight;

$m$  is weight of an experimental sample;

$x$  is the content of a given element in the experimental sample;

$y$  is the content of a given isotope in the element.

The errors in the measured reaction rates were measured by the standard error transfer formula.

The  $^{235}\text{U}$  fission rate was determined using expression (4):

$$\begin{aligned} R_{(n,f)}^{235U} &= \frac{1}{J^{f.p.}} \cdot \frac{N^{f.p.}}{n_{\text{exp.samp}}^{235U}} \cdot \frac{1}{F^{f.p.}(t_2, t_3)} = \\ &= \frac{1}{J^{f.p.}} \cdot \frac{SPA^{f.p.}(t_3)}{N_{st}^{235U} \cdot SPA^{235U}} \cdot \frac{SPA_{st}^{235U}}{(\lambda \cdot \eta \cdot \varepsilon)^{f.p.}} \cdot \frac{1}{F^{f.p.}(t_2, t_3)} \end{aligned} \quad (17)$$

where  $N^{f.p.}$  is the number of the fission product nuclei produced in an experimental sample;

$n_{\text{exp.samp.}}^{235\text{U}}$  is the number of  $^{235}\text{U}$  nuclei in the experimental sample;

$J^{f.p.}$  is the cumulative yield of the a  $^{235}\text{U}$  fission product;

$F(t_2, t_3)$  is the time function obtained by formula (14) to allow for the fission product decay during irradiation;

$SPA^{f.p.}(t_3)$  is the count rate (reduced to the irradiation stop moment) in the total absorption peak recorded as a result of the fission product decay;

$SPA^{235\text{U}}$  is the count rate in the total absorption peak recorded as a result of  $^{235}\text{U}$  decay;

$\lambda^{f.p.}$  is the decay constant of a recorded fission product;

$\eta^{f.p.}$  is the absolute  $\gamma$ -rays yield of a recorded fission product;

$\varepsilon^{f.p.}$  is the absolute spectrometer efficiency when recording a measured fission product  $\gamma$ -line.

Since two fission products ( $^{143}\text{Ce}$  and  $^{97}\text{Zr}$ ) were used simultaneously in determining the fission reaction rate, the expressions to calculate the  $^{235}\text{U}$  fission rate and its errors turn into

$$R_{(n,f)}^{235\text{U}} = \frac{\bar{Y}}{n_{\text{exp.samp.}}^{235\text{U}}} = \frac{SPA_{st.}^{235\text{U}}}{N_{st.}^{235\text{U}} \cdot SPA^{235\text{U}}} \cdot \bar{Y} \quad (18)$$

$$\Delta R_{(n,f)}^{235\text{U}} = R_{(n,f)}^{235\text{U}} \cdot \sqrt{\left(\frac{\Delta SPA_{st.}^{235\text{U}}}{SPA_{st.}^{235\text{U}}}\right)^2 + \left(\frac{\Delta SPA^{235\text{U}}}{SPA^{235\text{U}}}\right)^2 + \left(\frac{\Delta N_{st.}^{235\text{U}}}{N_{st.}^{235\text{U}}}\right)^2 + \left(\frac{\Delta \bar{Y}}{\bar{Y}}\right)^2}$$

where

$$\bar{Y} = \frac{\frac{Y^{143\text{Ce}}}{(\Delta Y^{143\text{Ce}})^2} + \frac{Y^{97\text{Zr}}}{(\Delta Y^{97\text{Zr}})^2}}{\frac{1}{(\Delta Y^{143\text{Ce}})^2} + \frac{1}{(\Delta Y^{97\text{Zr}})^2}} \quad (19)$$

$$(\Delta \bar{Y})^2 = \frac{1}{\frac{1}{(\Delta Y^{143\text{Ce}})^2} + \frac{1}{(\Delta Y^{97\text{Zr}})^2}}$$

where

$$Y^{143\text{Ce}} = \frac{SPA^{143\text{Ce}}}{J^{143\text{Ce}} \cdot (\lambda \cdot \eta \cdot \varepsilon)^{143\text{Ce}} \cdot F^{143\text{Ce}}(t_2, t_3)} \quad (20)$$

$$Y^{97\text{Zr}} = \frac{SPA^{97\text{Zr}}}{J^{97\text{Zr}} \cdot (\lambda \cdot \eta \cdot \varepsilon)^{97\text{Zr}} \cdot F^{97\text{Zr}}(t_2, t_3)} \quad (21)$$

The  $^{143}\text{Ce}$  and  $^{97}\text{Zr}$  nuclides were chosen to be the measured reaction products because the two nuclides satisfy the following requirements:

- ◇ the values of their fission product yields must be high (a few per cent);
- ◇ they must have short-lived precursors, for all of them to decay into a recorded fission product by the measurement start moment;
- ◇ their  $\gamma$ -lines must be sufficiently intense and well-identifiable by  $\gamma$ -spectrometry;
- ◇ they must be supported by nuclear data known to sufficiently high accuracy.

In terms of the above requirements, the  $^{143}\text{Ce}$  and  $^{97}\text{Zr}$  nuclides are most preferable; they are produced in the following chains:

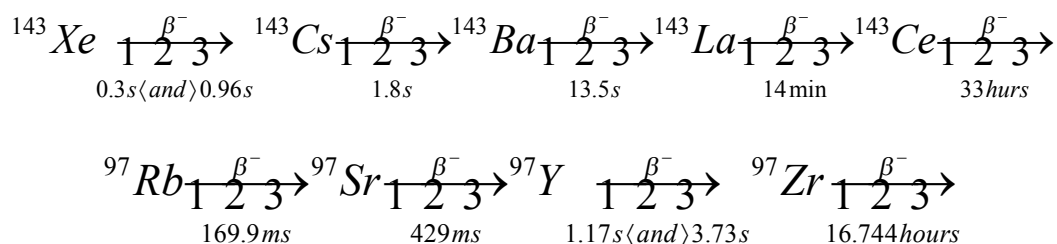


Table 13 presents the  $^{143}\text{Ce}$ ,  $^{97}\text{Zr}$  и  $^{235}\text{U}$  nuclear data [4], [7].

Table 13. Nuclear-physics characteristics of the nuclides.

Nuclide	$E_\gamma$ , keV	$\eta_\gamma$ , %	$T_{1/2}$ , s	$\epsilon$ , %	J, %
$^{143}\text{Ce}$	293.266	$42.8 \pm 0.5$	$(1.192 \pm 0.002) \cdot 10^5$	$2.03 \pm 0.04$	$5.95 \pm 0.04$
$^{97}\text{Zr}$	743.36	$93.06 \pm 0.16$	$(6.0278 \pm 0.0040) \cdot 10^4$	$0.843 \pm 0.011$	$5.95 \pm 0.09$

From Table 13 it follows that the  $^{143}\text{Ce}$  yield of the thermal neutron-induced  $^{235}\text{U}$  fission is known up to  $\sim 0.7\%$ , and the  $^{143}\text{Ce}$   $\gamma$ -rays yield from the measured  $\gamma$ -line ( $E_\gamma = 293.27$  keV) up to  $\sim 1.2\%$ . It is seen also that the  $^{97}\text{Zr}$  yield of the thermal neutron-induced  $^{235}\text{U}$  fission is known up to  $\sim 1.4\%$ , and the  $^{97}\text{Zr}$   $\gamma$ -rays yield from the measured  $\gamma$ -line ( $E_\gamma = 743.36$  keV) up to  $\sim 0.2\%$ . The error of determining the fission reaction rate can conveniently be reduced by simultaneous using the two fission products.

## 9.2 The SSNTD techniques

Unlike the  $\gamma$ -spectrometry, the input expressions get much simplified because the number of the produced tracks is in direct ratio to the fission reaction rate.

In this case, the ratio of the fission reaction rates is

$$\frac{R_{(n,f)}^x}{R_{(n,f)}^{\text{reper}}} = \frac{T^x}{T^{\text{reper}}} \cdot \frac{N^{\text{reper}}}{N^x} \cdot \frac{\xi^{\text{reper}}}{\xi^x} \quad (22)$$

where  $T^x$  is the number of the recorded fission fragment tracks of the nuclides presented in Table 1;

$T^{reper}$  is the number of the recorded fission fragment tracks of the nuclides, whose fission cross sections have been well-known ( $^{235}\text{U}$ ,  $^{239}\text{Pu}$ );

$N^x$  and  $N^{reper}$  are the numbers of nuclei in the experimental samples and in benchmarks, respectively;

$\xi^x$  and  $\xi^{reper}$  are the SSNTD sensitivities when recording the fission events in the benchmarks and samples, respectively:

$$R_{(n,f)}^x = \frac{T^x}{\xi^x \cdot N^x} \cdot \frac{1}{t} = \frac{T^x}{N^{eff}} \cdot \frac{1}{t} \quad (23)$$

The absolute number,  $N^x$ , in the experimental samples was determined by the  $\alpha$ - and  $\gamma$ -spectrometry techniques with calibration in a certificated thermal column. The SSNTD techniques are described in more detail in the VNIIEF section of this Report.

### 10. Determination of the absolute power of the MAKET facility with the experimental lattices

The absolute power of the MAKET facility with the experimental lattices 21-1-5(M2) and 21-2(M1) was determined by summing up the energy deposits in each of the fuel channels (FC). So, the sought value can be presented as

$$W = \sum_{i=1}^n W_i = E_f \cdot P_f = E_f \cdot \sum_{i=1}^n N_i^{TK} \cdot \overline{R}_{(n,f),i}^{235\text{U}} \quad (24)$$

where  $W$  is energy deposit in the MAKET core;

$W_i$  is energy deposit in the I-th FC;

$n$  is number of FCs in a lattice;

$P_f$  is number of fission events in the core in unit time;

$E_f$  is energy deposit in a single  $^{235}\text{U}$  fission event, disregarding the energy carried away by an antineutrino and the energy deposit in the decays of the fission products of a high decay time,  $E_f = 194.0833$  MeV (this value was selected to conform to the MCNP-4B code calculations);

$N_i^{TK}$  is number of  $^{235}\text{U}$  nuclei in the I-th FC;

$\overline{R}_{(n,f),i}^{235\text{U}}$  is the absolute  $^{235}\text{U}$  fission reaction rate as averaged over the I-th FC volume.

The number of  $^{235}\text{U}$  nuclei is determined as

$$N_i^{TK} = \frac{M_i \cdot N_{Av}}{A}, \quad (25)$$

where  $M_i$  is the  $^{235}\text{U}$  within the i-th FC volume;

$N_{Av}$  is the Avogadro number ( $6.023 \times 10^{23} \text{ mol}^{-1}$ );

$A$  is the  $^{235}\text{U}$  atomic mass (235.0409).



The FC energy deposit is determined by measuring the absolute  $^{235}\text{U}$  fission reaction rates in fuel elements (the measurement techniques are described in Section 1.9.1 above). In this case, the fuel elements must be scanned throughout the FC length. This procedure is replaced by sticking the experimental samples of the same composition to the FC external surface with introducing the appropriate corrections.

The above approach gives rise to difficulties due to high labour hours requirements of determining the number of  $^{235}\text{U}$  nuclei in the experimental samples, as well as of measuring the  $\gamma$ -ray intensity of the fragment nuclides produced in the  $^{235}\text{U}$  fission. The labour hours can be much reduced if allowance is made for the fact that the rates of the  $^{235}\text{U}(n,f)$  reaction and  $^{63}\text{Cu}(n,\gamma)$  radiative trapping reaction are distributed alike along the FC axis, considering the FC orientation.

On introducing the concept of nonuniformity coefficient  $K_z$  defined to be

$$K_{z,i}(z) = \frac{R_i(z)}{\bar{R}_i} \quad (26)$$

(where  $K_{z,i}(z)$  is the nonuniformity coefficient at point  $z$  for the  $i$ -th FC;

$R_i(z)$  is the reaction rate at point  $z$  near the neutron flux maximum for the  $i$ -th FC;

$\bar{R}_i$  is the mean reaction rate along the  $i$ -th FC axis),

the above proposition may be presented as

$${}^0K_{z,i}^{63\text{Cu}}(z) = {}^0K_{z,i}^{235\text{U}}(z); \quad {}^1K_{z,i}^{63\text{Cu}}(z) = {}^1K_{z,i}^{235\text{U}}(z),$$

where  ${}^0,1K_{z,i}^{63\text{Cu}}(z)$  is the nonuniformity coefficient at point  $z$  obtained for the  $i$ -th FC via the  $^{63}\text{Cu}(n,\gamma)$  reaction rate;  ${}^0,1K_{z,i}^{235\text{U}}(z)$  is the nonuniformity coefficient at point  $z$  obtained for the  $i$ -th FC via the  $^{235}\text{U}(n,f)$  reaction rate.

The superscripts "0" and "1" indicate the orientation of an experimental sample placed on FC. The maximum and minimum of the neutron field distribution along the FC azimuth are located on the line that connects the FC center and the core center. The superscript "0" indicates that the experimental sample is at the least distance from the core center, while the superscript "1" indicates the greatest distance (see Table 17 for exceptions). In his case, the mean reaction rate in centerline direction is calculated for the  $i$ -th FC as

$$\bar{R}_i = \frac{\int_a^b R_i(z) dz}{\int_a^b dz} = \frac{\int_a^b R_i(z) dz}{b-a}, \quad (27)$$

where  $a$  and  $b$  are the fuel location boundaries in the FC (see Subsection 1.13 below;  $a=15$  mm,  $b=1283$  mm).

Considering that, generally, the centerline distribution of neutron flux in the MAKET core is described as  $A_i^{0,1} \cdot \cos(B_i^{0,1} \cdot (z - C_i^{0,1}))$ , the integral in (27) was calculated by two methods, depending on the FC position:

- in the case of the SBM-surrounding FCs with the strongest disturbance of the neutron flux (34-16 "1", 32-16 "1", 31-17 "1", 30-18 "1", 31-19 "1", 32-20 "1", 34-20 "1"), the integral was calculated numerically as

$$\bar{R}_i^{0,1} = \frac{\sum_{j=1}^{n_i} R_i^{0,1}(z_j) \cdot \Delta z_j}{\sum_{j=1}^n \Delta z_j}, \quad (28)$$

(where  $n_i$  is the number of the experimental samples fixed with Scotch tape to the FC)

- in the case of the remaining FCs and the FCs of position 0, where the neutron flux density is little disturbed (see Figs. 18 and 19), the experimental reaction rates were described by the above presented function, while the integral was calculated analytically as

$$\begin{aligned} \bar{R}_i^{0,1} &= \frac{1}{b-a} \cdot \int_a^b A_i^{0,1} \cdot \cos(B_i^{0,1} \cdot (z - C_i^{0,1})) \cdot dz = \\ &= \frac{1}{b-a} \cdot \frac{A_i^{0,1}}{B_i^{0,1}} \cdot [\sin(B_i^{0,1} \cdot (b - C_i^{0,1})) - \sin(B_i^{0,1} \cdot (a - C_i^{0,1}))] \end{aligned} \quad (29)$$

The parameters  $A_i^{0,1}$ ,  $B_i^{0,1}$ , and  $C_i^{0,1}$  were found by least squares method. Using the measured nonuniformity coefficient for the i-th FC,  ${}^{0,1}K_{z,i}^{63Cu}$ , together with the absolute  ${}^{235}U(n,f)$  reaction rate measured at point  $z$ ,  $R_{(n,f)_i}^{0,1}(z)$ , we can calculate the mean  ${}^{235}U(n,f)$  reaction rate,  $\bar{R}_{(n,f)_i}^{0,1}(z)$ , over the FC length without measuring the space distribution of neutron flux density over the FC length with the  ${}^{235}U$ -containing experimental samples:

$$\bar{R}_{(n,f)_i}^{0,1} = \frac{R_{(n,f)_i}^{0,1}(z)}{{}^{0,1}K_{z,i}^{AB}} \quad (30)$$

On averaging over the i-th FC volume, the  ${}^{235}U(n,f)$  reaction rate can be presented as

$$\bar{R}_{(n,f)_i}^{0,1} = \frac{1}{2} \cdot \left( \bar{R}_{(n,f)_i}^{0,1} + \bar{R}_{(n,f)_i}^{1,1} \right) \quad (31)$$

On calculating the  $\bar{R}_{(n,f)_i}^{0,1}$  value and basing on the U quantities in each of the FCs, we can determine the MAKET facility power via formula (24).

The  ${}^{235}U(n,f)$  reaction rate is determined by the formula similar to (17).

The  $^{235}\text{U}$  fission rate was determined (as in Subsection 1.9.1) by simultaneous using two fission products ( $^{143}\text{Ce}$  and  $^{97}\text{Zr}$ ), so the formulas to determine the absolute MAKET power are

$$W = E_f \cdot \left( \frac{SPA}{N} \right)_{st.}^{235U} \cdot X \quad (32)$$

$$\Delta W = W \cdot \sqrt{\left( \frac{\Delta E_f}{E_f} \right)^2 + \left( \frac{\Delta SPA_{st.}^{235U}}{SPA_{st.}^{235U}} \right)^2 + \left( \frac{\Delta N_{st.}^{235U}}{N_{st.}^{235U}} \right)^2 + \left( \frac{\Delta X}{X^{235U}} \right)^2}$$

where

$$X = \sum_i^n N_i^{TK} \cdot \frac{\bar{Y}_i}{K_i^{fuel}} \quad (33)$$

$$\Delta X = \sqrt{\sum_{i=1}^n \left( \frac{N_i^{TK} \cdot \Delta \bar{Y}_i}{K_i^{fuel}} \right)^2 + \left( \frac{\Delta N_i^{TK} \cdot \bar{Y}_i}{K_i^{fuel}} \right)^2}$$

$$\bar{Y}_i = \frac{1}{2} \cdot \left( \frac{\bar{Y}_i^{0''}}{K_{z_i}^{0''} \cdot SPA_i^{0''235U}} + \frac{\bar{Y}_i^{1''}}{K_{z_i}^{1''} \cdot SPA_i^{1''235U}} \right) \quad (34)$$

$$\Delta \bar{Y}_i = \frac{1}{2} \sqrt{\left( \frac{\bar{Y}_i^{0''}}{K_{z_i}^{0''} \cdot SPA_i^{0''235U}} \right)^2 \cdot \left[ \left( \frac{\Delta \bar{Y}_i^{0''}}{\bar{Y}_i^{0''}} \right)^2 + \left( \frac{\Delta K_{z_i}^{0''}}{K_{z_i}^{0''}} \right)^2 + \left( \frac{\Delta SPA_i^{0''235U}}{SPA_i^{0''235U}} \right)^2 \right] + \left( \frac{\bar{Y}_i^{1''}}{K_{z_i}^{1''} \cdot SPA_i^{1''235U}} \right)^2 \cdot \left[ \left( \frac{\Delta \bar{Y}_i^{1''}}{\bar{Y}_i^{1''}} \right)^2 + \left( \frac{\Delta K_{z_i}^{1''}}{K_{z_i}^{1''}} \right)^2 + \left( \frac{\Delta SPA_i^{1''235U}}{SPA_i^{1''235U}} \right)^2 \right]}$$

The  $\bar{Y}_i^{0,1''}$  value was calculated by formula (19) allowing for positions 0 and 1 for the i-th FC, i.e.,

$$\bar{Y}_i^{0,1''} = \frac{\frac{Y_i^{0,1''143Ce}}{(\Delta Y_i^{0,1''143Ce})^2} + \frac{Y_i^{0,1''97Zr}}{(\Delta Y_i^{0,1''97Zr})^2}}{\frac{1}{(\Delta Y_i^{0,1''143Ce})^2} + \frac{1}{(\Delta Y_i^{0,1''97Zr})^2}} \quad (35)$$

$$\left(\Delta\bar{Y}_i^{0,1''}\right)^2 = \frac{1}{\frac{1}{(\Delta Y_i^{0,1''^{143}\text{Ce}})^2} + \frac{1}{(\Delta Y_i^{0,1''^{97}\text{Zr}})^2}}$$

$$Y_i^{0,1''^{143}\text{Ce}} = \frac{SPA_i^{0,1''^{143}\text{Ce}}}{J^{143\text{Ce}} \cdot (\lambda \cdot \eta \cdot \varepsilon)^{143\text{Ce}} \cdot F^{143\text{Ce}}(t_2, t_3)} \quad (36)$$

$$Y_i^{0,1''^{97}\text{Zr}} = \frac{SPA_i^{0,1''^{97}\text{Zr}}}{J^{97\text{Zr}} \cdot (\lambda \cdot \eta \cdot \varepsilon)^{97\text{Zr}} \cdot F^{97\text{Zr}}(t_2, t_3)} \quad (37)$$

$$\Delta Y^{0,1''^{143}\text{Ce},^{97}\text{Zr}} = Y^{0,1''^{143}\text{Ce},^{97}\text{Zr}} \cdot \sqrt{\left[\left(\frac{\Delta SPA}{SPA}\right)^2 + \left(\frac{\Delta J}{J}\right)^2 + \left(\frac{\Delta \lambda}{\lambda}\right)^2 + \left(\frac{\Delta \eta}{\eta}\right)^2 + \left(\frac{\Delta \varepsilon}{\varepsilon}\right)^2\right]^{143\text{Ce},^{97}\text{Zr}}}$$

It can readily be seen that, when used to determine the fission reaction rate for but a single fragment nuclide, formulas (32)-(37) get much simplified, though retaining the general physical meaning. Considering the symmetry of the examined lattices, but a half of the FCs were used in the experiments to determine the energy deposit, i.e., 19 FCs were used.

In the case of lattice 21-1-5(M2), the FCs were used in cells: 34-14\*, 31-15, 33-15, 30-16, 32-16, 34-16\*, 29-17, 31-17, 24-18, 28-18, 30-18, 29-19, 31-19, 30-20, 32-20, 34-20\*, 31-21, 33-21, 34-22\*.

In the case of lattice 21-2, the FCs were used in cells: 34-14\*, 31-15, 33-15, 30-16, 32-16, 34-16\*, 29-17, 31-17, 34-18\*, 28-18, 30-18, 29-19, 31-19, 30-20, 32-20, 34-20\*, 31-21, 33-21, 34-22\*.

The asterisk (\*) indicates the channels on the lattice symmetry axis, i.e., with symmetry coefficient  $K^{sim} = 1$ . The rest channels have  $K^{sim} = 2$  (see Tables 16 and 17).

The 6.3-mm diameter, ~300- $\mu\text{m}$  thick  $^{nat}\text{Cu}$  foil samples were used in the experiments to measure the reaction rates along the FC. The samples were fixed with Scotch tape at two opposite points of heights of 94, 253, 411, 570, 729, 887, 1045, and 1204 mm from the top of the bottom lattice on the outside of the FCs taken from the MAKET core. Besides, the samples in lattice 21-1-5(M2) were also fixed at height of 15 mm and 1283 mm. The samples having been fixed, the FCs were placed in the core after being oriented to positions 0 and 1 (see above), except for FC 34-18 in lattice 21-2, on which four experimental samples were fixed (the superscripts "0", "1", "2", and "3" corresponded to positioning the samples at the points nearest to FC 34-16, FC 38-18, FC 34-20, and FC 30-18, respectively). The measurement results are presented in Figs. 18 and 19 and in Tables 18 and 19.

Also, ten  $^{nat}\text{Cu}$  foil samples of 6.3-mm diameter, ~300- $\mu\text{m}$  thickness each were placed in all gaps between the small multi-salt rods in all the containers (four containers for lattice 21-1-5(M2) and three containers for lattice 21-2) with the view to obtain the spatial distribution of neutrons inside the SBM. Fig. 20 and Tables 20 and 21 present the results.

The absolute  $^{235}\text{U}(n,f)$  reaction rates were measured using high-enriched U foil samples ( $\sim 90\%$   $^{235}\text{U}$ ) of 6.3-mm diameter, 100- $\mu\text{m}$  thickness each. Those U samples were scotch-taped right to the Cu samples at a 570-mm height.

In the case of FC 32-16, in both lattices, two  $^{235}\text{U}$  samples were also scotch-taped right on the outside of the fuel element at a 570-mm height to verify the calculated correction factor  $K^{fuel}$ , which allows for the difference between the fission reaction rate on the FC surface and the reaction rate averaged over the fuel volume. Table 14 presents the results of comparing between the experimental and calculated fission reaction rates.

Table 14. Comparison between the experimental and calculated  $K^{fuel}$  values.

The ratio of the $^{235}\text{U}$ fission rates on the surfaces of FC and of fuel element			
21-1-5(M2)		21-2	
Experiment	1.083 $\pm$ 0.005	Experiment	1.105 $\pm$ 0.016
Calculation	1.092	Calculation	1.104

Tables 18 and 19, together with Figs. 18 and 19, present the measured FC height distributions of the  $^{63}\text{Cu}(n,\gamma)$  reaction rates for lattices 21-1-5(M2) and 21-2. Tables 16 and 17 present the nonuniformity coefficients  $K_z$  obtained basing on the distributions. Tables 16 and 17 presents the calculated values of cofactor X entering formula (32) to calculate the MAKET facility power for lattices 21-1-5(M2) and 21-2. Table 15 presents the final results of calculating the power obtained making allowance for the parameters of the standard used (see formula (4)).

Table 15. Power (W) in lattices 21-1-5(M2) and 21-2.

	21-1-5(M2)		21-2	
	W $\pm$ $\Delta$ W	%	W $\pm$ $\Delta$ W	%
$W_0$	81.4 $\pm$ 1.7	2.1	78.8 $\pm$ 1.6	2.0

The tabulated power values were taken to be the base values. Determination of the relative neutron flux density by the reactometer has made it possible to calculate the values of the MAKET power during all experiments:

$$W_i = W_0 \cdot \frac{\varphi_i}{\varphi_0},$$

where  $W_i$  is the MAKET power during the i-th experiment;

$W_0$  is the basic power value;

$\varphi_i$  is the mean relative neutron flux density during the i-th experiment;

$\varphi_0$  is the mean relative neutron flux density during the basic experiment.

21-1-5(M2)

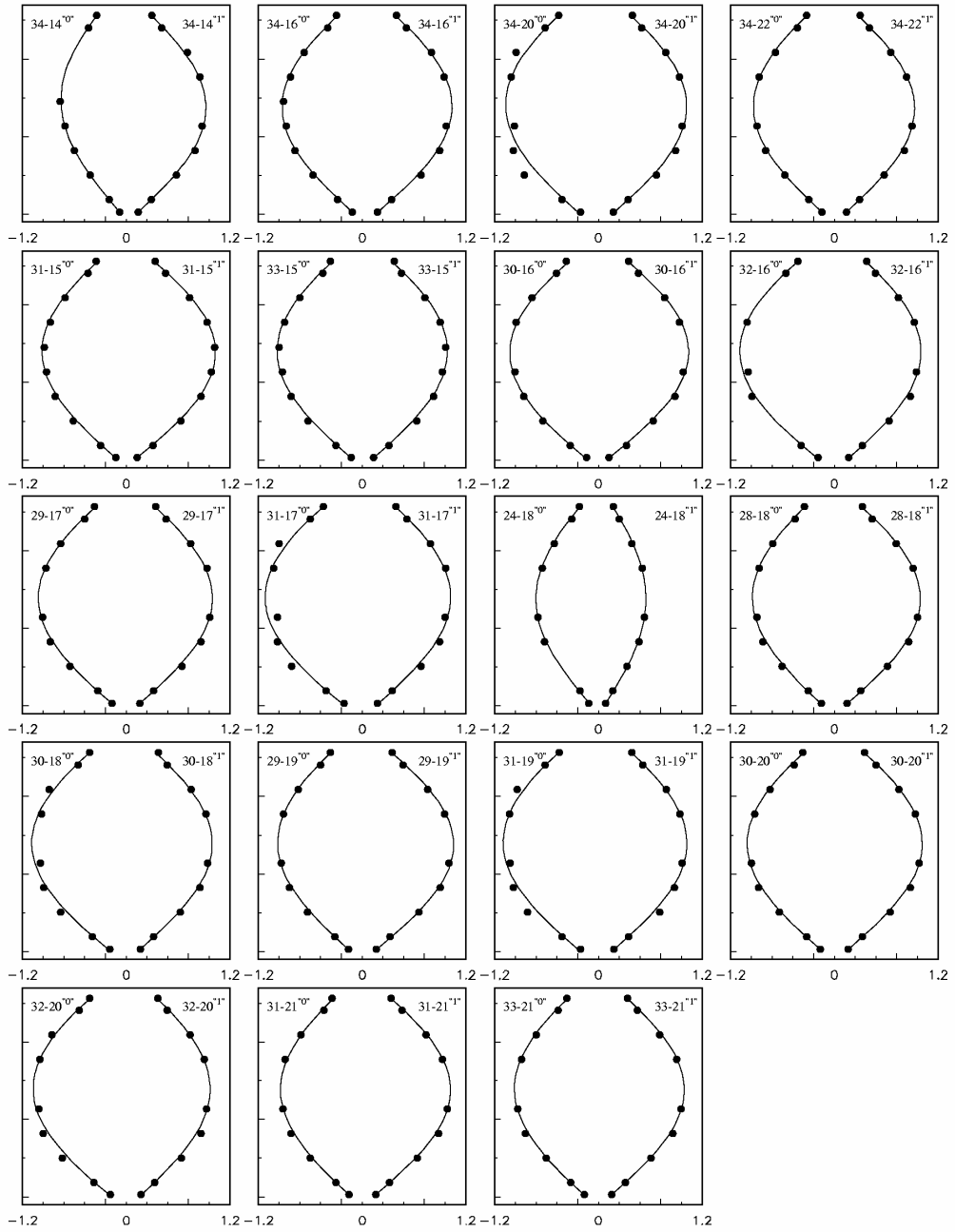


Fig. 18. The FC height distributions of the  ${}^{63}\text{Cu}$  ( $n,\gamma$ ) reaction rates for lattice 21-1-5(M2).

21-2

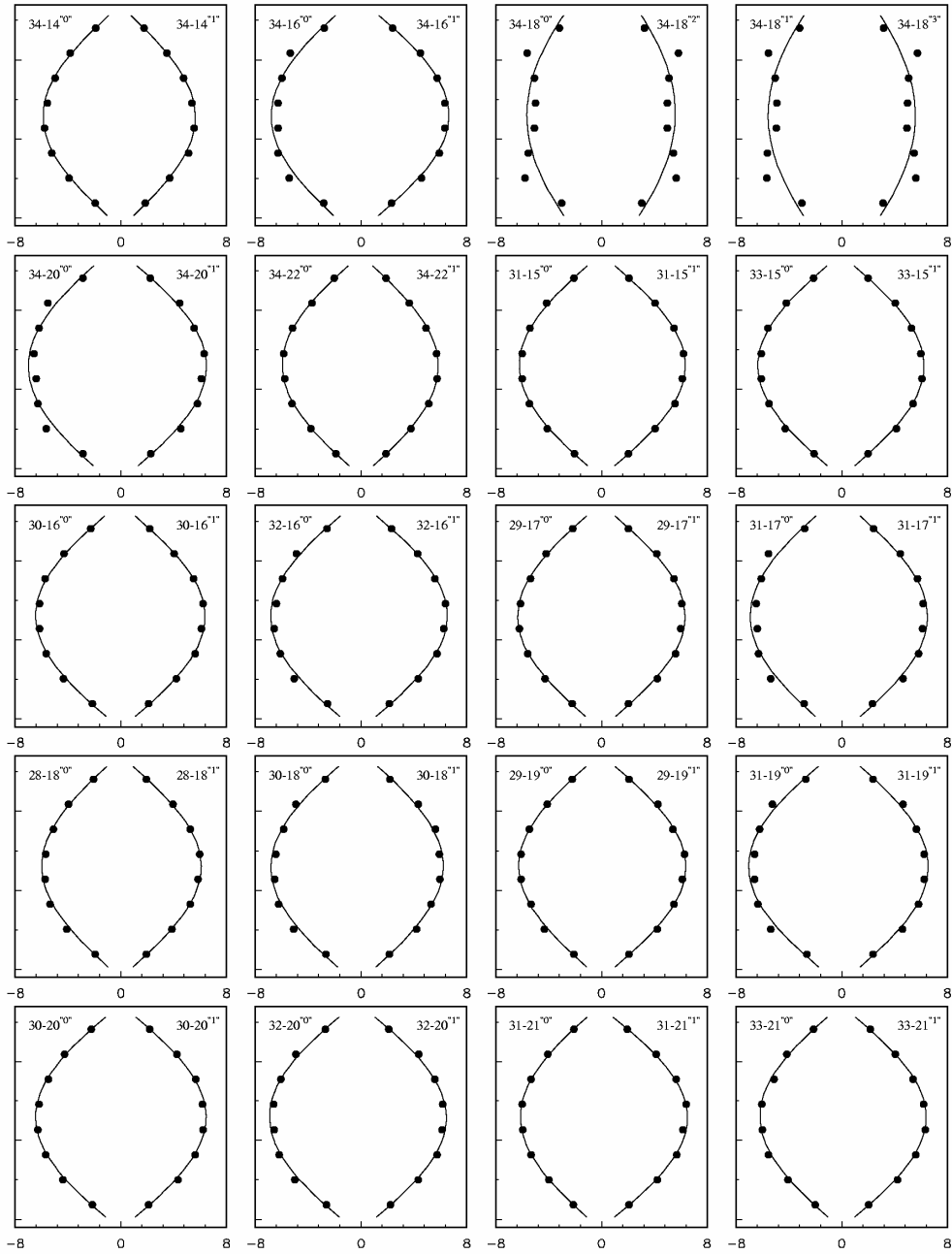


Fig. 19. The FC height distributions of the  $^{63}\text{Cu}$  ( $n,\gamma$ ) reaction rates for lattice 21-2.

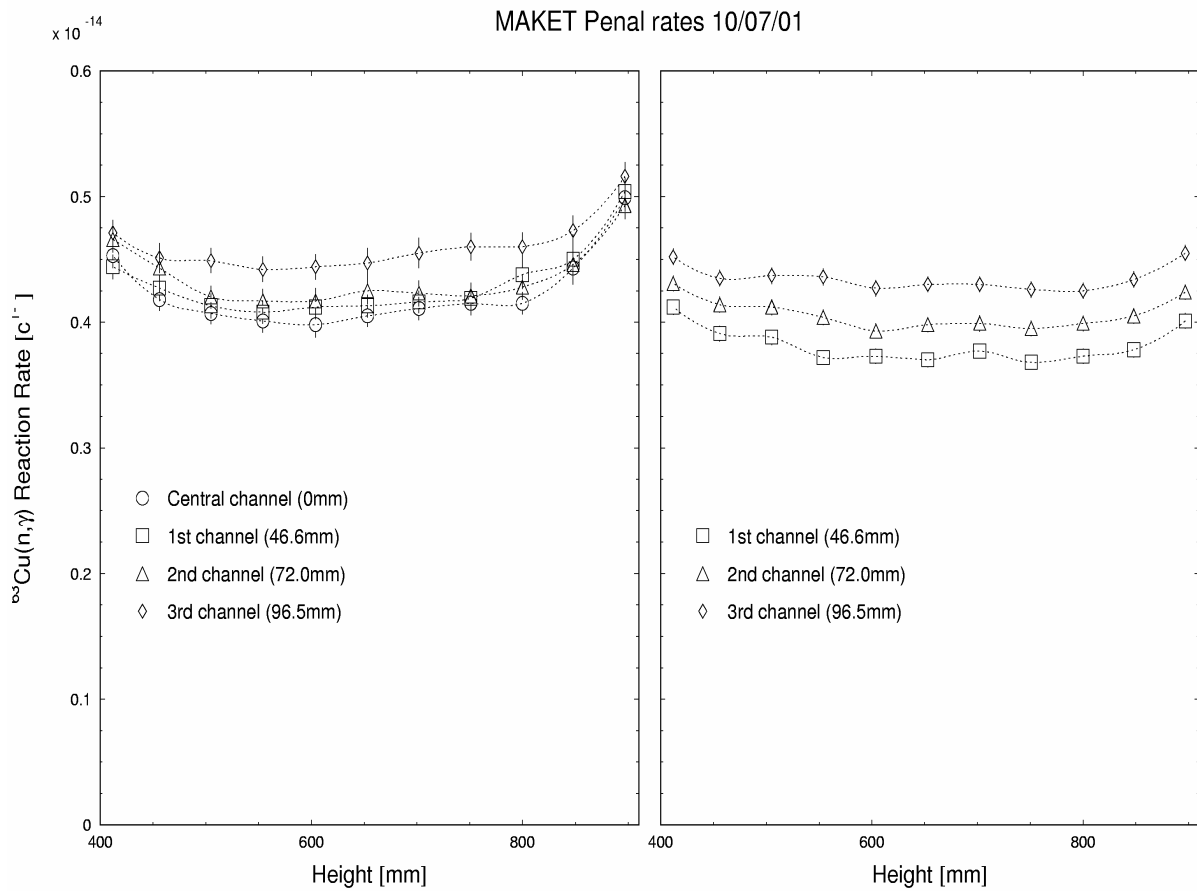


Fig. 20. Distributions of the  $^{63}\text{Cu}(n,\gamma)$  reaction rates in the containers.



Table 16. The steps of calculating cofactor X in lattice 21-1-5(M2).

FC	Position	$S_i^{235U} \pm \Delta S_i^{235U}$	$S_i^{143Ce} \pm \Delta S_i^{143Ce}$	$S_i^{97Zr} \pm \Delta S_i^{97Zr}$	$K_{Z_i} \pm \Delta K_{Z_i}$	$K_i^{fuel}$	$K^{sim}$	$Y^{143Ce} \pm \Delta Y^{143Ce}, \times 10^6$	$Y^{97Zr} \pm \Delta Y^{97Zr}, \times 10^6$	$\bar{Y} \pm \Delta \bar{Y}, \times 10^6$	$\bar{\bar{Y}} \pm \Delta \bar{\bar{Y}}, \times 10^4$	$X_i, \times 10^{28}$
34-14	0	9.594±0.074	26.32±0.42	47.05±0.36	1.311±0.033	1.165	1	1.226±0.034	1.255±0.031	1.241±0.023	9.93±0.20	2.011
	1	8.849±0.070	24.81±0.30	43.91±0.35	1.317±0.021			1.155±0.030	1.171±0.027	1.164±0.020		
34-16	0	9.488±0.072	28.27±0.30	49.93±0.48	1.189±0.013	1.154	1	1.316±0.033	1.331±0.029	1.325±0.022	11.45±0.20	2.331
	1	9.375±0.081	28.04±0.25	50.24±0.48	1.266±0.025			1.306±0.032	1.340±0.029	1.325±0.021		
34-20	0	8.902±0.132	26.66±0.30	47.46±0.66	1.183±0.008	1.154	1	1.241±0.032	1.265±0.028	1.255±0.021	11.30±0.21	2.312
	1	9.753±0.073	29.22±0.47	51.87±0.88	1.316±0.026			1.361±0.038	1.383±0.035	1.373±0.026		
34-22	0	8.839±0.097	24.47±0.34	44.16±1.11	1.312±0.015	1.163	1	1.139±0.031	1.177±0.028	1.160±0.021	9.91±0.19	2.012
	1	8.878±0.099	24.67±0.74	44.68±0.57	1.344±0.016			1.149±0.043	1.191±0.043	1.170±0.030		
31-15	0	9.546±0.072	26.90±0.34	48.56±0.37	1.281±0.044	1.164	2	1.253±0.033	1.295±0.030	1.276±0.022	10.49±0.25	2.097
	1	8.950±0.113	26.85±0.23	47.78±0.37	1.339±0.026			1.250±0.031	1.274±0.027	1.264±0.020		
33-15	0	9.051±0.112	25.97±0.49	46.96±0.44	1.266±0.030	1.157	2	1.209±0.036	1.252±0.034	1.232±0.025	10.39±0.22	2.121
	1	9.382±0.080	26.87±0.39	47.30±0.45	1.336±0.020			1.251±0.034	1.261±0.031	1.257±0.023		
30-16	0	9.404±0.072	27.43±0.31	49.97±0.46	1.292±0.015	1.162	2	1.277±0.033	1.332±0.030	1.307±0.027	10.85±0.23	2.220
	1	9.280±0.073	27.93±0.65	50.39±0.47	1.303±0.030			1.301±0.043	1.343±0.041	1.323±0.030		
32-16	0	9.321±0.131	29.81±0.25	52.38±0.49	1.295±0.010	1.153	2	1.388±0.034	1.397±0.030	1.393±0.022	11.17±0.21	2.275
	1	8.282±0.069	24.40±0.29	43.60±0.61	1.287±0.030			1.136±0.029	1.162±0.026	1.151±0.020		
29-17	0	8.743±0.090	26.37±0.28	46.67±0.52	1.297±0.024	1.160	2	1.228±0.031	1.244±0.028	1.237±0.021	10.72±0.20	2.178
	1	9.370±0.073	27.43±0.27	49.87±0.49	1.323±0.021			1.277±0.032	1.330±0.029	1.306±0.026		
31-17	0	9.298±0.100	28.32±0.25	50.49±0.50	1.195±0.011	1.153	2	1.319±0.033	1.346±0.029	1.334±0.022	11.59±0.19	2.380
	1	8.562±0.086	25.61±0.35	45.97±0.56	1.266±0.019			1.192±0.032	1.226±0.029	1.211±0.022		
24-18	0	7.534±0.064	17.06±0.24	29.43±0.36	1.341±0.025	1.174	2	0.794±0.021	0.785±0.019	0.789±0.014	6.84±0.13	1.384
	1	9.188±0.071	15.34±0.22	27.15±0.57	1.334±0.018			0.714±0.019	0.724±0.017	0.720±0.013		
28-18	0	8.911±0.070	25.22±0.32	44.66±0.78	1.286±0.021	1.163	2	1.174±0.031	1.191±0.028	1.184±0.021	10.59±0.20	2.165
	1	8.382±0.089	25.71±0.44	45.81±0.48	1.330±0.024			1.197±0.035	1.221±0.032	1.210±0.023		
30-18	0	8.636±0.128	25.97±0.41	46.37±0.49	1.257±0.013	1.155	2	1.209±0.034	1.236±0.031	1.224±0.023	10.93±0.21	2.226
	1	8.710±0.133	25.55±0.28	44.48±0.48	1.289±0.023			1.190±0.030	1.186±0.027	1.188±0.020		
29-19	0	8.751±0.071	25.64±0.28	45.01±0.49	1.294±0.015	1.162	2	1.194±0.031	1.200±0.027	1.197±0.020	10.91±0.20	2.232
	1	8.968±0.102	27.61±0.39	50.29±0.52	1.304±0.021			1.286±0.035	1.341±0.032	1.315±0.028		
31-19	0	9.195±0.075	29.11±0.31	50.76±0.53	1.228±0.010	1.156	2	1.355±0.034	1.353±0.030	1.354±0.023	11.61±0.18	2.334
	1	8.573±0.107	26.19±0.30	46.39±0.51	1.278±0.016			1.219±0.031	1.237±0.028	1.229±0.021		
30-20	0	8.969±0.073	26.99±0.40	48.30±0.53	1.293±0.032	1.164	2	1.257±0.034	1.288±0.031	1.274±0.023	11.06±0.22	2.236
	1	8.766±0.071	27.74±0.37	48.39±0.53	1.324±0.020			1.292±0.034	1.290±0.030	1.291±0.023		
32-20	0	9.386±0.072	29.63±0.32	52.54±0.56	1.282±0.013	1.153	2	1.380±0.035	1.401±0.031	1.392±0.023	11.08±0.27	2.242
	1	9.587±0.094	27.02±0.62	50.93±0.58	1.289±0.029			1.258±0.041	1.358±0.041	1.308±0.050		
31-21	0	9.651±0.074	26.92±0.31	48.50±0.55	1.322±0.035	1.163	2	1.254±0.032	1.293±0.029	1.275±0.022	10.40±0.22	2.131
	1	8.871±0.108	27.27±0.32	48.16±0.92	1.332±0.026			1.270±0.033	1.284±0.029	1.278±0.022		
33-21	0	9.711±0.073	27.49±0.41	48.36±0.57	1.297±0.021	1.158	2	1.280±0.035	1.289±0.032	1.285±0.024	10.39±0.20	2.117
	1	8.915±0.070	26.59±0.31	47.15±0.57	1.324±0.027			1.238±0.032	1.257±0.029	1.249±0.021		
$\Sigma =$											73.34±0.30	

Table 17. The steps of calculating cofactor X in lattice 21-2.

FC	Position	$S_i^{235U} \pm \Delta S_i^{235U}$	$S_i^{143Ce} \pm \Delta S_i^{143Ce}$	$S_i^{97Zr} \pm \Delta S_i^{97Zr}$	$K_{Z_i} \pm \Delta K_{Z_i}$	$K_i^{fuel}$	$K^{sim}$	$Y^{143Ce} \pm \Delta Y^{143Ce}, \times 10^6$	$Y^{97Zr} \pm \Delta Y^{97Zr}, \times 10^6$	$\bar{Y} \pm \Delta \bar{Y}, \times 10^6$	$\bar{Y} \pm \Delta \bar{Y}, \times 10^4$	$X_i \times 10^{28}$
34-14	0	8.776±0.069	12.23±0.18	23.33±0.30	1.398±0.022	1.167	1	1.126±0.030	1.217±0.024	1.181±0.045	9.55±0.23	1.931
	1	9.779±0.110	14.11±0.19	25.25±0.31	1.413±0.020			1.298±0.034	1.317±0.025	1.310±0.020		
34-16	0	9.368±0.121	14.44±0.20	26.92±0.36	1.353±0.013	1.151	1	1.329±0.035	1.404±0.027	1.376±0.037	11.16±0.25	2.278
	1	8.708±0.083	14.11±0.21	26.10±0.36	1.338±0.025			1.299±0.034	1.362±0.027	1.337±0.031		
34-18	0	9.514±0.105	11.62±0.20	21.38±0.37	1.208±0.014	1.101	1	1.070±0.030	1.116±0.024	1.097±0.023	9.50±0.12	2.013
	1	9.472±0.085	11.27±0.19	20.49±0.36	1.184±0.014			1.037±0.029	1.069±0.023	1.056±0.018		
	2	9.237±0.104	11.26±0.19	19.93±0.36	1.193±0.015			1.037±0.029	1.040±0.022	1.039±0.018		
	3	9.103±0.149	11.01±0.19	20.09±0.37	1.181±0.014			1.014±0.028	1.048±0.023	1.035±0.018		
34-20	0	9.656±0.077	15.64±0.24	27.60±0.47	1.343±0.020	1.154	1	1.440±0.038	1.440±0.029	1.440±0.023	11.07±0.26	2.266
	1	10.210±0.075	15.53±0.25	29.19±0.49	1.318±0.032			1.429±0.039	1.523±0.032	1.485±0.046		
34-22	0	9.062±0.059	12.92±0.24	24.25±0.48	1.385±0.024	1.168	1	1.189±0.035	1.265±0.029	1.233±0.038	9.64±0.23	1.950
	1	9.349±0.125	13.21±0.23	24.52±0.49	1.417±0.023			1.216±0.034	1.279±0.028	1.253±0.031		
31-15	0	8.981±0.070	14.04±0.19	24.76±0.31	1.368±0.019	1.168	2	1.293±0.033	1.291±0.024	1.292±0.020	10.51±0.16	2.094
	1	8.589±0.069	13.30±0.18	24.05±0.31	1.379±0.015			1.224±0.032	1.254±0.024	1.243±0.019		
33-15	0	9.395±0.074	14.04±0.19	25.70±0.32	1.361±0.021	1.156	2	1.292±0.033	1.340±0.026	1.323±0.023	10.23±0.17	2.089
	1	9.155±0.071	14.18±0.21	24.83±0.32	1.403±0.021			1.305±0.035	1.295±0.026	1.299±0.021		
30-16	0	8.834±0.073	13.98±0.19	25.35±0.33	1.351±0.022	1.162	2	1.286±0.033	1.322±0.025	1.309±0.020	10.82±0.20	2.212
	1	8.928±0.078	13.66±0.19	25.36±0.33	1.363±0.017			1.257±0.033	1.323±0.026	1.298±0.032		
32-16	0	9.399±0.094	15.38±0.20	28.41±0.36	1.449±0.013	1.158	2	1.415±0.036	1.482±0.028	1.457±0.032	10.65±0.18	2.161
	1	9.320±0.072	14.63±0.21	25.72±0.34	1.360±0.018			1.347±0.035	1.342±0.026	1.343±0.021		
29-17	0	9.085±0.071	14.07±0.21	25.69±0.36	1.386±0.019	1.162	2	1.295±0.034	1.340±0.027	1.323±0.022	10.61±0.20	2.152
	1	9.039±0.074	13.81±0.20	25.53±0.37	1.352±0.025			1.271±0.033	1.332±0.026	1.309±0.030		
31-17	0	8.781±0.072	14.08±0.20	25.80±0.37	1.361±0.013	1.159	2	1.296±0.034	1.346±0.026	1.327±0.024	11.21±0.27	2.289
	1	9.175±0.167	14.19±0.17	26.69±0.38	1.311±0.029			1.306±0.033	1.393±0.025	1.360±0.042		
28-18	0	9.557±0.072	14.02±0.21	25.32±0.38	1.361±0.027	1.166	2	1.290±0.034	1.321±0.026	1.310±0.021	10.20±0.17	2.081
	1	9.350±0.072	14.20±0.21	25.79±0.39	1.376±0.017			1.307±0.035	1.345±0.027	1.331±0.021		
30-18	0	9.011±0.086	14.83±0.21	26.30±0.39	1.435±0.015	1.162	2	1.365±0.036	1.372±0.027	1.369±0.021	10.71±0.19	2.168
	1	9.452±0.133	14.88±0.21	26.54±0.40	1.348±0.027			1.369±0.036	1.384±0.027	1.379±0.022		
29-19	0	9.339±0.076	14.18±0.21	25.22±0.42	1.375±0.024	1.151	2	1.305±0.035	1.316±0.027	1.312±0.021	10.62±0.19	2.195
	1	8.733±0.069	14.06±0.22	25.57±0.42	1.369±0.023			1.294±0.035	1.334±0.027	1.318±0.021		
31-19	0	8.824±0.072	14.54±0.22	27.01±0.44	1.401±0.016	1.153	2	1.338±0.036	1.409±0.029	1.381±0.034	11.18±0.24	2.255
	1	9.344±0.071	14.70±0.22	27.03±0.44	1.328±0.031			1.353±0.036	1.410±0.029	1.388±0.028		
30-20	0	9.552±0.072	15.05±0.23	27.21±0.45	1.382±0.024	1.153	2	1.385±0.037	1.420±0.029	1.407±0.023	10.85±0.22	2.216
	1	9.353±0.071	14.87±0.23	27.66±0.46	1.368±0.025			1.369±0.037	1.443±0.029	1.414±0.036		
32-20	0	10.232±0.075	17.39±0.24	30.48±0.49	1.431±0.020	1.155	2	1.600±0.042	1.590±0.031	1.594±0.025	10.73±0.23	2.168
	1	9.646±0.100	14.45±0.24	26.98±0.46	1.350±0.028			1.330±0.036	1.408±0.030	1.376±0.038		
31-21	0	9.498±0.173	13.88±0.22	25.43±0.46	1.378±0.021	1.166	2	1.277±0.035	1.327±0.028	1.307±0.024	10.32±0.24	2.108
	1	9.070±0.025	13.79±0.17	25.84±0.36	1.364±0.025			1.269±0.032	1.348±0.025	1.318±0.038		
33-21	0	9.094±0.071	13.73±0.23	25.43±0.48	1.373±0.029	1.160	2	1.264±0.035	1.327±0.028	1.302±0.031	10.17±0.22	2.068
	1	9.809±0.163	14.87±0.24	26.46±0.49	1.413±0.025			1.369±0.037	1.380±0.029	1.376±0.023		
											Σ =	70.95±0.30

Table 18. The  $^{63}\text{Cu}$  reaction rates in lattice 21-1-5(M2).

L, m	$(R \pm \Delta R) \times 10^{-15} / (\text{SPA} \pm \Delta \text{SPA})$			
	Channel			
	24-18 "0"	24-18 "1"	28-18 "0"A	28-18 "1"
1.283	$0.958 \pm 0.007 / 0.935 \pm 0.005$	$0.764 \pm 0.006 / 0.746 \pm 0.004$	$1.526 \pm 0.011 / 1.490 \pm 0.007$	$1.452 \pm 0.011 / 1.418 \pm 0.007$
1.204	$1.319 \pm 0.010 / 1.288 \pm 0.007$	$1.054 \pm 0.008 / 1.029 \pm 0.006$	$1.919 \pm 0.014 / 1.874 \pm 0.009$	$1.877 \pm 0.014 / 1.833 \pm 0.009$
1.045	$2.213 \pm 0.029 / 2.161 \pm 0.026$	$1.644 \pm 0.022 / 1.605 \pm 0.020$	$3.044 \pm 0.040 / 2.973 \pm 0.035$	$3.016 \pm 0.040 / 2.945 \pm 0.036$
0.887	$2.783 \pm 0.021 / 2.718 \pm 0.013$	$2.193 \pm 0.017 / 2.142 \pm 0.011$	$3.770 \pm 0.028 / 3.681 \pm 0.018$	$3.915 \pm 0.029 / 3.823 \pm 0.019$
0.570	$3.034 \pm 0.022 / 2.963 \pm 0.013$	$2.322 \pm 0.017 / 2.267 \pm 0.010$	$3.992 \pm 0.028 / 3.898 \pm 0.017$	$4.205 \pm 0.030 / 4.107 \pm 0.018$
0.411	$2.655 \pm 0.020 / 2.593 \pm 0.012$	$2.015 \pm 0.015 / 1.968 \pm 0.010$	$3.548 \pm 0.026 / 3.465 \pm 0.016$	$3.620 \pm 0.027 / 3.535 \pm 0.016$
0.253		$1.407 \pm 0.019 / 1.374 \pm 0.017$	$2.521 \pm 0.034 / 2.462 \pm 0.030$	$2.636 \pm 0.035 / 2.574 \pm 0.031$
0.094	$0.927 \pm 0.007 / 0.905 \pm 0.005$	$0.725 \pm 0.006 / 0.708 \pm 0.004$	$1.311 \pm 0.010 / 1.281 \pm 0.007$	$1.329 \pm 0.010 / 1.298 \pm 0.007$
0.015	$0.406 \pm 0.004 / 0.397 \pm 0.003$	$0.334 \pm 0.003 / 0.326 \pm 0.003$	$0.560 \pm 0.005 / 0.547 \pm 0.004$	$0.547 \pm 0.005 / 0.534 \pm 0.004$
L, m	Channel			
	29-17 "0"	29-17 "1"	29-19 "0"A	29-19 "1"
	1.283	$1.595 \pm 0.012 / 1.557 \pm 0.007$	$1.496 \pm 0.011 / 1.461 \pm 0.007$	$1.613 \pm 0.012 / 1.575 \pm 0.008$
1.204	$2.063 \pm 0.015 / 2.015 \pm 0.010$	$1.978 \pm 0.015 / 1.931 \pm 0.009$	$2.045 \pm 0.015 / 1.997 \pm 0.010$	$2.021 \pm 0.015 / 1.974 \pm 0.010$
1.045	$3.203 \pm 0.042 / 3.128 \pm 0.037$	$3.190 \pm 0.042 / 3.115 \pm 0.037$	$3.098 \pm 0.041 / 3.025 \pm 0.037$	$3.184 \pm 0.043 / 3.110 \pm 0.038$
0.887	$3.942 \pm 0.029 / 3.850 \pm 0.018$	$4.026 \pm 0.030 / 3.932 \pm 0.019$	$3.872 \pm 0.029 / 3.781 \pm 0.018$	$4.039 \pm 0.030 / 3.944 \pm 0.019$
0.570	$4.124 \pm 0.029 / 4.028 \pm 0.017$	$4.200 \pm 0.030 / 4.102 \pm 0.017$	$4.086 \pm 0.029 / 3.990 \pm 0.017$	$4.423 \pm 0.031 / 4.320 \pm 0.019$
0.411	$3.761 \pm 0.027 / 3.673 \pm 0.017$	$3.667 \pm 0.027 / 3.581 \pm 0.016$	$3.579 \pm 0.026 / 3.495 \pm 0.016$	$3.929 \pm 0.029 / 3.836 \pm 0.018$
0.253	$2.764 \pm 0.036 / 2.699 \pm 0.032$	$2.783 \pm 0.037 / 2.718 \pm 0.032$	$2.650 \pm 0.036 / 2.588 \pm 0.032$	$2.780 \pm 0.037 / 2.715 \pm 0.033$
0.094	$1.407 \pm 0.011 / 1.374 \pm 0.007$	$1.370 \pm 0.011 / 1.338 \pm 0.007$	$1.366 \pm 0.011 / 1.334 \pm 0.007$	$1.385 \pm 0.011 / 1.352 \pm 0.007$
0.015	$0.586 \pm 0.005 / 0.572 \pm 0.004$	$0.568 \pm 0.005 / 0.555 \pm 0.004$	$0.597 \pm 0.006 / 0.583 \pm 0.004$	$0.600 \pm 0.006 / 0.585 \pm 0.004$
L, m	Channel			
	30-16 "0"A	30-16 "1"	30-18 "0"	30-18 "1"
	1.283	$1.622 \pm 0.012 / 1.584 \pm 0.008$	$1.518 \pm 0.012 / 1.483 \pm 0.008$	$1.859 \pm 0.014 / 1.815 \pm 0.008$
1.204	$2.103 \pm 0.016 / 2.054 \pm 0.011$	$2.022 \pm 0.016 / 1.974 \pm 0.010$	$2.397 \pm 0.018 / 2.341 \pm 0.011$	$2.047 \pm 0.015 / 1.999 \pm 0.010$
1.045	$3.297 \pm 0.043 / 3.220 \pm 0.038$	$3.250 \pm 0.043 / 3.174 \pm 0.038$	$3.858 \pm 0.051 / 3.768 \pm 0.045$	$3.153 \pm 0.042 / 3.079 \pm 0.037$
0.887	$4.078 \pm 0.031 / 3.982 \pm 0.020$	$4.036 \pm 0.031 / 3.941 \pm 0.020$	$4.178 \pm 0.031 / 4.080 \pm 0.020$	$3.886 \pm 0.029 / 3.795 \pm 0.018$
0.570	$4.213 \pm 0.030 / 4.114 \pm 0.018$	$4.346 \pm 0.031 / 4.244 \pm 0.019$	$4.344 \pm 0.031 / 4.242 \pm 0.018$	$4.096 \pm 0.029 / 4.000 \pm 0.017$
0.411	$3.727 \pm 0.028 / 3.640 \pm 0.018$	$3.747 \pm 0.028 / 3.659 \pm 0.018$	$4.092 \pm 0.030 / 3.996 \pm 0.018$	$3.617 \pm 0.027 / 3.532 \pm 0.016$
0.253	$2.712 \pm 0.036 / 2.648 \pm 0.032$	$2.707 \pm 0.036 / 2.644 \pm 0.032$	$2.351 \pm 0.031 / 2.296 \pm 0.028$	$2.654 \pm 0.036 / 2.592 \pm 0.032$
0.094	$1.392 \pm 0.011 / 1.360 \pm 0.008$	$1.385 \pm 0.011 / 1.353 \pm 0.008$	$1.668 \pm 0.013 / 1.629 \pm 0.008$	$1.383 \pm 0.011 / 1.350 \pm 0.007$
0.015	$0.589 \pm 0.006 / 0.575 \pm 0.004$	$0.596 \pm 0.006 / 0.582 \pm 0.004$	$0.695 \pm 0.006 / 0.679 \pm 0.005$	$0.591 \pm 0.005 / 0.577 \pm 0.004$

Table 18, cont'd.

L, m	$(R \pm \Delta R) \times 10^{-15} / (SPA \pm \Delta SPA)$			
	Channel			
	30-20 "0"	30-20 "1"	31-15 "1"	31-15 "1"
1.283	$1.617 \pm 0.012 / 1.579 \pm 0.008$	$1.529 \pm 0.012 / 1.493 \pm 0.008$	$1.539 \pm 0.012 / 1.503 \pm 0.008$	$1.441 \pm 0.011 / 1.407 \pm 0.007$
1.204	$1.984 \pm 0.015 / 1.938 \pm 0.010$	$2.048 \pm 0.016 / 2.000 \pm 0.010$	$1.971 \pm 0.015 / 1.924 \pm 0.010$	$1.952 \pm 0.015 / 1.906 \pm 0.009$
1.045	$3.194 \pm 0.043 / 3.119 \pm 0.038$	$3.131 \pm 0.041 / 3.058 \pm 0.037$	$3.308 \pm 0.026 / 3.230 \pm 0.018$	$3.450 \pm 0.046 / 3.369 \pm 0.040$
0.887	$3.896 \pm 0.029 / 3.804 \pm 0.019$	$4.066 \pm 0.031 / 3.971 \pm 0.020$	$3.798 \pm 0.029 / 3.709 \pm 0.018$	$3.992 \pm 0.030 / 3.898 \pm 0.019$
0.570	$4.123 \pm 0.030 / 4.027 \pm 0.018$	$4.222 \pm 0.030 / 4.123 \pm 0.018$	$4.057 \pm 0.029 / 3.962 \pm 0.018$	$4.207 \pm 0.030 / 4.108 \pm 0.018$
0.411	$3.712 \pm 0.027 / 3.625 \pm 0.017$	$3.717 \pm 0.028 / 3.630 \pm 0.017$	$3.690 \pm 0.027 / 3.603 \pm 0.017$	$3.719 \pm 0.027 / 3.632 \pm 0.016$
0.253	$2.681 \pm 0.036 / 2.618 \pm 0.031$	$2.712 \pm 0.037 / 2.648 \pm 0.032$	$2.815 \pm 0.037 / 2.749 \pm 0.033$	$2.984 \pm 0.040 / 2.915 \pm 0.035$
0.094	$1.432 \pm 0.011 / 1.398 \pm 0.008$	$1.392 \pm 0.011 / 1.359 \pm 0.008$	$1.340 \pm 0.011 / 1.308 \pm 0.007$	$1.362 \pm 0.011 / 1.330 \pm 0.007$
0.015	$0.602 \pm 0.006 / 0.588 \pm 0.004$	$0.596 \pm 0.006 / 0.582 \pm 0.004$	$0.554 \pm 0.005 / 0.541 \pm 0.004$	$0.560 \pm 0.005 / 0.547 \pm 0.004$
L, m	Channel			
	31-17 "0"	31-17 "1"	31-19 "0"	31-19 "1"
1.283	$2.003 \pm 0.015 / 1.956 \pm 0.009$	$1.724 \pm 0.013 / 1.684 \pm 0.008$	$1.998 \pm 0.015 / 1.951 \pm 0.009$	$1.705 \pm 0.013 / 1.665 \pm 0.008$
1.204	$2.580 \pm 0.019 / 2.520 \pm 0.012$	$2.235 \pm 0.017 / 2.183 \pm 0.011$	$2.620 \pm 0.020 / 2.559 \pm 0.013$	$2.259 \pm 0.017 / 2.206 \pm 0.011$
1.045	$4.069 \pm 0.054 / 3.973 \pm 0.047$	$3.349 \pm 0.022 / 3.271 \pm 0.011$	$4.030 \pm 0.054 / 3.936 \pm 0.048$	$3.347 \pm 0.045 / 3.269 \pm 0.040$
0.887	$4.382 \pm 0.033 / 4.280 \pm 0.020$	$4.039 \pm 0.031 / 3.945 \pm 0.020$	$4.421 \pm 0.033 / 4.318 \pm 0.021$	$4.040 \pm 0.030 / 3.946 \pm 0.019$
0.570	$4.287 \pm 0.030 / 4.187 \pm 0.018$	$4.142 \pm 0.029 / 4.045 \pm 0.017$	$4.389 \pm 0.031 / 4.286 \pm 0.019$	$4.236 \pm 0.030 / 4.137 \pm 0.018$
0.411	$4.203 \pm 0.031 / 4.105 \pm 0.019$	$3.816 \pm 0.028 / 3.726 \pm 0.017$	$4.296 \pm 0.032 / 4.195 \pm 0.020$	$3.810 \pm 0.028 / 3.721 \pm 0.018$

0.253	$3.491 \pm 0.046 / 3.409 \pm 0.041$	$2.868 \pm 0.039 / 2.801 \pm 0.034$	$3.484 \pm 0.047 / 3.402 \pm 0.041$	$3.041 \pm 0.041 / 2.970 \pm 0.036$
0.094	$1.837 \pm 0.014 / 1.794 \pm 0.009$	$1.483 \pm 0.011 / 1.449 \pm 0.008$	$1.775 \pm 0.014 / 1.734 \pm 0.009$	$1.498 \pm 0.012 / 1.463 \pm 0.008$
0.015	$0.762 \pm 0.007 / 0.744 \pm 0.005$	$0.647 \pm 0.006 / 0.632 \pm 0.004$	$0.766 \pm 0.007 / 0.748 \pm 0.005$	$0.645 \pm 0.006 / 0.630 \pm 0.005$
L, м	Channel			
	31-21 "0"	31-21 "1"	32-16 "0"	32-16 "1"
1.283	$1.525 \pm 0.011 / 1.489 \pm 0.007$	$1.468 \pm 0.011 / 1.433 \pm 0.007$	$1.873 \pm 0.014 / 1.829 \pm 0.008$	$1.683 \pm 0.012 / 1.643 \pm 0.008$
1.204	$1.903 \pm 0.014 / 1.858 \pm 0.009$	$1.973 \pm 0.015 / 1.927 \pm 0.010$	$2.422 \pm 0.018 / 2.365 \pm 0.011$	$2.024 \pm 0.015 / 1.976 \pm 0.009$
1.045	$3.013 \pm 0.040 / 2.942 \pm 0.036$	$3.130 \pm 0.042 / 3.057 \pm 0.037$		$3.133 \pm 0.042 / 3.060 \pm 0.037$
0.887	$3.838 \pm 0.029 / 3.748 \pm 0.018$	$4.024 \pm 0.030 / 3.929 \pm 0.019$	$4.413 \pm 0.007 / 4.212 \pm 0.020$	$3.940 \pm 0.029 / 3.847 \pm 0.018$
0.570	$4.036 \pm 0.029 / 3.942 \pm 0.017$	$4.285 \pm 0.031 / 4.185 \pm 0.018$	$4.371 \pm 0.031 / 4.269 \pm 0.018$	$4.146 \pm 0.029 / 4.049 \pm 0.017$
0.411	$3.504 \pm 0.026 / 3.421 \pm 0.016$	$3.801 \pm 0.028 / 3.712 \pm 0.017$	$4.085 \pm 0.030 / 3.990 \pm 0.018$	$3.761 \pm 0.027 / 3.673 \pm 0.017$
0.253	$2.536 \pm 0.034 / 2.476 \pm 0.030$	$2.019 \pm 0.027 / 1.971 \pm 0.024$		$2.736 \pm 0.037 / 2.672 \pm 0.032$
0.094	$1.318 \pm 0.010 / 1.288 \pm 0.007$	$1.366 \pm 0.011 / 1.334 \pm 0.007$	$1.643 \pm 0.013 / 1.604 \pm 0.008$	$1.393 \pm 0.011 / 1.360 \pm 0.007$
0.015	$0.564 \pm 0.005 / 0.551 \pm 0.004$	$0.573 \pm 0.005 / 0.559 \pm 0.004$	$0.684 \pm 0.006 / 0.668 \pm 0.005$	$0.602 \pm 0.005 / 0.588 \pm 0.004$

Table 18, cont'd.

L, m	$(R \pm \Delta R) \times 10^{-15} / (SPA \pm \Delta SPA)$			
	Channel			
	32-20 "0"	32-20 "1"	33-15 "0"	33-15 "1"
1.283	$1.844 \pm 0.014 / 1.801 \pm 0.009$	$1.628 \pm 0.012 / 1.590 \pm 0.008$	$1.623 \pm 0.012 / 1.585 \pm 0.007$	$1.491 \pm 0.011 / 1.456 \pm 0.007$
1.204	$2.297 \pm 0.017 / 2.243 \pm 0.011$	$2.049 \pm 0.016 / 2.001 \pm 0.010$	$2.034 \pm 0.016 / 1.986 \pm 0.010$	$1.920 \pm 0.015 / 1.875 \pm 0.010$
1.045	$3.587 \pm 0.048 / 3.503 \pm 0.042$	$3.098 \pm 0.042 / 3.025 \pm 0.037$	$3.508 \pm 0.047 / 3.426 \pm 0.041$	$2.999 \pm 0.040 / 2.928 \pm 0.036$
0.887	$4.216 \pm 0.031 / 4.117 \pm 0.020$	$3.841 \pm 0.029 / 3.751 \pm 0.018$	$3.980 \pm 0.030 / 3.886 \pm 0.019$	$3.763 \pm 0.029 / 3.674 \pm 0.018$
0.570	$4.396 \pm 0.031 / 4.293 \pm 0.019$	$4.064 \pm 0.029 / 3.969 \pm 0.017$	$4.064 \pm 0.029 / 3.969 \pm 0.017$	$4.172 \pm 0.030 / 4.074 \pm 0.018$
0.411	$4.080 \pm 0.030 / 3.985 \pm 0.019$	$3.724 \pm 0.028 / 3.636 \pm 0.017$	$3.694 \pm 0.028 / 3.607 \pm 0.017$	$3.675 \pm 0.027 / 3.589 \pm 0.017$
0.253	$3.119 \pm 0.042 / 3.046 \pm 0.037$	$2.688 \pm 0.036 / 2.625 \pm 0.032$	$2.997 \pm 0.040 / 2.927 \pm 0.035$	$2.845 \pm 0.038 / 2.779 \pm 0.033$
0.094	$1.601 \pm 0.012 / 1.564 \pm 0.008$	$1.394 \pm 0.011 / 1.361 \pm 0.007$	$1.385 \pm 0.011 / 1.353 \pm 0.008$	$1.336 \pm 0.011 / 1.304 \pm 0.007$
0.015	$0.668 \pm 0.006 / 0.652 \pm 0.005$	$0.622 \pm 0.006 / 0.607 \pm 0.005$	$0.599 \pm 0.006 / 0.585 \pm 0.004$	$0.566 \pm 0.005 / 0.553 \pm 0.004$
L, m	Channel			
	33-21 "0"	33-21 "1"	34-14 "0"	34-14 "1"
	1.283	$1.597 \pm 0.012 / 1.559 \pm 0.008$	$1.470 \pm 0.011 / 1.436 \pm 0.007$	$1.402 \pm 0.011 / 1.369 \pm 0.007$
1.204	$2.019 \pm 0.015 / 1.972 \pm 0.010$	$1.948 \pm 0.015 / 1.902 \pm 0.010$	$1.754 \pm 0.013 / 1.713 \pm 0.009$	$1.777 \pm 0.014 / 1.735 \pm 0.009$
1.045	$3.032 \pm 0.041 / 2.961 \pm 0.036$	$3.057 \pm 0.041 / 2.985 \pm 0.036$	$2.831 \pm 0.038 / 2.765 \pm 0.033$	$3.049 \pm 0.040 / 2.978 \pm 0.036$
0.887	$3.803 \pm 0.028 / 3.714 \pm 0.018$	$3.965 \pm 0.030 / 3.872 \pm 0.019$	$3.685 \pm 0.028 / 3.598 \pm 0.018$	$3.595 \pm 0.027 / 3.510 \pm 0.017$
0.570	$4.111 \pm 0.029 / 4.014 \pm 0.017$	$4.243 \pm 0.030 / 4.143 \pm 0.018$	$3.804 \pm 0.027 / 3.715 \pm 0.016$	$3.792 \pm 0.027 / 3.703 \pm 0.016$
0.411	$3.633 \pm 0.027 / 3.548 \pm 0.017$	$3.681 \pm 0.027 / 3.594 \pm 0.017$	$3.460 \pm 0.026 / 3.379 \pm 0.016$	$3.374 \pm 0.025 / 3.295 \pm 0.016$
0.253	$2.579 \pm 0.035 / 2.518 \pm 0.031$	$2.585 \pm 0.034 / 2.525 \pm 0.030$	$2.520 \pm 0.034 / 2.461 \pm 0.030$	$2.422 \pm 0.032 / 2.366 \pm 0.028$
0.094	$1.380 \pm 0.011 / 1.348 \pm 0.007$	$1.332 \pm 0.011 / 1.301 \pm 0.007$	$1.286 \pm 0.010 / 1.256 \pm 0.007$	$1.227 \pm 0.009 / 1.198 \pm 0.006$
0.015	$0.602 \pm 0.006 / 0.588 \pm 0.004$	$0.584 \pm 0.005 / 0.570 \pm 0.004$	$0.482 \pm 0.004 / 0.470 \pm 0.003$	$0.516 \pm 0.005 / 0.504 \pm 0.004$
L, m	Channel			
	34-16 "0"	34-16 "1"	34-20 "0"	34-20 "1"
	1.283	$1.831 \pm 0.013 / 1.788 \pm 0.008$	$1.729 \pm 0.013 / 1.688 \pm 0.008$	$2.019 \pm 0.015 / 1.972 \pm 0.009$
1.204	$2.625 \pm 0.019 / 2.564 \pm 0.012$	$2.190 \pm 0.016 / 2.138 \pm 0.010$	$2.622 \pm 0.020 / 2.560 \pm 0.013$	$2.169 \pm 0.016 / 2.118 \pm 0.011$
1.045	$3.928 \pm 0.052 / 3.836 \pm 0.046$	$3.395 \pm 0.045 / 3.316 \pm 0.039$	$3.981 \pm 0.053 / 3.887 \pm 0.046$	$3.287 \pm 0.044 / 3.210 \pm 0.038$
0.887	$4.294 \pm 0.032 / 4.194 \pm 0.020$	$4.054 \pm 0.030 / 3.959 \pm 0.019$	$4.293 \pm 0.032 / 4.192 \pm 0.020$	$3.985 \pm 0.030 / 3.891 \pm 0.019$
0.570	$4.259 \pm 0.030 / 4.159 \pm 0.018$	$4.219 \pm 0.030 / 4.120 \pm 0.017$	$4.239 \pm 0.030 / 4.139 \pm 0.018$	$4.200 \pm 0.030 / 4.101 \pm 0.018$
0.411	$4.165 \pm 0.030 / 4.068 \pm 0.018$	$3.789 \pm 0.028 / 3.701 \pm 0.017$	$4.231 \pm 0.031 / 4.132 \pm 0.019$	$3.788 \pm 0.028 / 3.699 \pm 0.017$
0.253	$3.626 \pm 0.048 / 3.541 \pm 0.042$	$2.940 \pm 0.039 / 2.871 \pm 0.034$	$3.642 \pm 0.048 / 3.557 \pm 0.042$	$2.942 \pm 0.039 / 2.874 \pm 0.034$
0.094	$1.828 \pm 0.014 / 1.785 \pm 0.009$	$1.452 \pm 0.011 / 1.418 \pm 0.007$	$1.841 \pm 0.014 / 1.798 \pm 0.010$	$1.496 \pm 0.012 / 1.461 \pm 0.008$
0.015	$0.750 \pm 0.007 / 0.732 \pm 0.005$	$0.620 \pm 0.006 / 0.606 \pm 0.004$	$0.755 \pm 0.007 / 0.738 \pm 0.005$	$0.645 \pm 0.006 / 0.630 \pm 0.005$

Table 18, cont'd.

L, m	$(R \pm \Delta R) \times 10^{-15} / (SPA \pm \Delta SPA)$	
	Channel	
	34-22 "0"	34-22 "1"
1.283	$1.452 \pm 0.011 / 1.418 \pm 0.007$	$1.304 \pm 0.010 / 1.274 \pm 0.006$
1.204	$1.858 \pm 0.014 / 1.814 \pm 0.009$	$1.727 \pm 0.013 / 1.686 \pm 0.009$
1.045	$2.916 \pm 0.039 / 2.848 \pm 0.035$	$2.754 \pm 0.037 / 2.690 \pm 0.033$
0.887	$3.771 \pm 0.028 / 3.683 \pm 0.018$	$3.547 \pm 0.027 / 3.464 \pm 0.017$
0.570	$3.869 \pm 0.028 / 3.778 \pm 0.016$	$3.899 \pm 0.028 / 3.808 \pm 0.016$
0.411	$3.472 \pm 0.026 / 3.390 \pm 0.016$	$3.505 \pm 0.026 / 3.422 \pm 0.016$
0.253	$2.415 \pm 0.033 / 2.358 \pm 0.029$	$2.434 \pm 0.033 / 2.377 \pm 0.029$
0.094	$1.290 \pm 0.010 / 1.259 \pm 0.007$	$1.234 \pm 0.010 / 1.205 \pm 0.007$
0.015	$0.536 \pm 0.005 / 0.524 \pm 0.004$	$0.551 \pm 0.005 / 0.538 \pm 0.004$

Table 19. The  $^{63}\text{Cu}$  reaction rates in lattice 21-2.

L, m	$(R \pm \Delta R) \times 10^{-15} / (SPA \pm \Delta SPA)$			
	Channel			
	28-18 "0"	28-18 "1"	29-17 "0"	29-17 "1"
1.204	$1.418 \pm 0.033 / 2.075 \pm 0.035$	$1.328 \pm 0.031 / 1.943 \pm 0.023$	$1.499 \pm 0.034 / 2.193 \pm 0.035$	$1.402 \pm 0.032 / 2.051 \pm 0.034$
1.045	$2.698 \pm 0.054 / 3.947 \pm 0.046$	$2.705 \pm 0.054 / 3.956 \pm 0.032$	$2.866 \pm 0.056 / 4.193 \pm 0.047$	$2.869 \pm 0.056 / 4.197 \pm 0.047$
0.887	$3.494 \pm 0.067 / 5.112 \pm 0.054$	$3.609 \pm 0.069 / 5.280 \pm 0.037$	$3.679 \pm 0.069 / 5.382 \pm 0.053$	$3.738 \pm 0.070 / 5.469 \pm 0.053$
0.728	$3.899 \pm 0.074 / 5.704 \pm 0.058$	$4.095 \pm 0.077 / 5.991 \pm 0.040$	$4.194 \pm 0.077 / 6.135 \pm 0.055$	$4.150 \pm 0.077 / 6.071 \pm 0.056$
0.570	$3.914 \pm 0.073 / 5.725 \pm 0.055$	$3.990 \pm 0.075 / 5.837 \pm 0.039$	$4.264 \pm 0.078 / 6.239 \pm 0.055$	$4.100 \pm 0.076 / 5.997 \pm 0.057$
0.411	$3.663 \pm 0.069 / 5.359 \pm 0.054$	$3.605 \pm 0.069 / 5.274 \pm 0.038$	$3.810 \pm 0.071 / 5.573 \pm 0.053$	$3.846 \pm 0.072 / 5.627 \pm 0.054$
0.253	$2.782 \pm 0.055 / 4.070 \pm 0.048$	$2.652 \pm 0.053 / 3.880 \pm 0.032$	$2.936 \pm 0.057 / 4.296 \pm 0.046$	$2.884 \pm 0.056 / 4.219 \pm 0.045$
0.094	$1.338 \pm 0.024 / 1.957 \pm 0.015$	$1.337 \pm 0.031 / 1.956 \pm 0.022$	$1.503 \pm 0.033 / 2.198 \pm 0.032$	$1.405 \pm 0.032 / 2.056 \pm 0.032$



Table 19, cont'd.

L, m	$(R \pm \Delta R) \times 10^{-15} / (SPA \pm \Delta SPA)$			
	Channel			
	29-19 "0"	29-19 "1"	30-16 "0"	30-16 "1"
1.204	1.506 ± 0.037 / 2.204 ± 0.041	1.412 ± 0.035 / 2.066 ± 0.040	1.549 ± 0.033 / 2.265 ± 0.032	1.485 ± 0.032 / 2.173 ± 0.031
1.045	2.821 ± 0.058 / 4.127 ± 0.053	2.911 ± 0.061 / 4.259 ± 0.056	2.937 ± 0.056 / 4.297 ± 0.044	2.768 ± 0.053 / 4.050 ± 0.044
0.887	3.736 ± 0.074 / 5.465 ± 0.062	3.707 ± 0.074 / 5.423 ± 0.064	3.919 ± 0.072 / 5.734 ± 0.050	3.772 ± 0.069 / 5.518 ± 0.049
0.728	4.157 ± 0.080 / 6.082 ± 0.065	4.289 ± 0.082 / 6.275 ± 0.066	4.215 ± 0.077 / 6.166 ± 0.052	4.272 ± 0.077 / 6.250 ± 0.053
0.570	4.175 ± 0.081 / 6.108 ± 0.065	4.178 ± 0.081 / 6.112 ± 0.066	4.215 ± 0.076 / 6.166 ± 0.052	4.184 ± 0.076 / 6.120 ± 0.052
0.411	3.648 ± 0.072 / 5.337 ± 0.061	3.756 ± 0.074 / 5.495 ± 0.064	3.862 ± 0.071 / 5.649 ± 0.050	3.868 ± 0.071 / 5.658 ± 0.050
0.253	2.954 ± 0.060 / 4.322 ± 0.054	2.898 ± 0.060 / 4.240 ± 0.056	2.953 ± 0.056 / 4.321 ± 0.043	2.887 ± 0.055 / 4.224 ± 0.044
0.094	1.435 ± 0.034 / 2.100 ± 0.037	1.423 ± 0.035 / 2.082 ± 0.038	1.456 ± 0.031 / 2.130 ± 0.031	1.452 ± 0.031 / 2.124 ± 0.030
L, m	Channel			
	30-18 "0"	30-18 "1"	30-20 "0"	30-20 "1"
	1.204	1.863 ± 0.041 / 2.725 ± 0.040	1.494 ± 0.034 / 2.185 ± 0.036	1.523 ± 0.042 / 2.228 ± 0.051
1.045	3.369 ± 0.066 / 4.929 ± 0.054	2.961 ± 0.059 / 4.331 ± 0.051	2.915 ± 0.066 / 4.265 ± 0.067	2.907 ± 0.065 / 4.253 ± 0.067
0.887	4.019 ± 0.076 / 5.879 ± 0.059	3.839 ± 0.073 / 5.616 ± 0.058	3.756 ± 0.078 / 5.494 ± 0.073	3.881 ± 0.081 / 5.677 ± 0.076
0.728	4.423 ± 0.083 / 6.471 ± 0.062	4.044 ± 0.076 / 5.916 ± 0.059	4.240 ± 0.087 / 6.203 ± 0.080	4.236 ± 0.088 / 6.196 ± 0.083
0.570	4.471 ± 0.083 / 6.541 ± 0.062	4.078 ± 0.078 / 5.966 ± 0.061	4.306 ± 0.088 / 6.299 ± 0.080	4.260 ± 0.088 / 6.232 ± 0.082
0.411	4.259 ± 0.080 / 6.230 ± 0.061	3.628 ± 0.066 / 5.307 ± 0.046	3.886 ± 0.081 / 5.685 ± 0.077	3.850 ± 0.081 / 5.632 ± 0.076
0.253	3.481 ± 0.067 / 5.092 ± 0.054	2.883 ± 0.058 / 4.217 ± 0.051	2.983 ± 0.067 / 4.363 ± 0.068	2.964 ± 0.066 / 4.335 ± 0.066
0.094	1.822 ± 0.040 / 2.666 ± 0.041	1.455 ± 0.034 / 2.128 ± 0.036	1.472 ± 0.040 / 2.153 ± 0.047	1.448 ± 0.041 / 2.118 ± 0.049
L, m	Channel			
	31-15 "0"	31-15 "1"	31-17 "0"	31-17 "1"
	1.204	1.429 ± 0.031 / 2.091 ± 0.030	1.430 ± 0.031 / 2.092 ± 0.030	1.916 ± 0.040 / 2.803 ± 0.039
1.045	2.828 ± 0.053 / 4.137 ± 0.041	2.776 ± 0.053 / 4.061 ± 0.041	3.787 ± 0.071 / 5.540 ± 0.053	3.019 ± 0.059 / 4.416 ± 0.050
0.887	3.695 ± 0.068 / 5.405 ± 0.048	3.739 ± 0.068 / 5.470 ± 0.047	4.180 ± 0.078 / 6.115 ± 0.057	3.927 ± 0.073 / 5.745 ± 0.054
0.728	4.097 ± 0.074 / 5.994 ± 0.050	4.253 ± 0.076 / 6.221 ± 0.050	4.423 ± 0.082 / 6.471 ± 0.059	4.214 ± 0.079 / 6.165 ± 0.058
0.570	4.097 ± 0.074 / 5.994 ± 0.049	4.176 ± 0.075 / 6.109 ± 0.050	4.383 ± 0.081 / 6.412 ± 0.058	4.187 ± 0.078 / 6.125 ± 0.057
0.411	3.733 ± 0.068 / 5.462 ± 0.047	3.819 ± 0.069 / 5.587 ± 0.047	4.313 ± 0.080 / 6.309 ± 0.059	3.970 ± 0.075 / 5.808 ± 0.056
0.253	2.814 ± 0.053 / 4.116 ± 0.040	2.768 ± 0.053 / 4.049 ± 0.042	3.695 ± 0.070 / 5.406 ± 0.054	3.175 ± 0.061 / 4.645 ± 0.050
0.094	1.396 ± 0.029 / 2.043 ± 0.028	1.394 ± 0.030 / 2.039 ± 0.029	1.955 ± 0.041 / 2.859 ± 0.039	1.576 ± 0.036 / 2.305 ± 0.037

Table 19, cont'd.

L, m	$(R \pm \Delta R) \times 10^{-15} / (SPA \pm \Delta SPA)$			
	Channel			
	31-19 "0"	31-19 "1"	31-21 "0"	31-21 "1"
1.204	1.861 ± 0.044 / 2.722 ± 0.046	1.620 ± 0.042 / 2.370 ± 0.048	1.429 ± 0.042 / 2.091 ± 0.051	1.343 ± 0.041 / 1.964 ± 0.051
1.045	3.612 ± 0.072 / 5.284 ± 0.062	3.158 ± 0.069 / 4.620 ± 0.068	2.770 ± 0.065 / 4.053 ± 0.070	2.835 ± 0.069 / 4.147 ± 0.075
0.887	4.246 ± 0.083 / 6.212 ± 0.069	3.870 ± 0.082 / 5.662 ± 0.077	3.635 ± 0.080 / 5.318 ± 0.080	3.864 ± 0.083 / 5.653 ± 0.082
0.728	4.508 ± 0.086 / 6.595 ± 0.069	4.255 ± 0.087 / 6.225 ± 0.079	4.117 ± 0.087 / 6.023 ± 0.083	4.375 ± 0.094 / 6.401 ± 0.091
0.570	4.521 ± 0.087 / 6.614 ± 0.069	4.274 ± 0.088 / 6.253 ± 0.081	4.091 ± 0.087 / 5.985 ± 0.084	4.212 ± 0.091 / 6.161 ± 0.089
0.411	4.341 ± 0.085 / 6.350 ± 0.071	3.980 ± 0.082 / 5.822 ± 0.076	3.652 ± 0.081 / 5.343 ± 0.082	3.892 ± 0.084 / 5.694 ± 0.082
0.253	3.684 ± 0.074 / 5.390 ± 0.065	3.140 ± 0.069 / 4.593 ± 0.069	2.714 ± 0.065 / 3.970 ± 0.072	2.892 ± 0.067 / 4.231 ± 0.070
0.094	1.821 ± 0.042 / 2.663 ± 0.044	1.622 ± 0.042 / 2.373 ± 0.049	1.461 ± 0.042 / 2.137 ± 0.050	1.418 ± 0.041 / 2.075 ± 0.051
L, m	Channel			
	32-16 "0"	32-16 "1"	32-20 "0"	32-20 "1"
	1.204	1.771 ± 0.038 / 2.590 ± 0.036	1.559 ± 0.034 / 2.281 ± 0.034	1.845 ± 0.047 / 2.699 ± 0.053
1.045	3.354 ± 0.063 / 4.907 ± 0.048	2.926 ± 0.056 / 4.281 ± 0.046	3.366 ± 0.074 / 4.925 ± 0.075	2.972 ± 0.068 / 4.348 ± 0.071
0.887	4.062 ± 0.074 / 5.942 ± 0.052	3.823 ± 0.071 / 5.593 ± 0.052	4.155 ± 0.086 / 6.078 ± 0.080	3.819 ± 0.081 / 5.586 ± 0.078
0.728	4.398 ± 0.080 / 6.434 ± 0.054	4.372 ± 0.079 / 6.396 ± 0.054	4.540 ± 0.094 / 6.641 ± 0.087	4.208 ± 0.089 / 6.156 ± 0.085
0.570	4.497 ± 0.081 / 6.578 ± 0.054	4.279 ± 0.078 / 6.260 ± 0.053	4.494 ± 0.093 / 6.574 ± 0.087	4.198 ± 0.088 / 6.142 ± 0.084
0.411	4.191 ± 0.077 / 6.131 ± 0.054	3.927 ± 0.072 / 5.744 ± 0.052	4.245 ± 0.090 / 6.210 ± 0.085	3.944 ± 0.084 / 5.770 ± 0.080
0.253	3.462 ± 0.065 / 5.064 ± 0.048	2.968 ± 0.057 / 4.342 ± 0.045	3.434 ± 0.074 / 5.023 ± 0.073	2.955 ± 0.068 / 4.324 ± 0.071
0.094	1.739 ± 0.036 / 2.543 ± 0.033	1.468 ± 0.032 / 2.148 ± 0.031	1.787 ± 0.046 / 2.614 ± 0.052	1.514 ± 0.043 / 2.215 ± 0.053
L, m	Channel			
	33-15 "0"	33-15 "1"	33-21 "0"	33-21 "1"
	1.204	1.472 ± 0.032 / 2.154 ± 0.031	1.353 ± 0.030 / 1.980 ± 0.030	1.477 ± 0.043 / 2.161 ± 0.052
1.045	2.889 ± 0.055 / 4.227 ± 0.042	2.754 ± 0.053 / 4.029 ± 0.042	2.839 ± 0.068 / 4.153 ± 0.074	2.763 ± 0.067 / 4.042 ± 0.073
0.887	3.833 ± 0.070 / 5.608 ± 0.049	3.607 ± 0.067 / 5.276 ± 0.049	3.516 ± 0.080 / 5.143 ± 0.084	3.687 ± 0.084 / 5.393 ± 0.087
0.728	4.173 ± 0.076 / 6.104 ± 0.051	4.078 ± 0.074 / 5.966 ± 0.051	4.154 ± 0.091 / 6.077 ± 0.091	4.223 ± 0.093 / 6.178 ± 0.092
0.570	4.174 ± 0.076 / 6.107 ± 0.051	4.152 ± 0.075 / 6.075 ± 0.052	4.107 ± 0.089 / 6.008 ± 0.087	4.309 ± 0.091 / 6.304 ± 0.087
0.411	3.768 ± 0.069 / 5.513 ± 0.049	3.690 ± 0.068 / 5.398 ± 0.049	3.809 ± 0.085 / 5.572 ± 0.086	3.822 ± 0.085 / 5.591 ± 0.086
0.253	2.924 ± 0.055 / 4.278 ± 0.042	2.824 ± 0.053 / 4.131 ± 0.041	2.797 ± 0.067 / 4.092 ± 0.073	2.879 ± 0.069 / 4.212 ± 0.075
0.094	1.439 ± 0.030 / 2.106 ± 0.029	1.341 ± 0.029 / 1.962 ± 0.028	1.376 ± 0.040 / 2.013 ± 0.049	1.369 ± 0.042 / 2.003 ± 0.052

Table 19, cont'd.

L, m	$(R \pm \Delta R) \times 10^{-15} / (SPA \pm \Delta SPA)$			
	Channel			
	34-14 "0"	34-14 "1"	34-16 "0"	34-16 "1"
1.204	1.302 ± 0.028 / 1.905 ± 0.028	1.194 ± 0.027 / 1.746 ± 0.027	1.917 ± 0.040 / 2.804 ± 0.037	1.636 ± 0.035 / 2.394 ± 0.034
1.045	2.610 ± 0.049 / 3.818 ± 0.039	2.388 ± 0.046 / 3.494 ± 0.038	3.660 ± 0.068 / 5.354 ± 0.051	3.077 ± 0.059 / 4.501 ± 0.048
0.887	3.410 ± 0.063 / 4.988 ± 0.046	3.250 ± 0.060 / 4.754 ± 0.043	4.109 ± 0.075 / 6.011 ± 0.053	3.933 ± 0.073 / 5.753 ± 0.055
0.728	3.816 ± 0.069 / 5.583 ± 0.048	3.684 ± 0.067 / 5.390 ± 0.045	4.314 ± 0.079 / 6.311 ± 0.054	4.348 ± 0.080 / 6.361 ± 0.057
0.570	3.938 ± 0.071 / 5.762 ± 0.049	3.796 ± 0.069 / 5.553 ± 0.047	4.295 ± 0.079 / 6.282 ± 0.055	4.338 ± 0.080 / 6.346 ± 0.056
0.411	3.580 ± 0.066 / 5.237 ± 0.047	3.509 ± 0.065 / 5.134 ± 0.047	4.300 ± 0.079 / 6.290 ± 0.055	4.051 ± 0.075 / 5.926 ± 0.054
0.253	2.689 ± 0.051 / 3.933 ± 0.040	2.542 ± 0.049 / 3.719 ± 0.039	3.735 ± 0.069 / 5.464 ± 0.051	3.140 ± 0.060 / 4.594 ± 0.047
0.094	1.317 ± 0.029 / 1.926 ± 0.028	1.270 ± 0.028 / 1.858 ± 0.027	1.945 ± 0.040 / 2.846 ± 0.036	1.560 ± 0.034 / 2.283 ± 0.034
L, m	Channel			
	34-18 "0"	34-18 "1"	34-18 "2"	34-18 "3"
	1.204	2.173 ± 0.046 / 3.179 ± 0.043	2.180 ± 0.047 / 3.189 ± 0.045	2.237 ± 0.048 / 3.272 ± 0.046
1.045	3.860 ± 0.073 / 5.646 ± 0.056	3.803 ± 0.073 / 5.563 ± 0.058	3.984 ± 0.077 / 5.828 ± 0.062	3.928 ± 0.076 / 5.746 ± 0.062
0.887	3.483 ± 0.067 / 5.096 ± 0.055	3.453 ± 0.067 / 5.052 ± 0.055	3.485 ± 0.069 / 5.099 ± 0.058	3.453 ± 0.069 / 5.051 ± 0.060
0.728	3.419 ± 0.066 / 5.002 ± 0.053	3.376 ± 0.066 / 4.939 ± 0.054	3.403 ± 0.067 / 4.978 ± 0.057	3.388 ± 0.067 / 4.956 ± 0.058
0.570	3.480 ± 0.067 / 5.090 ± 0.054	3.386 ± 0.065 / 4.953 ± 0.053	3.397 ± 0.067 / 4.969 ± 0.057	3.364 ± 0.067 / 4.922 ± 0.057
0.411	3.798 ± 0.072 / 5.556 ± 0.057	3.856 ± 0.073 / 5.641 ± 0.058	3.715 ± 0.073 / 5.435 ± 0.061	3.744 ± 0.073 / 5.477 ± 0.061
0.253	3.964 ± 0.076 / 5.800 ± 0.059	3.890 ± 0.074 / 5.691 ± 0.057	3.862 ± 0.074 / 5.650 ± 0.060	3.833 ± 0.074 / 5.607 ± 0.061
0.094	2.072 ± 0.044 / 3.032 ± 0.042	2.084 ± 0.044 / 3.049 ± 0.042	2.069 ± 0.045 / 3.026 ± 0.044	2.124 ± 0.046 / 3.107 ± 0.045
L, m	Channel			
	34-20 "0"	34-20 "1"	34-22 "0"	34-22 "1"
	1.204	1.967 ± 0.050 / 2.877 ± 0.057	1.532 ± 0.043 / 2.241 ± 0.052	1.384 ± 0.042 / 2.025 ± 0.052
1.045	3.782 ± 0.081 / 5.533 ± 0.079	3.052 ± 0.069 / 4.465 ± 0.071	2.552 ± 0.064 / 3.734 ± 0.072	2.500 ± 0.063 / 3.657 ± 0.071
0.887	4.247 ± 0.090 / 6.212 ± 0.085	3.794 ± 0.082 / 5.550 ± 0.081	3.556 ± 0.080 / 5.203 ± 0.082	3.371 ± 0.080 / 4.932 ± 0.085
0.728	4.499 ± 0.094 / 6.582 ± 0.087	4.310 ± 0.092 / 6.305 ± 0.088	4.023 ± 0.088 / 5.885 ± 0.087	3.902 ± 0.086 / 5.708 ± 0.087
0.570	4.374 ± 0.093 / 6.398 ± 0.088	4.172 ± 0.089 / 6.104 ± 0.087	3.951 ± 0.088 / 5.780 ± 0.090	3.947 ± 0.087 / 5.775 ± 0.087
0.411	4.301 ± 0.091 / 6.292 ± 0.087	3.979 ± 0.086 / 5.821 ± 0.084	3.569 ± 0.080 / 5.222 ± 0.082	3.504 ± 0.080 / 5.126 ± 0.082
0.253	3.865 ± 0.083 / 5.653 ± 0.081	3.099 ± 0.072 / 4.534 ± 0.076	2.602 ± 0.064 / 3.806 ± 0.071	2.594 ± 0.064 / 3.794 ± 0.072
0.094	1.962 ± 0.051 / 2.871 ± 0.058	1.554 ± 0.043 / 2.274 ± 0.052	1.293 ± 0.040 / 1.892 ± 0.050	1.290 ± 0.040 / 1.887 ± 0.050

Table 20. The  $^{63}\text{Cu}$  reaction rates in the single-segment containers in lattice 21-1-5(M2).

L, м	$(R \pm \Delta R) \times 10^{-15} / (SPA \pm \Delta SPA)$			
	Channel			
	Container No. 1	Container No. 2	Container No. 3	Пенал №4
0.897	$4.989 \pm 0.110 / 4.872 \pm 0.035$	$5.044 \pm 0.111 / 4.925 \pm 0.037$	$4.928 \pm 0.109 / 4.812 \pm 0.038$	$5.162 \pm 0.115 / 5.041 \pm 0.040$
0.848	$4.427 \pm 0.101 / 4.323 \pm 0.041$	$4.503 \pm 0.200 / 4.397 \pm 0.173$	$4.457 \pm 0.126 / 4.352 \pm 0.083$	$4.732 \pm 0.119 / 4.621 \pm 0.066$
0.800	$4.148 \pm 0.089 / 4.051 \pm 0.023$	$4.375 \pm 0.114 / 4.272 \pm 0.067$	$4.280 \pm 0.100 / 4.180 \pm 0.044$	$4.603 \pm 0.113 / 4.495 \pm 0.059$
0.751	$4.150 \pm 0.095 / 4.053 \pm 0.038$	$4.192 \pm 0.093 / 4.094 \pm 0.031$	$4.214 \pm 0.104 / 4.116 \pm 0.055$	$4.600 \pm 0.112 / 4.492 \pm 0.056$
0.702	$4.109 \pm 0.091 / 4.012 \pm 0.031$	$4.159 \pm 0.088 / 4.062 \pm 0.018$	$4.232 \pm 0.102 / 4.133 \pm 0.050$	$4.547 \pm 0.120 / 4.440 \pm 0.072$
0.653	$4.049 \pm 0.086 / 3.954 \pm 0.019$	$4.126 \pm 0.091 / 4.029 \pm 0.030$	$4.253 \pm 0.108 / 4.153 \pm 0.061$	$4.474 \pm 0.120 / 4.369 \pm 0.074$
0.604	$3.978 \pm 0.104 / 3.885 \pm 0.061$	$4.117 \pm 0.095 / 4.021 \pm 0.041$	$4.174 \pm 0.103 / 4.076 \pm 0.054$	$4.443 \pm 0.100 / 4.339 \pm 0.038$
0.554	$4.007 \pm 0.093 / 3.913 \pm 0.040$	$4.076 \pm 0.093 / 3.981 \pm 0.037$	$4.170 \pm 0.095 / 4.072 \pm 0.038$	$4.420 \pm 0.102 / 4.316 \pm 0.043$
0.505	$4.070 \pm 0.086 / 3.974 \pm 0.017$	$4.134 \pm 0.097 / 4.037 \pm 0.044$	$4.195 \pm 0.090 / 4.097 \pm 0.020$	$4.491 \pm 0.098 / 4.386 \pm 0.030$
0.456	$4.178 \pm 0.090 / 4.080 \pm 0.021$	$4.268 \pm 0.100 / 4.167 \pm 0.046$	$4.435 \pm 0.149 / 4.331 \pm 0.115$	$4.509 \pm 0.118 / 4.403 \pm 0.071$
0.412	$4.528 \pm 0.100 / 4.422 \pm 0.032$	$4.436 \pm 0.098 / 4.332 \pm 0.032$	$4.658 \pm 0.103 / 4.548 \pm 0.036$	$4.712 \pm 0.105 / 4.602 \pm 0.037$

Table 21. The  $^{63}\text{Cu}$  reaction rates in the single-segment containers in lattice 21-2.

L, м	$(R \pm \Delta R) \times 10^{-15} / (SPA \pm \Delta SPA)$		
	Channel		
	Container No. 2	Container No. 3	Container No. 4
0.897	$4.120 \pm 0.062 / 6.028 \pm 0.091$	$4.356 \pm 0.064 / 6.373 \pm 0.093$	$4.673 \pm 0.066 / 6.838 \pm 0.097$
0.848	$3.883 \pm 0.062 / 5.682 \pm 0.090$	$4.158 \pm 0.064 / 6.084 \pm 0.094$	$4.454 \pm 0.066 / 6.517 \pm 0.097$
0.800	$3.826 \pm 0.061 / 5.598 \pm 0.089$	$4.090 \pm 0.064 / 5.984 \pm 0.093$	$4.366 \pm 0.066 / 6.389 \pm 0.097$
0.751	$3.776 \pm 0.061 / 5.525 \pm 0.089$	$4.049 \pm 0.065 / 5.925 \pm 0.095$	$4.369 \pm 0.067 / 6.393 \pm 0.098$
0.702	$3.868 \pm 0.060 / 5.660 \pm 0.088$	$4.094 \pm 0.067 / 5.990 \pm 0.098$	$4.411 \pm 0.065 / 6.454 \pm 0.095$
0.653	$3.800 \pm 0.061 / 5.560 \pm 0.089$	$4.086 \pm 0.062 / 5.979 \pm 0.091$	$4.408 \pm 0.065 / 6.450 \pm 0.095$
0.604	$3.826 \pm 0.059 / 5.599 \pm 0.087$	$4.034 \pm 0.064 / 5.903 \pm 0.093$	$4.384 \pm 0.066 / 6.414 \pm 0.097$
0.554	$3.820 \pm 0.060 / 5.590 \pm 0.087$	$4.144 \pm 0.064 / 6.063 \pm 0.093$	$4.477 \pm 0.066 / 6.551 \pm 0.097$
0.505	$3.979 \pm 0.063 / 5.822 \pm 0.092$	$4.224 \pm 0.067 / 6.181 \pm 0.097$	$4.486 \pm 0.067 / 6.564 \pm 0.098$
0.456	$4.010 \pm 0.063 / 5.868 \pm 0.092$	$4.243 \pm 0.066 / 6.209 \pm 0.097$	$4.460 \pm 0.066 / 6.526 \pm 0.097$
0.412	$4.227 \pm 0.062 / 6.185 \pm 0.091$	$4.423 \pm 0.064 / 6.472 \pm 0.094$	$4.642 \pm 0.065 / 6.792 \pm 0.096$

## 11. Experimental results

Presented here are the results of experimental determining the  $^{235}\text{U}(\text{n},\text{f})$ ,  $^{238}\text{U}(\text{n},\gamma)$ ,  $^{55}\text{Mn}(\text{n},\gamma)$ ,  $^{63}\text{Cu}(\text{n},\gamma)$ ,  $^{197}\text{Au}(\text{n},\gamma)$ ,  $^{176}\text{Lu}(\text{n},\gamma)$ ,  $^{115}\text{In}(\text{n},\text{n}')$ ,  $^{27}\text{Al}(\text{n},\alpha)$ , and  $^{64}\text{Zn}(\text{n},\text{p})$  reaction rates. Additionally, the  $^{115}\text{In}(\text{n},\gamma)$ ,  $^{115}\text{In}(\text{n},2\text{n}) + ^{113}\text{In}(\text{n},\gamma)$ ,  $^{64}\text{Zn}(\text{n},\gamma)$ ,  $^{68}\text{Zn}(\text{n},\gamma)$  reaction rates have been determined. The restricted MAKET facility power has prevented us from determining the  $^{238}\text{U}(\text{n},\text{f})$  and  $^{64}\text{Zn}(\text{n},2\text{n})$  reaction rates. The desired reaction rates were determined by formulas (15) and (17). Tables 22 and 23 present the results.

Tables 24-26 present the characteristics and the isotopic composition of the irradiated samples. Table 27 presents the nuclear-physics characteristics of the nuclide produced. The characteristics were used in measuring the reaction rates.

Table 28 presents the results of experimental determining the actinide fission reaction rates measured with SSNTDs (formula (23)). The actinides are listed in Table 1 above.

Table 22. Reaction rates at different radii of SBM in lattice 21-1-5(M2).

Reaction	0 mm $R \pm \Delta R, \text{c}^{-1}$	46.5 mm $R \pm \Delta R, \text{c}^{-1}$	72 mm $R \pm \Delta R, \text{c}^{-1}$	96.5 mm $R \pm \Delta R, \text{c}^{-1}$
$^{235}\text{U}(\text{n},\text{f})$	$(4.96 \pm 0.13) \cdot 10^{-13}$	$(4.95 \pm 0.09) \cdot 10^{-13}$	$(5.28 \pm 0.15) \cdot 10^{-13}$	$(5.35 \pm 0.13) \cdot 10^{-13}$
$^{238}\text{U}(\text{n},\gamma)$	$(8.91 \pm 0.29) \cdot 10^{-15}$	$(9.13 \pm 0.34) \cdot 10^{-15}$	$(9.35 \pm 0.37) \cdot 10^{-15}$	$(9.47 \pm 0.41) \cdot 10^{-15}$
$^{55}\text{Mn}(\text{n},\gamma)$	$(1.26 \pm 0.01) \cdot 10^{-14}$	$(1.28 \pm 0.02) \cdot 10^{-14}$	$(1.31 \pm 0.02) \cdot 10^{-14}$	$(1.37 \pm 0.02) \cdot 10^{-14}$
$^{63}\text{Cu}(\text{n},\gamma)$	$(4.50 \pm 0.27) \cdot 10^{-15}$	$(4.43 \pm 0.18) \cdot 10^{-15}$	$(4.70 \pm 0.22) \cdot 10^{-15}$	$(4.61 \pm 0.19) \cdot 10^{-15}$
$^{197}\text{Au}(\text{n},\gamma)$	$(1.96 \pm 0.03) \cdot 10^{-13}$	$(1.98 \pm 0.04) \cdot 10^{-13}$	$(2.01 \pm 0.03) \cdot 10^{-13}$	$(2.06 \pm 0.03) \cdot 10^{-13}$
$^{176}\text{Lu}(\text{n},\gamma)$	$(4.14 \pm 0.13) \cdot 10^{-12}$	$(4.18 \pm 0.13) \cdot 10^{-12}$	$(4.21 \pm 0.13) \cdot 10^{-12}$	$(4.38 \pm 0.14) \cdot 10^{-12}$
$^{115}\text{In}(\text{n},\gamma)$	$(1.36 \pm 0.03) \cdot 10^{-13}$	$(1.41 \pm 0.03) \cdot 10^{-13}$	$(1.47 \pm 0.02) \cdot 10^{-13}$	$(1.55 \pm 0.03) \cdot 10^{-13}$
$^{115}\text{In}(\text{n},\text{n}')$	$(1.53 \pm 0.07) \cdot 10^{-17}$	$(1.68 \pm 0.08) \cdot 10^{-17}$	$(1.80 \pm 0.09) \cdot 10^{-17}$	$(2.09 \pm 0.11) \cdot 10^{-17}$
$^{115}\text{In}(\text{n},2\text{n})$	$(5.09 \pm 0.15) \cdot 10^{-16}$	$(5.18 \pm 0.15) \cdot 10^{-16}$	$(5.30 \pm 0.18) \cdot 10^{-16}$	$(5.31 \pm 0.19) \cdot 10^{-16}$
$^{27}\text{Al}(\text{n},\alpha)$	$(5.30 \pm 0.22) \cdot 10^{-20}$	$(7.86 \pm 0.28) \cdot 10^{-20}$	$(6.58 \pm 0.26) \cdot 10^{-20}$	$(8.40 \pm 0.30) \cdot 10^{-20}$
$^{64}\text{Zn}(\text{n},\text{p})$	$(2.41 \pm 0.12) \cdot 10^{-18}$	$(2.52 \pm 0.09) \cdot 10^{-18}$	$(2.92 \pm 0.11) \cdot 10^{-18}$	$(3.36 \pm 0.12) \cdot 10^{-18}$
$^{64}\text{Zn}(\text{n},\gamma)$	$(7.26 \pm 0.02) \cdot 10^{-16}$	$(7.35 \pm 0.14) \cdot 10^{-16}$	$(7.52 \pm 0.19) \cdot 10^{-16}$	$(8.02 \pm 0.19) \cdot 10^{-16}$
$^{68}\text{Zn}(\text{n},\gamma)$	$(9.36 \pm 0.64) \cdot 10^{-18}$	$(1.08 \pm 0.07) \cdot 10^{-16}$	$(1.01 \pm 0.07) \cdot 10^{-16}$	$(1.06 \pm 0.08) \cdot 10^{-16}$

Table 23. Reaction rates at different radii of SBM in lattice 21-2.

Reaction	46.5 mm $R \pm \Delta R, \text{c}^{-1}$	72 mm $R \pm \Delta R, \text{c}^{-1}$	96.5 mm $R \pm \Delta R, \text{c}^{-1}$
$^{235}\text{U}(\text{n},\text{f})$	$(4.19 \pm 0.10) \cdot 10^{-13}$	$(4.76 \pm 0.12) \cdot 10^{-13}$	$(5.13 \pm 0.13) \cdot 10^{-13}$
$^{238}\text{U}(\text{n},\gamma)$	$(9.08 \pm 0.30) \cdot 10^{-15}$	$(1.01 \pm 0.03) \cdot 10^{-14}$	$(9.93 \pm 0.33) \cdot 10^{-15}$
$^{55}\text{Mn}(\text{n},\gamma)$	$(1.18 \pm 0.02) \cdot 10^{-14}$	$(1.22 \pm 0.02) \cdot 10^{-14}$	$(1.35 \pm 0.02) \cdot 10^{-14}$
$^{63}\text{Cu}(\text{n},\gamma)$	$(3.90 \pm 0.02) \cdot 10^{-15}$	$(3.97 \pm 0.15) \cdot 10^{-15}$	$(4.44 \pm 0.20) \cdot 10^{-15}$
$^{197}\text{Au}(\text{n},\gamma)$	$(1.93 \pm 0.04) \cdot 10^{-13}$	$(1.95 \pm 0.04) \cdot 10^{-13}$	$(2.16 \pm 0.05) \cdot 10^{-13}$
$^{176}\text{Lu}(\text{n},\gamma)$	$(3.86 \pm 0.23) \cdot 10^{-12}$	$(3.96 \pm 0.24) \cdot 10^{-12}$	$(4.36 \pm 0.26) \cdot 10^{-12}$
$^{115}\text{In}(\text{n},\gamma)$	$(1.26 \pm 0.03) \cdot 10^{-13}$	$(1.35 \pm 0.04) \cdot 10^{-13}$	$(1.45 \pm 0.02) \cdot 10^{-13}$
$^{115}\text{In}(\text{n},\text{n}')$	$(3.37 \pm 0.21) \cdot 10^{-17}$	$(2.42 \pm 0.23) \cdot 10^{-17}$	$(2.78 \pm 0.25) \cdot 10^{-17}$
$^{115}\text{In}(\text{n},2\text{n})$	$(8.94 \pm 0.23) \cdot 10^{-16}$	$(8.94 \pm 0.23) \cdot 10^{-16}$	$(9.17 \pm 0.23) \cdot 10^{-16}$
$^{27}\text{Al}(\text{n},\alpha)$	$(1.08 \pm 0.03) \cdot 10^{-19}$	$(8.36 \pm 0.36) \cdot 10^{-20}$	$(9.68 \pm 0.28) \cdot 10^{-20}$

$^{64}\text{Zn}(n,p)$	$(5.57 \pm 0.12) \cdot 10^{-18}$	$(4.34 \pm 0.16) \cdot 10^{-18}$	$(4.34 \pm 0.25) \cdot 10^{-18}$
$^{64}\text{Zn}(n,\gamma)$	$(7.14 \pm 0.10) \cdot 10^{-16}$	$(7.40 \pm 0.11) \cdot 10^{-16}$	$(7.96 \pm 0.12) \cdot 10^{-16}$
$^{68}\text{Zn}(n,\gamma)$	$(9.68 \pm 0.32) \cdot 10^{-17}$	$(1.03 \pm 0.03) \cdot 10^{-16}$	$(1.15 \pm 0.04) \cdot 10^{-16}$



Table 24. Parameters of the experimental samples irradiated in lattice 21-1-5(M2).

Sample	R, mm							
	0		46.5		72.0		96.5	
	Ø, MM	W, mГ	Ø, MM	W, mГ	Ø, MM	W, mГ	Ø, MM	W, mГ
<sup>235</sup> U	6.3	16.3 / (0.982- <sup>235</sup> U)	6.3	17.0 / (1.103- <sup>235</sup> U)	6.3	16.6 / (0.964 - <sup>235</sup> U)	6.3	16.8 / 0.994 - <sup>235</sup> U
<sup>238</sup> U	7.0	53.7	7.0	52.8	7.0	52.7	7.0	51.5
<sup>nat</sup> In	10.5	1317.0	10.5	1312.7	10.5	1340.1	10.5	1299.7
Zn	10.5	448.0	10.5	433.8	10.5	437.2	10.5	445.3
<sup>nat</sup> In	7.0	84.0	7.0	79.5	7.0	81.0	7.0	76.4
<sup>27</sup> Al	10.5	225.6	10.5	228.6	10.5	228.4	10.5	229.0
MCS *	7.0	8.4	7.0	8.7	7.0	8.5	7.0	9.2

\* Multi-composition sample

Table 25. Parameters of the experimental samples irradiated in lattice 21-2.

Sample	R, mm					
	46.5		72.0		96.5	
	Ø, MM	W, mГ	Ø, MM	W, mГ	Ø, MM	W, mГ
<sup>235</sup> U	6.3	16.9 / (1.160 - <sup>235</sup> U)	6.3	17.1 / (1.090- <sup>235</sup> U)	6.3	17.2 / (1.100 - <sup>235</sup> U)
<sup>238</sup> U	7.0	55.0	7.0	52.5	7.0	54.9
Zn	10.5	437.9	10.5	448.8	10.5	395.6
<sup>nat</sup> In	7.0	76.8	7.0	72.2	7.0	71.0
<sup>27</sup> Al	10.5	225.0	10.5	226.6	10.5	227.0
MCS *	7.0	8.6	7.0	9.3	7.0	7.5

\* Multi-composition sample



Table 26. Isotopic composition of samples.

Sample	State of aggregation	Isotopic composition, at.
$^{235}\text{U}$	Pseudo-alloy with Al (Al + UO <sub>2</sub> )	-
$^{238}\text{U}$	Metal foil	$^{235}\text{U}$ - 0.495; $^{238}\text{U}$ - 99.505
$^{\text{nat}}\text{In}$	Metal foil	$^{115}\text{In}$ - 95.7; $^{113}\text{In}$ - 4.3
Zn	Metal foil	$^{64}\text{Zn}$ - 99.4±0.1; $^{66}\text{Zn}$ - 0.39; $^{67}\text{Zn}$ - 0.04; $^{68}\text{Zn}$ - 0.17; $^{70}\text{Zn}$ < 0.02
$^{27}\text{Al}$	Metal foil	$^{27}\text{Al}$ - 100
Multi-composition sample (MCS)	Alloy Al (base)+ $^{55}\text{Mn}$ + $^{\text{nat}}\text{Cu}$ + $^{197}\text{Au}$ + $^{\text{nat}}\text{Lu}$	$^{55}\text{Mn}$ - 1.685; $^{176}\text{Lu}$ - 0.0515; $^{63}\text{Cu}$ - 1.768; $^{197}\text{Au}$ - 0.220
SSNTD detectors (via mass-spectrometry analysis)		
$^{235}\text{U}$	$^{235}\text{U}$ - 99.97±0.003; $^{233}\text{U}$ < 2·10 <sup>-4</sup> ; $^{234}\text{U}$ - 3.23·10 <sup>-3</sup> ; $^{236}\text{U}$ - 2.67·10 <sup>-3</sup> ; $^{238}\text{U}$ - 1.99·10 <sup>-2</sup>	
$^{237}\text{Np}$	$^{237}\text{Np}$ - 99.99; $^{233}\text{U}$ < 0.001	
$^{238}\text{Pu}$	$^{238}\text{Pu}$ - 99.160; $^{239}\text{Pu}$ - 0.7887; $^{240}\text{Pu}$ - 3.465·10 <sup>-2</sup> ; $^{241}\text{Pu}$ - 1.27·10 <sup>-3</sup> ; $^{242}\text{Pu}$ - 1.52·10 <sup>-2</sup>	
$^{239}\text{Pu}$	$^{239}\text{Pu}$ - 99.99	
$^{240}\text{Pu}$	$^{240}\text{Pu}$ - 99.517; $^{239}\text{Pu}$ - 0.386; $^{241}\text{Pu}$ - 0.094; $^{242}\text{Pu}$ - 2.76·10 <sup>-3</sup>	
$^{241}\text{Pu}$	$^{241}\text{Pu}$ - 99.995; $^{239}\text{Pu}$ - 7.43·10 <sup>-4</sup> ; $^{240}\text{Pu}$ - 6.79·10 <sup>-4</sup> ; $^{242}\text{Pu}$ - 3.72·10 <sup>-3</sup> ; $^{244}\text{Pu}$ - < 1·10 <sup>-4</sup>	
$^{242\text{m}}\text{Am}$	$^{242\text{m}}\text{Am}$ - 84.37; $^{241}\text{Am}$ - 15.07	
$^{243}\text{Cm}$	$^{243}\text{Cm}$ - 98.237; $^{244}\text{Cm}$ - 1.71	
$^{245}\text{Cm}$	$^{245}\text{Cm}$ - 98.96; $^{244}\text{Cm}$ - 0.62; $^{243}\text{Cm}$ - 0.41	
$^{247}\text{Cm}$	$^{247}\text{Cm}$ - 83.20; $^{244}\text{Cm}$ - 5.59; $^{245}\text{Cm}$ - 5.07; $^{246}\text{Cm}$ - 5.28; $^{248}\text{Cm}$ - 0.86	
Main isotope admixtures in SSNTD detectors (via alpha-spectrometry analysis)		
$^{235}\text{U}$	-	
$^{237}\text{Np}$	$^{235}\text{U}$ - 0.0007	
$^{238}\text{Pu}$	$^{239}\text{Pu}$ - 0.7794	
$^{239}\text{Pu}$	-	
$^{240}\text{Pu}$	$^{239}\text{Pu}$ - 0.3423; $^{241}\text{Pu}$ - 0.0906	
$^{241}\text{Pu}$	-	
$^{242\text{m}}\text{Am}$	$^{241}\text{Am}$ - 20.56	
$^{243}\text{Cm}$	$^{244}\text{Cm}$ - 1.70	
$^{245}\text{Cm}$	$^{244}\text{Cm}$ - 0.5755; $^{243}\text{Cm}$ - 0.3759	
$^{247}\text{Cm}$	$^{244}\text{Cm}$ - 14.52; $^{245}\text{Cm}$ - 16.23; $^{246}\text{Cm}$ - 16.60	

Table 27. Nuclear-physics characteristics of nuclides.

Nuclide	$T_{1/2}$ , c	$E_{\gamma}$ , keV	$\eta_{\gamma}$ , %	$\varepsilon_{H=40\text{ mm}}$ , %
$^{239}\text{Np}$	$(2.036016 \pm 0.000147) \cdot 10^5$	106.123	27.2±0.4	4.02±0.08
		277.599	14.38±0.21	2.13±0.04
$^{56}\text{Mn}$	$(9.28404 \pm 0.00036) \cdot 10^3$	846.754	98.9±0.3	0.744±0.009
		1810.72	27.2±0.8	0.357±0.006
$^{64}\text{Cu}$	$(4.572 \pm 0.00072) \cdot 10^4$	511A	34.79±0.40	1.21±0.02
$^{198}\text{Au}$	$(2.32864 \pm 0.00018) \cdot 10^5$	411.802	95.58±0.12	1.48±0.02
$^{177}\text{Lu}$	$(5.818176 \pm 0.010368) \cdot 10^5$	208.3664	57.7±1.2	2.76±0.06
$^{115\text{m}}\text{In}$	$(1.61496 \pm 0.00144) \cdot 10^4$	336.24	45.8±2.2	1.79±0.03
$^{24}\text{Na}$	$(5.38524 \pm 0.000432) \cdot 10^4$	1369	100	0.467±0.007
$^{116}\text{In}$	$(3.2574 \pm 0.0102) \cdot 10^3$	416.86	27.7±1.24	1.47±0.02
		1097.3	56.2±1.2	0.579±0.008
		1293.54	84.4±1.8	0.494±0.007
$^{114}\text{In}$	$(4.277664 \pm 0.000864) \cdot 10^6$	190.27	15.56±0.16	2.97±0.06
$^{65}\text{Zn}$	$(2.1104064 \pm 0.0022464) \cdot 10^7$	1115.546	50.60±0.24	0.570±0.007
$^{69}\text{Zn}$	$(4.9536 \pm 0.0072) \cdot 10^4$	438.634	94.77±0.20	1.40±0.02

The  $^{235}\text{U}$ ,  $^{143}\text{Ce}$ , and  $^{97}\text{Zr}$  nuclear-physics characteristics can be found in Table 13.

Table 28. The SSNTD-measured actinide fission rates.

Isotope	Lattice 21-1-5(M2)							
	0 mm		46.5 mm		72 mm		96.5 mm	
	R, c <sup>-1</sup>	%	R, c <sup>-1</sup>	%	R, c <sup>-1</sup>	%	R, c <sup>-1</sup>	%
$^{235}\text{U}$	$(5.109 \pm 0.189) \cdot 10^{-13}$	3.70	$(5.370 \pm 0.193) \cdot 10^{-13}$	3.60	$(5.115 \pm 0.189) \cdot 10^{-13}$	3.70	$(4.985 \pm 0.199) \cdot 10^{-13}$	4.00
$^{239}\text{Pu}$	$(7.653 \pm 2.855) \cdot 10^{-13}$	3.73	$(8.349 \pm 0.310) \cdot 10^{-13}$	3.70	$(7.221 \pm 0.271) \cdot 10^{-13}$	3.76	$(7.891 \pm 0.294) \cdot 10^{-13}$	3.73
$^{237}\text{Np}$	$(2.118 \pm 0.091) \cdot 10^{-16}$	4.31	-	-	-	-	-	-
$^{238}\text{Pu}$	$(1.944 \pm 0.079) \cdot 10^{-14}$	4.07	-	-	-	-	-	-
$^{240}\text{Pu}$	$(3.960 \pm 0.163) \cdot 10^{-15}$	4.11	-	-	-	-	-	-
$^{241}\text{Pu}$	$(8.854 \pm 0.390) \cdot 10^{-13}$	4.41	-	-	-	-	-	-
$^{242\text{m}}\text{Am}$	$(6.417 \pm 0.343) \cdot 10^{-12}$	5.35	-	-	-	-	-	-
$^{243}\text{Cm}$	$(6.541 \pm 0.332) \cdot 10^{-13}$	5.07	-	-	-	-	-	-
$^{245}\text{Cm}$	$(1.456 \pm 0.079) \cdot 10^{-12}$	5.40	-	-	-	-	-	-
$^{247}\text{Cm}$	$(2.444 \pm 0.151) \cdot 10^{-13}$	6.20	-	-	-	-	-	-
Isotope	Lattice 21-2							
	0 mm		46.5 mm		72 mm		96.5 mm	
	R, c <sup>-1</sup>	%	R, c <sup>-1</sup>	%	R, c <sup>-1</sup>	%	R, c <sup>-1</sup>	%
$^{235}\text{U}$	-	-	$(4.615 \pm 0.171) \cdot 10^{-13}$	3.70	$(5.771 \pm 0.208) \cdot 10^{-13}$	3.60	$(6.182 \pm 0.241) \cdot 10^{-13}$	3.90
$^{239}\text{Pu}$	-	-	$(8.547 \pm 0.316) \cdot 10^{-13}$	3.70	$(7.389 \pm 0.276) \cdot 10^{-13}$	3.74	$(9.089 \pm 0.336) \cdot 10^{-13}$	3.70
$^{237}\text{Np}$	-	-	$(3.728 \pm 0.160) \cdot 10^{-16}$	4.30	-	-	-	-
$^{238}\text{Pu}$	-	-	$(1.869 \pm 0.094) \cdot 10^{-14}$	5.02	-	-	-	-
$^{240}\text{Pu}$	-	-	$(3.937 \pm 0.165) \cdot 10^{-15}$	4.20	-	-	-	-
$^{241}\text{Pu}$	-	-	$(8.348 \pm 0.386) \cdot 10^{-13}$	4.63	-	-	-	-
$^{242\text{m}}\text{Am}$	-	-	$(6.543 \pm 0.353) \cdot 10^{-12}$	5.40	-	-	-	-
$^{243}\text{Cm}$	-	-	$(7.000 \pm 0.335) \cdot 10^{-13}$	4.78	-	-	-	-
$^{245}\text{Cm}$	-	-	$(1.397 \pm 0.075) \cdot 10^{-12}$	5.40	-	-	-	-
$^{247}\text{Cm}$	-	-	$(2.714 \pm 0.169) \cdot 10^{-13}$	6.22	-	-	-	-

## 12. Determination of neutron spectra in the SBM channels

The experimental data of Tables 22 and 23 were used to unfold the neutron spectra in the SBM channels, wherein the measurements were made for lattices 21-1-5(M2) and 21-2.

The neutron energy spectra in the 0-mm, 46.5-mm, 72.0-mm, and 96.5-mm SBM channels in fuel lattice 21-1-5(M2) and in the 46.5-mm, 72.0-mm, and 96.5-mm SBM channels in fuel lattice 21-2 were unfolded by the KASKAD code that describes the neutron spectrum as

$$\begin{aligned}
\phi(E) = & A_F \cdot \left(2 \cdot \alpha_F^{3/2} / \sqrt{\pi}\right) \cdot \sqrt{E} \cdot \exp(-\alpha_F \cdot E) + A_H^1 \cdot (\alpha_H^1)^2 \cdot E \cdot \exp(-\alpha_H^1 \cdot E) + \\
& + A_H^n \cdot (\alpha_H^n)^2 \cdot E \cdot \exp(-\alpha_H^n \cdot E) + A_M \cdot \alpha_M^2 \cdot E \cdot \exp(-\alpha_M^2 \cdot E) + \\
& + A_\Phi \cdot (1/E^{\alpha_\Phi}) \cdot \left[1 + (10^7/E)^7\right]^{-1} \cdot \left[1 + (E/0.2)^2\right]^{-1}
\end{aligned}
\tag{38}$$

where  $\phi(E)$  is unit neutron fluence;  $E$  is neutron energy in MeV; the subscripts F, H, M, and  $\Phi$  are different neutron spectrum components from, respectively,  $^{235}\text{U}$  fission neutrons (F), inelastic neutron scattering on nuclei of the MAKET core structure materials (H), elastic neutron scattering on the deuterium and hydrogen nuclei of the moderator (heavy water) (M), and stopped neutrons in the form of the Fermi spectrum( $\Phi$ ).

The error in determining the emery spectrum for the SBM channels has been found at a 0.95 confidence level to be 3-6% for thermal neutrons, 15% for <150 keV neutrons, 3-10% for 0.15-10 MeV neutrons, and 10-15% for 10-18 MeV neutrons.

Table 29 presents the values of constants  $\alpha$  and  $A$  used in formula (38) to describe the neutron energy spectra in the SBM channels.

Table 29. The values of constants  $\alpha$  and  $A$ .

Position of a channel, mm	Neutron fluence, $10^9$	Neutron energy in the spectrum, MeV	Spectral components			
			$\alpha_F (A_F)$	$\alpha_H (A_H)$	$\alpha_M (A_M), \cdot 10^7$	$\alpha_\Phi (A_\Phi)$
Lattice 21-1-5(M2)						
0	2.27	0.0904	0.788(3.45)	5.000(3.61)	3.368(45.8)	1.000(3.28)
46.5	2.49	0.1135	0.705(2.71)	5.000(11.6)	3.296(41.8)	1.000(3.05)
72	2.42	0.1051	0.766(3.60)	5.000(5.79)	3.430(45.1)	0.980(3.76)
96.5	2.48	0.111	0.766(4.26)	5.000(4.32)	3.275(43.6)	1.000(3.32)
Lattice 21-2						
46.5	2.61	0.1364	0.795(5.67)	5.000(4.68)	3.180(40.3)	1.000(3.43)
72	2.36	0.1745	0.808(7.92)	5.000(4.01)	3.130(38.6)	0.990(3.75)
96.5	2.23	0.1331	0.802(6.24)	5.000(1.45)	3.125(43.6)	1.000(3.38)

Fig. 21 shows the neutron spectra unfolded from experimental data by KASKAD code. Fig. 22 shows the neutron spectra simulated by the MCNB-4B code.

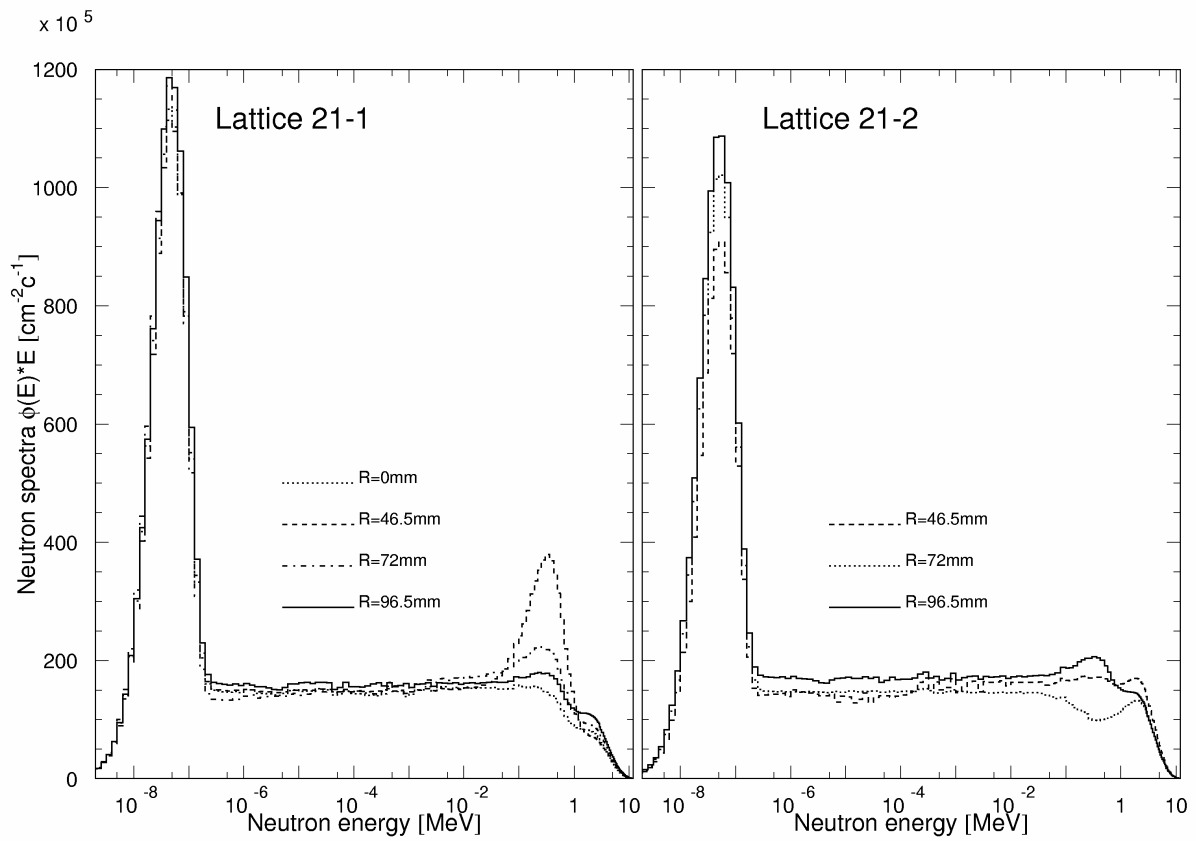


Fig. 21. The SBM channel neutron spectra unfolded from experimental data by the KASKAD code.

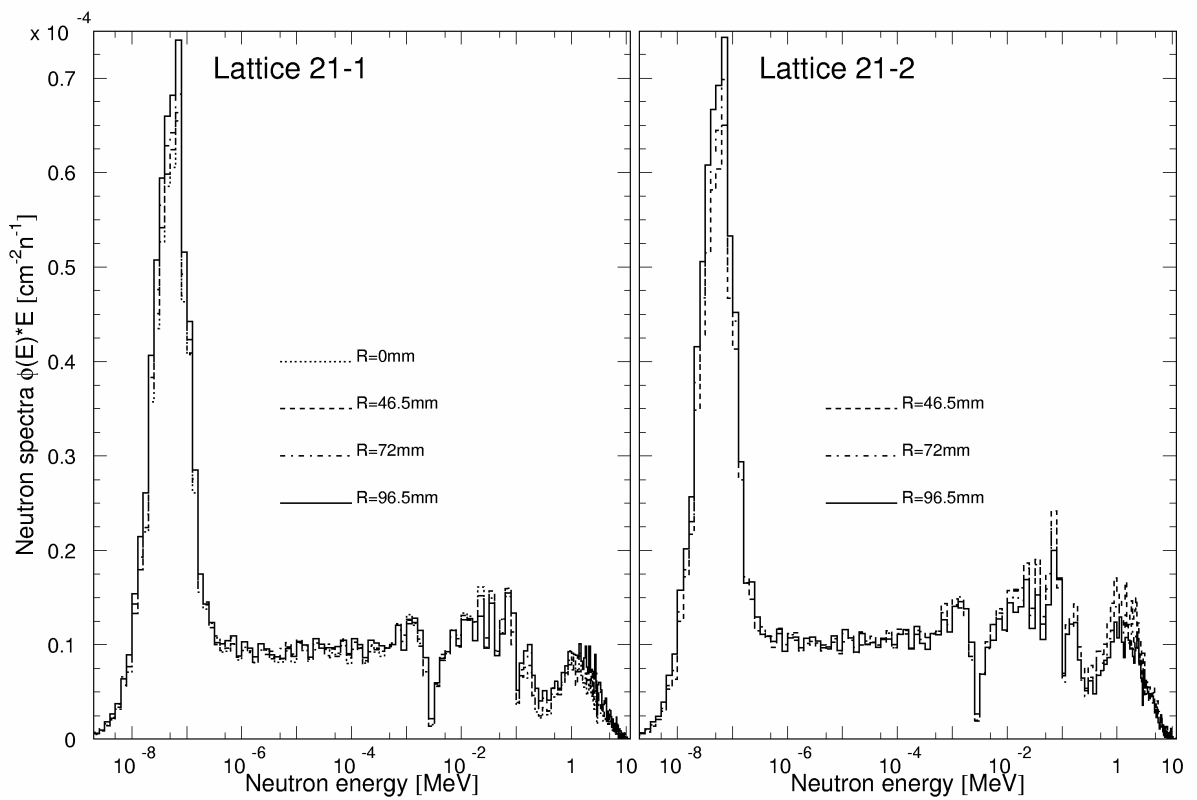


Fig. 22. The SBM channel neutron spectra simulated by the MCNP-4B code.

### 13. The computational model of the MAKET facility; the calculation results

The MCNP-4B code was used to calculate the MAKET critical states and the reaction rates for experimental samples in the SBM channels [8]. Pending the calculations, two simulation models (the MCNP-4B input files) were constructed, namely, B21-1-5(M2) (the salt insert in the central fuel channel) and B21-2 (fuel elements in the central fuel channel).

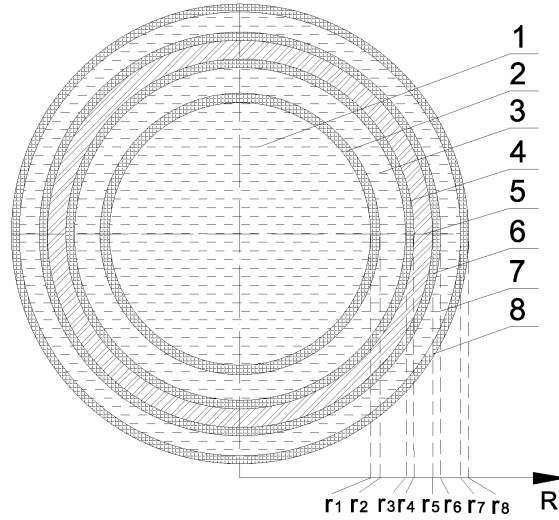


Fig. 23. Simulation model of fuel element

The models give the detailed three-dimensional descriptions of the MAKET facility and SBM, including two cylindrical tanks, and the upper and lower supporting lattices. The fuel channels are of the complicated structure of a set of stacked ring-shaped fuel elements) with the fissile material of a 1268-mm total length. In the simulation models, the fuel elements were represented by a set of the height-uniform cylinders (zones), whose cross sections are presented in Table 30.

Table 30. Dimensions and composition of the fuel element zones.

Layer Nos.	Composition	Internal radius, mm	External radius, mm
1	D <sub>2</sub> O	0	17
2	Al	17	18
3	D <sub>2</sub> O	18	21.4
4	Al	21.4	22.4
5	UO <sub>2</sub> + Al	22.4	24
6	Al	24	25
7	D <sub>2</sub> O	25	28.8
8	Al	28.8	30

The simulation model allowed also for the design of the fuel channel bottom (see Fig. 24). Since the uranium mass is alike in all the fuel elements (see Table 42), the total uranium mass in the fuel channels was distributed uniformly over the total length of the fuel elements in the channels.

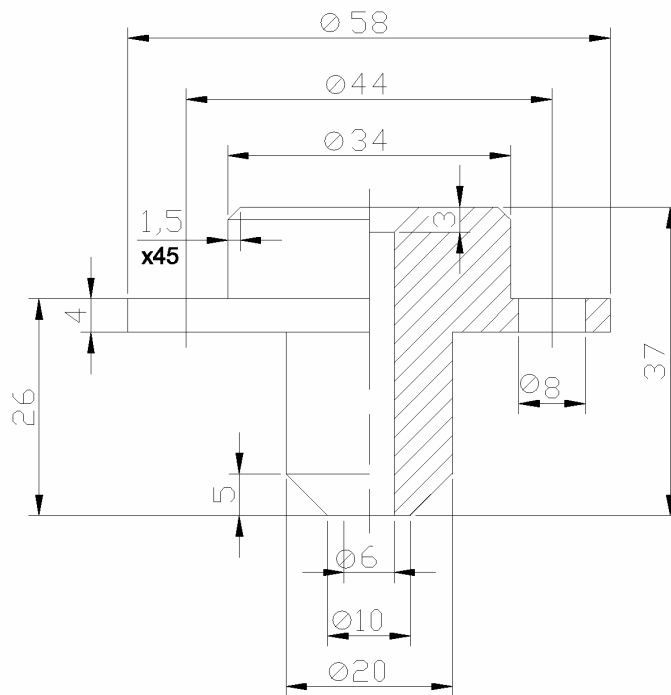


Fig. 24. Drawing of the fuel channel bottom.

The SBM was described in strict conformity with the set of drawings; all the actual dimensions, gaps, etc., were allowed for. In the SBM description, the physical approximation (a simplified representation of a given object geometry that avoids introducing any strong distortion in the MAKET facility neutron-physics characteristics) was only used for the SBM upper part above the heavy water level and for minor pieces (bolts, for instance). In the actual experiments, the central axis of the MAKET critical facility assembly (with the SBM axis established) did not coincide with the central axis of the tank. The relevant analysis and calculations have shown that the displacement of the critical facility to the tank center does not affect the calculation results. In the simulation models, therefore, the SBM was placed at the center of the heavy water tank.

Figs. 25 and 26 show the horizontal and vertical sections of the simulation model for lattice 21-1-5(M2).

The critical heavy water lattices are known to be sensitive to the light water content of heavy water, and to the impurities in the latter and in the structure materials. The impact of the impurities in heavy water and in the SBM salt on  $K_{\text{eff}}$  was computer-analyzed. To simplify the model, the overall composition of the heavy water impurities was replaced with the  $^{10}\text{B}$  isotope of a  $5 \cdot 10^{15}$  nucleus/cm<sup>3</sup> nuclear concentration. As a result,  $K_{\text{eff}}$  has proved to be the same when the calculations were made for the overall impurity composition and for  $^{10}\text{B}$  only. The SBM salt composition was also simplified, namely, the strongest two absorbers were taken to be as such (see Table 6, Mn -  $1.5 \cdot 10^{-4}$  % (weight) and Cu -  $8 \cdot 10^{-4}$  % (weight)), whereas all the rest impurities were replaced with  $6.5 \cdot 10^{-3}$  % (weight) of V. The impurity content of the Zr alloy was taken to conform to Table 3.

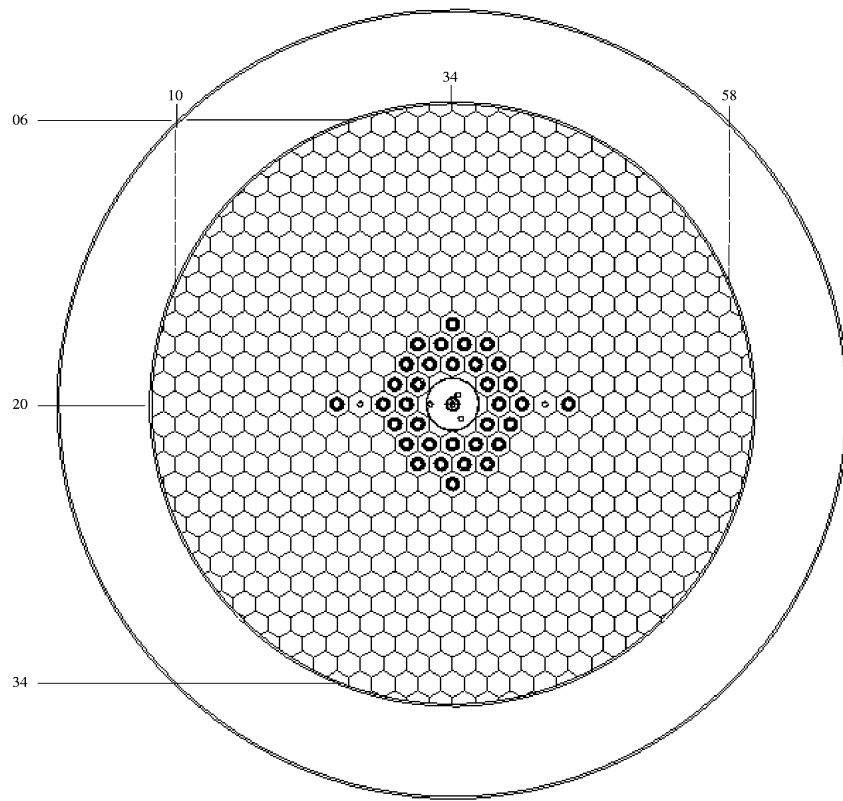


Fig. 25. The horizontal section of the simulation model for lattice 21-1-5(M2).

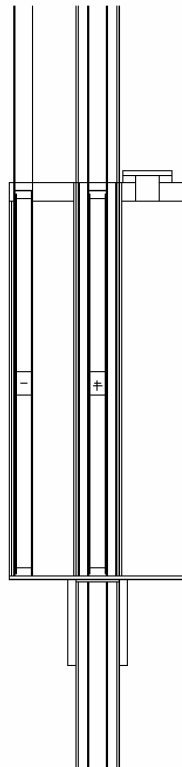


Fig. 26. The vertical section of the simulation model for lattice 21-1-5(M2).

To support the calculations, a neutron cross section library was compiled basing of the ENDF/B-VI rev.7 [9] and JENDL-3.2 [10] files of estimated nuclear data. All the neutron cross sections are presented in continuous form within a 0.1% accuracy of restoring the cross sections in the range of unresolved resonances. Use was also made of the ML45 code designed by the present authors basing on the NJOY-94(99) code [11, 12]. The thermal scattering matrix  $S_{a,b}$  was constructed for deuterium and hydrogen to suit the experimental heavy and light water temperatures, respectively. The method for preparing the neutron cross sections was verified by calculating the critical tests [13] and the actual experiments.

Thus, the simulation models reproduced the real three-dimensional geometry of the MAKET facility and SBM and described the isotopic composition of their structure materials as plausibly as possible. The correctness of constructing the models and the neutron cross section libraries has been verified by calculating the critical states of the MAKET facility with the SBM. Table 7 presents the parameters of the critical states and the calculation results. Fig. 3 shows the cartograms of the critical states. Calculations of each of the critical states took about 2-3 days of machine time, which corresponded to 10-15 million neutron histories. Table 7 shows a good agreement of the above two simulation models in determining the critical state, despite a minor overestimation of the calculation results, which arose probably from the errors in determining the heavy water impurity composition and, maybe, from other uncertainties.

The reaction rates were calculated for the experimental samples in their containers. The tentative analysis and calculations have made it possible to describe and calculate the real geometry and mass of the experimental samples for  $^{nat}\text{In}$  and  $^{238}\text{U}$  only, thus allowing for the self-blocking effects. For all the rest samples, the reaction rates were detected in terms of a single calculation run in a homogeneous region that describes the detector locations. Calculations of each version took about a week of machine time, which corresponds to 50-60 million neutron histories.

The MCNP-4B output consists of the calculated reaction rate values normalized to the fission neutron number  $[1/n]$ , where  $n$  designates a fission neutron. To facilitate the experiment-calculation comparisons, the code output data were reduced to dimension  $[1/(g \cdot W \cdot s)]$ . The normalization factor was calculated as

$$K = \frac{1}{E_f \cdot \Sigma_f} \cdot \frac{N_{Av}}{A} \quad (39)$$

where  $E_f$  is energy deposition in a single fission event (conforming to the code output,  $E_f=194.0833$  MeV);

$\Sigma_f$  is the total number of fission events normalized to a single fission neutron (the  $\Sigma_f$  value is taken from the code output);

$N_{Av}$  is the Avogadro number ( $6.023 \cdot 10^{23} \text{ mol}^{-1}$ );

$A$  is the atomic mass of nuclide.



Table 31. The calculated reaction rate values (1/(g·W·s)) in lattice 21-1-5(M2) (ENDF/B-VI rev.7).

Reaction	Position of experimental sample, mm			
	0	46.5	72	96.5
	$R_{\text{calc}} \pm \Delta R_{\text{calc}}$	$R_{\text{calc}} \pm \Delta R_{\text{calc}}$	$R_{\text{calc}} \pm \Delta R_{\text{calc}}$	$R_{\text{calc}} \pm \Delta R_{\text{calc}}$
$^{235}\text{U}(n,f)$	$(1.327 \pm 0.003) \cdot 10^7$	$(1.365 \pm 0.003) \cdot 10^7$	$(1.436 \pm 0.004) \cdot 10^7$	$(1.532 \pm 0.005) \cdot 10^7$
$^{238}\text{U}(n,f)$	$(6.579 \pm 0.068) \cdot 10^4$	$(6.803 \pm 0.078) \cdot 10^4$	$(7.102 \pm 0.082) \cdot 10^4$	$(7.592 \pm 0.104) \cdot 10^4$
$^{238}\text{U}(n,\gamma)$	$(2.440 \pm 0.149) \cdot 10^5$	$(2.451 \pm 0.138) \cdot 10^5$	$(2.715 \pm 0.172) \cdot 10^5$	$(2.616 \pm 0.169) \cdot 10^5$
$^{55}\text{Mn}(n,\gamma)$	$(1.398 \pm 0.003) \cdot 10^6$	$(1.436 \pm 0.004) \cdot 10^6$	$(1.507 \pm 0.004) \cdot 10^6$	$(1.607 \pm 0.005) \cdot 10^6$
$^{63}\text{Cu}(n,\gamma)$	$(4.145 \pm 0.014) \cdot 10^5$	$(4.276 \pm 0.016) \cdot 10^5$	$(4.501 \pm 0.019) \cdot 10^5$	$(4.768 \pm 0.020) \cdot 10^5$
$^{197}\text{Au}(n,\gamma)$	$(6.456 \pm 0.010) \cdot 10^6$	$(6.621 \pm 0.099) \cdot 10^6$	$(6.861 \pm 0.106) \cdot 10^6$	$(6.954 \pm 0.115) \cdot 10^6$
$^{176}\text{Lu}(n,\gamma)$	$(1.337 \pm 0.004) \cdot 10^8$	$(1.374 \pm 0.004) \cdot 10^8$	$(1.433 \pm 0.004) \cdot 10^8$	$(1.514 \pm 0.005) \cdot 10^8$
$^{27}\text{Al}(n,\alpha)$	$10.31 \pm 0.98$	$13.72 \pm 1.35$	$16.61 \pm 1.80$	$17.68 \pm 1.77$
$^{115}\text{In}(n,n')$	$(6.831 \pm 0.106) \cdot 10^2$	$(7.170 \pm 0.107) \cdot 10^2$	$(8.566 \pm 0.125) \cdot 10^2$	$(8.546 \pm 0.142) \cdot 10^2$
$^{113}\text{In}(n,\gamma)$	$(1.220 \pm 0.110) \cdot 10^6$	$(1.223 \pm 0.101) \cdot 10^6$	$(1.377 \pm 0.145) \cdot 10^6$	$(1.212 \pm 0.084) \cdot 10^6$
$^{115}\text{In}(n,\gamma)$	$(9.659 \pm 0.291) \cdot 10^6$	$(9.838 \pm 0.274) \cdot 10^6$	$(1.001 \pm 0.027) \cdot 10^7$	$(1.060 \pm 0.033) \cdot 10^7$
$^{237}\text{Np}(n,f)$	$(4.317 \pm 0.068) \cdot 10^3$	$(4.707 \pm 0.074) \cdot 10^3$	$(5.102 \pm 0.085) \cdot 10^3$	$(5.603 \pm 0.105) \cdot 10^3$
$^{238}\text{Pu}(n,f)$	$(3.931 \pm 0.022) \cdot 10^5$	$(4.042 \pm 0.023) \cdot 10^5$	$(4.290 \pm 0.026) \cdot 10^5$	$(4.568 \pm 0.032) \cdot 10^5$
$^{239}\text{Pu}(n,f)$	$(2.131 \pm 0.012) \cdot 10^7$	$(2.183 \pm 0.012) \cdot 10^7$	$(2.324 \pm 0.014) \cdot 10^7$	$(2.437 \pm 0.017) \cdot 10^7$
$^{240}\text{Pu}(n,f)$	$(1.033 \pm 0.020) \cdot 10^2$	$(1.118 \pm 0.021) \cdot 10^4$	$(1.161 \pm 0.022) \cdot 10^4$	$(1.265 \pm 0.028) \cdot 10^4$
$^{241}\text{Pu}(n,f)$	$(2.593 \pm 0.013) \cdot 10^7$	$(2.659 \pm 0.014) \cdot 10^7$	$(2.825 \pm 0.015) \cdot 10^7$	$(2.986 \pm 0.019) \cdot 10^7$
$^{242m}\text{Am}(n,f)$	$(1.639 \pm 0.008) \cdot 10^8$	$(1.681 \pm 0.009) \cdot 10^8$	$(1.787 \pm 0.009) \cdot 10^8$	$(1.896 \pm 0.012) \cdot 10^8$
$^{243}\text{Cm}(n,f)$	$(1.889 \pm 0.009) \cdot 10^7$	$(1.948 \pm 0.010) \cdot 10^7$	$(2.059 \pm 0.011) \cdot 10^7$	$(2.169 \pm 0.013) \cdot 10^7$
$^{245}\text{Cm}(n,f)$	$(4.488 \pm 0.024) \cdot 10^7$	$(4.634 \pm 0.025) \cdot 10^7$	$(4.919 \pm 0.029) \cdot 10^7$	$(5.254 \pm 0.037) \cdot 10^7$
$^{247}\text{Cm}(n,f)$	$(3.341 \pm 0.041) \cdot 10^6$	$(3.373 \pm 0.042) \cdot 10^6$	$(3.525 \pm 0.044) \cdot 10^6$	$(3.831 \pm 0.056) \cdot 10^6$

Table 32. The calculated reaction rate values (1/(g·W·s)) in lattice 21-1-5(M2) (JENDL-3.2).

Reaction	Position of experimental sample, mm			
	0	46.5	72	96.5
	$R_{\text{calc}} \pm \Delta R_{\text{calc}}$	$R_{\text{calc}} \pm \Delta R_{\text{calc}}$	$R_{\text{calc}} \pm \Delta R_{\text{calc}}$	$R_{\text{calc}} \pm \Delta R_{\text{calc}}$
$^{235}\text{U}(n,f)$	$(1.336 \pm 0.007) \cdot 10^7$	$(1.378 \pm 0.007) \cdot 10^7$	$(1.436 \pm 0.008) \cdot 10^7$	$(1.532 \pm 0.010) \cdot 10^7$
$^{238}\text{U}(n,f)$	$(6.666 \pm 0.071) \cdot 10^4$	$(6.748 \pm 0.066) \cdot 10^4$	$(7.117 \pm 0.076) \cdot 10^4$	$(7.660 \pm 0.124) \cdot 10^4$
$^{238}\text{U}(n,\gamma)$	$(2.555 \pm 0.165) \cdot 10^5$	$(2.445 \pm 0.163) \cdot 10^5$	$(2.793 \pm 0.173) \cdot 10^5$	$(2.908 \pm 0.199) \cdot 10^5$
$^{55}\text{Mn}(n,\gamma)$	$(1.401 \pm 0.007) \cdot 10^6$	$(1.443 \pm 0.007) \cdot 10^6$	$(1.501 \pm 0.008) \cdot 10^6$	$(1.601 \pm 0.001) \cdot 10^6$
$^{63}\text{Cu}(n,\gamma)$	$(4.156 \pm 0.030) \cdot 10^5$	$(4.358 \pm 0.040) \cdot 10^5$	$(4.470 \pm 0.038) \cdot 10^5$	$(4.747 \pm 0.039) \cdot 10^5$
$^{197}\text{Au}(n,\gamma)$	$(6.027 \pm 0.161) \cdot 10^6$	$(6.669 \pm 0.191) \cdot 10^6$	$(6.771 \pm 0.203) \cdot 10^6$	$(6.882 \pm 0.212) \cdot 10^6$
$^{115}\text{In}(n,n')$	$(6.818 \pm 0.604) \cdot 10^1$	$(8.154 \pm 0.973) \cdot 10^1$	$(7.791 \pm 0.655) \cdot 10^1$	$(8.233 \pm 0.689) \cdot 10^1$
$^{115}\text{In}(n,2n)$	$8.359 \pm 4.771$	$12.31 \pm 6.82$	$9.022 \pm 6.839$	$2.394 \pm 1.508$
$^{115}\text{In}(n,\gamma)$	$(8.638 \pm 0.201) \cdot 10^6$	$(9.037 \pm 0.211) \cdot 10^6$	$(9.468 \pm 0.215) \cdot 10^6$	$(1.021 \pm 0.0275) \cdot 10^7$
$^{113}\text{In}(n,\gamma)$	$(1.482 \pm 0.125) \cdot 10^6$	$(1.514 \pm 0.120) \cdot 10^6$	$(1.653 \pm 0.155) \cdot 10^6$	$(1.542 \pm 0.108) \cdot 10^6$
$^{27}\text{Al}(n,\alpha)$	$12.48 \pm 2.66$	$14.67 \pm 3.36$	$16.84 \pm 4.41$	$16.17 \pm 2.66$
$^{64}\text{Zn}(n,p)$	$(2.545 \pm 0.106) \cdot 10^2$	$(3.239 \pm 0.135) \cdot 10^2$	$(3.830 \pm 0.166) \cdot 10^2$	$(4.336 \pm 0.201) \cdot 10^2$
$^{64}\text{Zn}(n,\gamma)$	$(7.377 \pm 0.059) \cdot 10^4$	$(7.599 \pm 0.0654) \cdot 10^4$	$(7.824 \pm 0.0587) \cdot 10^4$	$(8.298 \pm 0.069) \cdot 10^4$
$^{237}\text{Np}(n,f)$	$(5.996 \pm 0.074) \cdot 10^3$	$(6.223 \pm 0.0765) \cdot 10^3$	$(6.932 \pm 0.086) \cdot 10^3$	$(7.191 \pm 0.104) \cdot 10^3$
$^{238}\text{Pu}(n,f)$	$(4.150 \pm 0.019) \cdot 10^5$	$(4.313 \pm 0.021) \cdot 10^5$	$(4.486 \pm 0.022) \cdot 10^5$	$(4.811 \pm 0.031) \cdot 10^5$
$^{239}\text{Pu}(n,f)$	$(2.131 \pm 0.009) \cdot 10^7$	$(2.189 \pm 0.010) \cdot 10^7$	$(2.294 \pm 0.011) \cdot 10^7$	$(2.433 \pm 0.013) \cdot 10^7$
$^{240}\text{Pu}(n,f)$	$(1.011 \pm 0.015) \cdot 10^4$	$(1.087 \pm 0.017) \cdot 10^4$	$(1.145 \pm 0.017) \cdot 10^4$	$(1.165 \pm 0.019) \cdot 10^4$
$^{241}\text{Pu}(n,f)$	$(2.590 \pm 0.010) \cdot 10^7$	$(2.669 \pm 0.011) \cdot 10^7$	$(2.799 \pm 0.012) \cdot 10^7$	$(2.974 \pm 0.015) \cdot 10^7$
$^{242m}\text{Am}(n,f)$	$(1.636 \pm 0.007) \cdot 10^8$	$(1.688 \pm 0.007) \cdot 10^8$	$(1.771 \pm 0.008) \cdot 10^8$	$(1.885 \pm 0.009) \cdot 10^8$
$^{243}\text{Cm}(n,f)$	$(1.665 \pm 0.007) \cdot 10^7$	$(1.707 \pm 0.007) \cdot 10^7$	$(1.785 \pm 0.007) \cdot 10^7$	$(1.892 \pm 0.009) \cdot 10^7$
$^{245}\text{Cm}(n,f)$	$(3.994 \pm 0.018) \cdot 10^7$	$(4.122 \pm 0.019) \cdot 10^7$	$(4.337 \pm 0.021) \cdot 10^7$	$(4.637 \pm 0.026) \cdot 10^7$
$^{247}\text{Cm}(n,f)$	$(2.863 \pm 0.026) \cdot 10^6$	$(2.908 \pm 0.027) \cdot 10^6$	$(3.008 \pm 0.027) \cdot 10^6$	$(3.149 \pm 0.032) \cdot 10^6$

Table 33. The calculated reaction rate values (1/(g·W·s)) in lattice 21-2 (ENDF/B-VI rev.7).

Reaction	Position of experimental sample, mm		
	46.5	72	96.5
	$R_{\text{calc}} \pm \Delta R_{\text{calc}}$	$R_{\text{calc}} \pm \Delta R_{\text{calc}}$	$R_{\text{calc}} \pm \Delta R_{\text{calc}}$
$^{235}\text{U}(n,f)$	$(1.321 \pm 0.004) \cdot 10^7$	$(1.435 \pm 0.004) \cdot 10^7$	$(1.551 \pm 0.005) \cdot 10^7$
$^{238}\text{U}(n,f)$	$(6.553 \pm 0.076) \cdot 10^4$	$(7.216 \pm 0.095) \cdot 10^4$	$(7.527 \pm 0.108) \cdot 10^4$
$^{238}\text{U}(n,\gamma)$	$(2.607 \pm 0.150) \cdot 10^5$	$(2.804 \pm 0.182) \cdot 10^5$	$(2.630 \pm 0.188) \cdot 10^5$
$^{55}\text{Mn}(n,\gamma)$	$(1.399 \pm 0.004) \cdot 10^6$	$(1.514 \pm 0.004) \cdot 10^6$	$(1.632 \pm 0.005) \cdot 10^6$
$^{63}\text{Cu}(n,\gamma)$	$(4.169 \pm 0.017) \cdot 10^5$	$(4.535 \pm 0.019) \cdot 10^5$	$(4.865 \pm 0.023) \cdot 10^5$
$^{197}\text{Au}(n,\gamma)$	$(6.869 \pm 0.115) \cdot 10^6$	$(7.050 \pm 0.108) \cdot 10^6$	$(7.386 \pm 0.140) \cdot 10^6$
$^{176}\text{Lu}(n,\gamma)$	$(1.359 \pm 0.004) \cdot 10^8$	$(1.454 \pm 0.005) \cdot 10^8$	$(1.553 \pm 0.006) \cdot 10^8$
$^{27}\text{Al}(n,\alpha)$	$22.46 \pm 2.31$	$17.81 \pm 1.54$	$19.29 \pm 1.88$
$^{115}\text{In}(n,n')$	$(1.366 \pm 0.019) \cdot 10^3$	$(1.539 \pm 0.021) \cdot 10^3$	$(1.580 \pm 0.026) \cdot 10^3$
$^{115}\text{In}(n,\gamma)$	$(9.274 \pm 0.281) \cdot 10^6$	$(1.055 \pm 0.036) \cdot 10^7$	$(1.095 \pm 0.039) \cdot 10^7$
$^{113}\text{In}(n,\gamma)$	$(1.347 \pm 0.110) \cdot 10^6$	$(1.340 \pm 0.091) \cdot 10^6$	$(1.599 \pm 0.175) \cdot 10^6$
$^{237}\text{Np}(n,f)$	$(8.759 \pm 0.168) \cdot 10^3$	$(7.473 \pm 0.144) \cdot 10^3$	$(6.852 \pm 0.141) \cdot 10^3$
$^{238}\text{Pu}(n,f)$	$(4.013 \pm 0.029) \cdot 10^5$	$(4.354 \pm 0.029) \cdot 10^5$	$(4.643 \pm 0.039) \cdot 10^5$
$^{239}\text{Pu}(n,f)$	$(2.143 \pm 0.015) \cdot 10^7$	$(2.326 \pm 0.016) \cdot 10^7$	$(2.457 \pm 0.019) \cdot 10^7$
$^{240}\text{Pu}(n,f)$	$(1.607 \pm 0.029) \cdot 10^4$	$(1.496 \pm 0.030) \cdot 10^4$	$(1.398 \pm 0.031) \cdot 10^4$
$^{241}\text{Pu}(n,f)$	$(2.573 \pm 0.015) \cdot 10^7$	$(2.819 \pm 0.017) \cdot 10^7$	$(3.004 \pm 0.022) \cdot 10^7$
$^{242\text{m}}\text{Am}(n,f)$	$(1.618 \pm 0.009) \cdot 10^8$	$(1.775 \pm 0.011) \cdot 10^8$	$(1.901 \pm 0.014) \cdot 10^8$
$^{243}\text{Cm}(n,f)$	$(1.906 \pm 0.011) \cdot 10^7$	$(2.064 \pm 0.012) \cdot 10^7$	$(2.210 \pm 0.015) \cdot 10^7$
$^{245}\text{Cm}(n,f)$	$(4.392 \pm 0.028) \cdot 10^7$	$(4.889 \pm 0.033) \cdot 10^7$	$(5.264 \pm 0.042) \cdot 10^7$
$^{247}\text{Cm}(n,f)$	$(3.520 \pm 0.053) \cdot 10^6$	$(3.632 \pm 0.051) \cdot 10^6$	$(3.835 \pm 0.059) \cdot 10^6$

Table 34. The calculated reaction rate values ( $1/(\text{g} \cdot \text{W} \cdot \text{s})$ ) in lattice 21-2 (JENDL-3.2).

Reaction	Position of experimental sample, mm		
	46.5	72	96.5
	$R_{\text{calc}} \pm \Delta R_{\text{calc}}$	$R_{\text{calc}} \pm \Delta R_{\text{calc}}$	$R_{\text{calc}} \pm \Delta R_{\text{calc}}$
$^{235}\text{U}(n,f)$	$(1.324 \pm 0.004) \cdot 10^7$	$(1.438 \pm 0.004) \cdot 10^7$	$(1.554 \pm 0.005) \cdot 10^7$
$^{55}\text{Mn}(n,\gamma)$	$(1.398 \pm 0.004) \cdot 10^6$	$(1.513 \pm 0.004) \cdot 10^6$	$(1.631 \pm 0.005) \cdot 10^6$
$^{63}\text{Cu}(n,\gamma)$	$(4.166 \pm 0.017) \cdot 10^5$	$(4.532 \pm 0.019) \cdot 10^5$	$(4.861 \pm 0.023) \cdot 10^5$
$^{197}\text{Au}(n,\gamma)$	$(6.868 \pm 0.105) \cdot 10^6$	$(7.015 \pm 0.096) \cdot 10^6$	$(7.383 \pm 0.126) \cdot 10^6$
$^{115}\text{In}(n,n')$	$(1.471 \pm 0.015) \cdot 10^2$	$(1.259 \pm 0.013) \cdot 10^2$	$(1.3200.014) \cdot 10^4$
$^{115}\text{In}(n,2n)$	$8.009 \pm 2.715$	$4.070 \pm 1.485$	$4.266 \pm 1.445$
$^{115}\text{In}(n,\gamma)$	$(8.676 \pm 0.265) \cdot 10^6$	$(9.618 \pm 0.284) \cdot 10^6$	$(9.798 \pm 0.299) \cdot 10^6$
$^{113}\text{In}(n,\gamma)$	$(1.681 \pm 0.123) \cdot 10^6$	$(1.651 \pm 0.107) \cdot 10^6$	$(2.056 \pm 0.209) \cdot 10^6$
$^{27}\text{Al}(n,\alpha)$	$21.52 \pm 2.25$	$17.01 \pm 1.49$	$18.37 \pm 1.80$
$^{64}\text{Zn}(n,p)$	$(6.214 \pm 0.125) \cdot 10^2$	$(5.095 \pm 0.101) \cdot 10^2$	$(4.984 \pm 0.108) \cdot 10^4$
$^{64}\text{Zn}(n,\gamma)$	$(7.471 \pm 0.033) \cdot 10^4$	$(7.999 \pm 0.037) \cdot 10^4$	$(8.535 \pm 0.037) \cdot 10^4$
$^{237}\text{Np}(n,f)$	$(1.055 \pm 0.016) \cdot 10^4$	$(9.343 \pm 0.149) \cdot 10^3$	$(8.586 \pm 0.144) \cdot 10^3$
$^{238}\text{Pu}(n,f)$	$(4.176 \pm 0.025) \cdot 10^5$	$(4.579 \pm 0.028) \cdot 10^5$	$(4.879 \pm 0.036) \cdot 10^5$
$^{239}\text{Pu}(n,f)$	$(2.134 \pm 0.013) \cdot 10^7$	$(2.315 \pm 0.0149) \cdot 10^7$	$(2.467 \pm 0.017) \cdot 10^7$
$^{240}\text{Pu}(n,f)$	$(1.540 \pm 0.025) \cdot 10^4$	$(1.404 \pm 0.024) \cdot 10^4$	$(1.358 \pm 0.026) \cdot 10^4$
$^{241}\text{Pu}(n,f)$	$(2.566 \pm 0.013) \cdot 10^7$	$(2.807 \pm 0.015) \cdot 10^7$	$(3.014 \pm 0.018) \cdot 10^7$
$^{242\text{m}}\text{Am}(n,f)$	$(1.613 \pm 0.008) \cdot 10^8$	$(1.769 \pm 0.009) \cdot 10^8$	$(1.905 \pm 0.012) \cdot 10^8$
$^{243}\text{Cm}(n,f)$	$(1.662 \pm 0.008) \cdot 10^7$	$(1.801 \pm 0.009) \cdot 10^7$	$(1.938 \pm 0.012) \cdot 10^7$
$^{245}\text{Cm}(n,f)$	$(3.881 \pm 0.021) \cdot 10^7$	$(4.319 \pm 0.025) \cdot 10^7$	$(4.6850.033) \cdot 10^7$
$^{247}\text{Cm}(n,f)$	$(2.922 \pm 0.034) \cdot 10^6$	$(3.140 \pm 0.034) \cdot 10^6$	$(3.273 \pm 0.038) \cdot 10^6$

The renormalized calculation results are presented in Tables 31, 32 (lattice 21-1-5(M2)) and 33, 34 (lattice 21-2).

The ENDF/B-VI (rev. 7) library was used when calculating the reaction rates presented in Tables 31 and 33.

The JENDL-3.2 library was used when calculating the reaction rates presented in Tables 32 and 34.

The  $^{68}\text{Zn}$  radiative capture reaction rate is not presented for either lattices, for the given nuclide data are absent from the two libraries. The  $^{64}\text{Zn}$  data are absent from ENDF/B-IV (rev. 7), and the  $^{176}\text{Lu}$  data from JENDL-3.2.

Besides, with a view to experimental determining the MAKET facility power, the  $^{235}\text{U}$  fission rate and  $^{63}\text{Cu}$  radiative trapping rate were calculated in terms of two simulation models outside a fuel element and as averaged over the fuel. The calculation results were used then to calculate  $K_i^{fuel}$  when determining the MAKET facility power for both lattices and to compare between the experimental and calculated data (see Subsection 1.14 below).

#### 14. Comparison between the experimental and calculated reaction rates

All the experimental and calculated results (see Table 1) are presented in Figs. 27 and 28. The calculated results presented in the Figures account the isotopic admixtures in the samples obtained via  $\alpha$ -spectrometry (Table 26).

The unified normalization ( $1/(\text{g}\cdot\text{W}\cdot\text{s})$ ) was used in the comparison. To that end, the experimental reaction rates were renormalized:

$$R_{norm} = \frac{R_{x_0}^{A,B} \cdot N_{Av}}{A \cdot W} \quad (39)$$

where  $W$  is the MAKET facility absolute power that correspond to an experimental lattice (see table 15);

$N_{Av}$  is the Avogadro number;

$R_{x_0}^{A,B}$  is the measured reaction rate (see formula (16));

$A$  is the atomic weight of an element.

The simulation-experiment mean squared deviation factor presented in Figs. 27 and 28 and in Table 35 were calculated as

$$\langle F \rangle = 10^{\sqrt{\langle (\log(R_{cal,i}/R_{exp,i}))^2 \rangle}} \quad (40)$$

where  $\langle \rangle$  means averaging over all the experimental and calculated data used in the comparisons.

The data presented show that the experiment-calculation differences are ranging from 2% to 47%<sup>1</sup> for the reactions of the well-known cross sections. In the case of the actinide reactions, the experiment-calculation differences are ranging from ~1% to 72%.

<sup>1</sup> The  $^{115}\text{In}(n,2n)+^{113}\text{In}(n,\gamma)$  reaction was disregarded because the  $^{113}\text{In}(n,\gamma)$  reaction rate is  $\gg$  the  $^{115}\text{In}(n,2n)$  reaction rate.

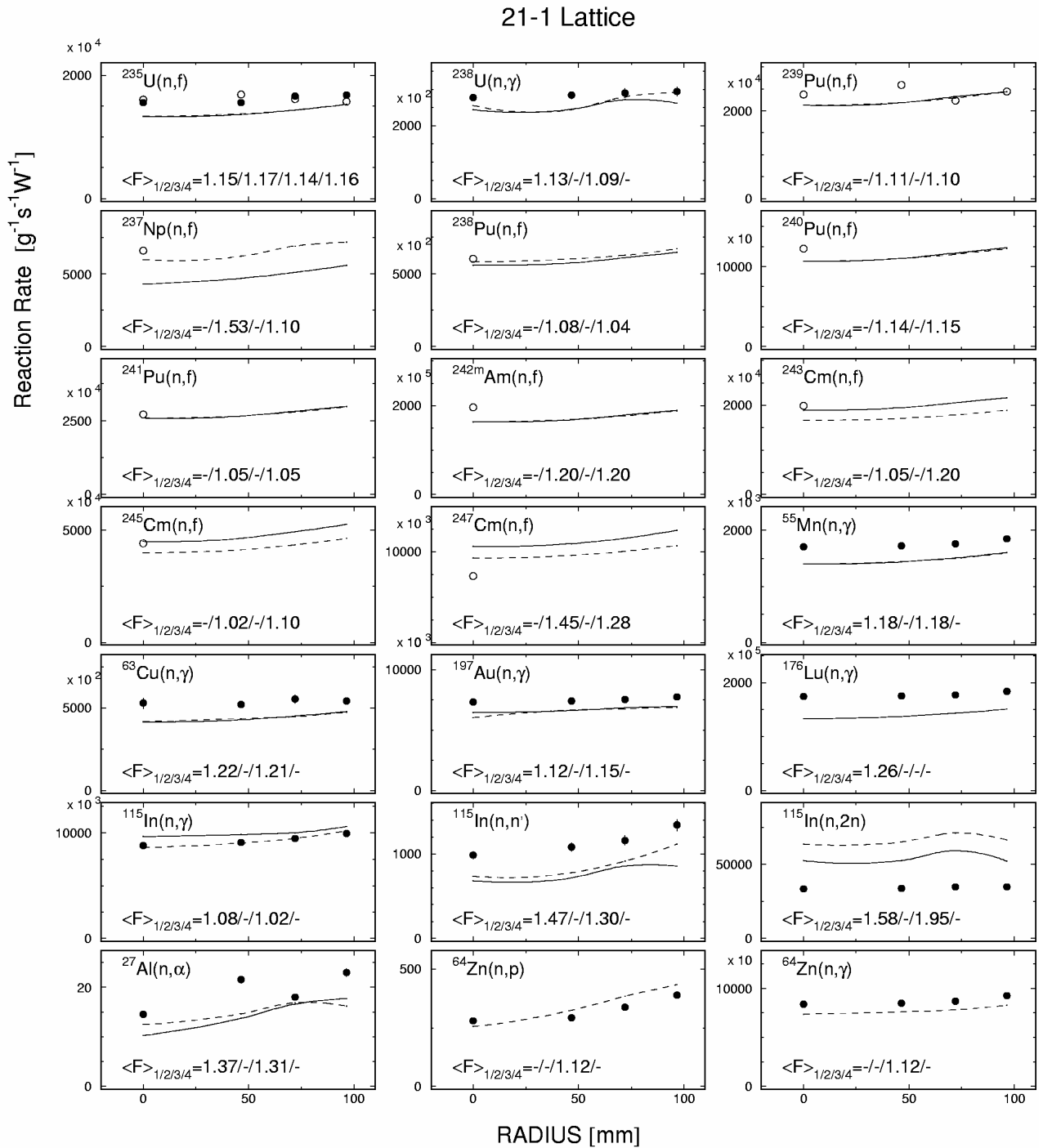


Fig. 27. The MAKET-measured and calculated reaction rates in the lattice with salt insert in central channel after normalizing to the  $^{235}\text{U}(n,f)$  reaction rate at the respective points. The black circles are the ITEP data. The light circles are the VNIIEF data. The dashed lines are the JENDL-3.2 –based calculations. The solid lines are the ENDF/B-IV–based calculations.  $\langle F \rangle_{1/2/3/4}$  are the experiment-calculation mean square deviation factors, where  $\langle F \rangle_1$  is the ITEP experiment- ENDF/B-VI calculation difference;  $\langle F \rangle_2$  is the VNIIEF experiment- ENDF/B-VI calculation difference;  $\langle F \rangle_3$  is the ITEP experiment- JENDL-3.2 calculation difference;  $\langle F \rangle_4$  is the VNIIEF experiment- JENDL-3.2 calculation difference. The gaps indicate lack of the appropriate experimental or calculated results.

## 21-2 Lattice

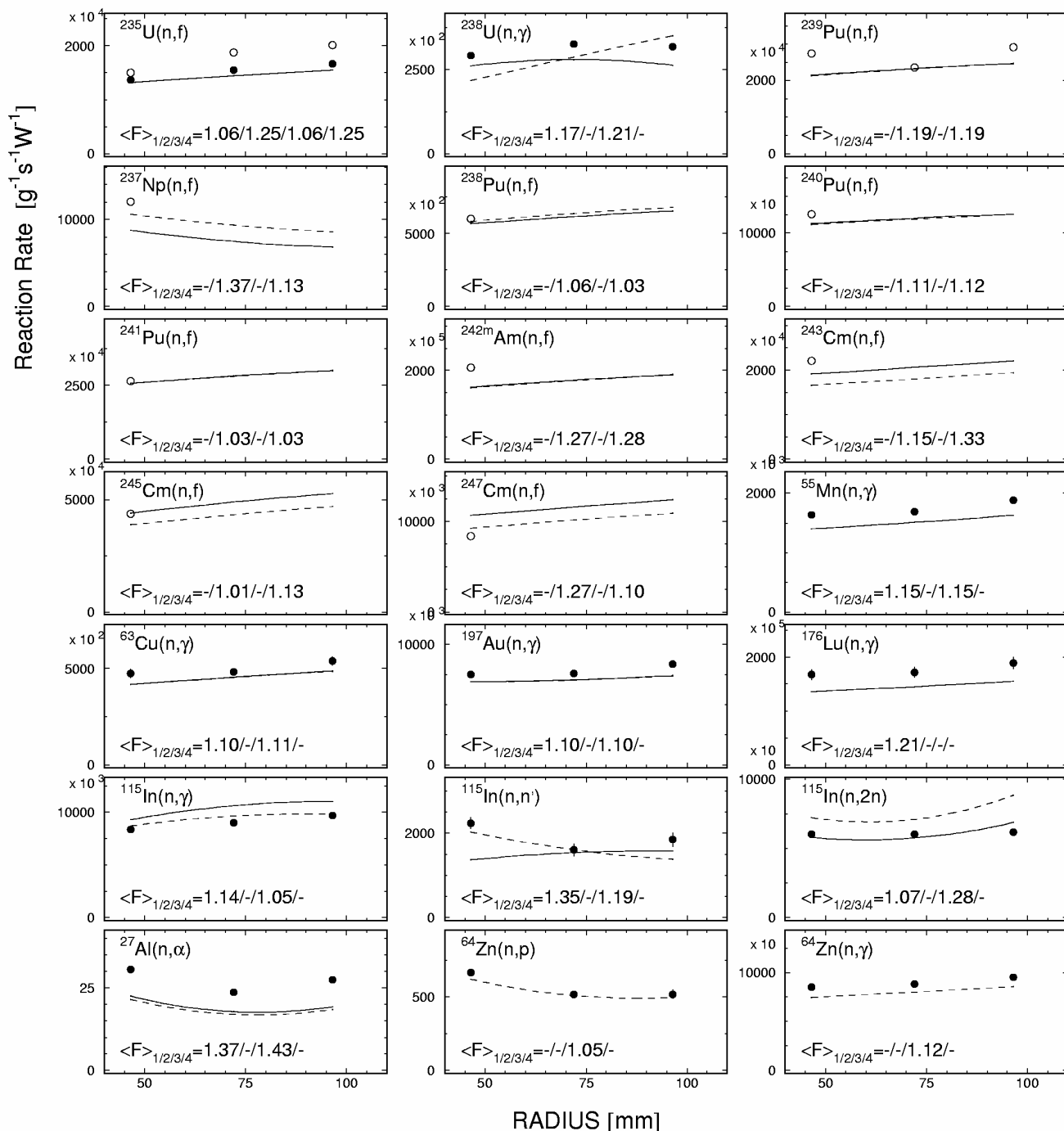


Fig. 28. The MAKET-measured and calculated reaction rates in the lattice with fuel elements in central channel after normalizing to the  $^{235}\text{U}(\text{n},\text{f})$  reaction rate at the respective points. The black circles are the ITEP data. The light circles are the VNIIEF data. The dashed lines are the JENDL-3.2 -based calculations. The solid lines are the ENDF/B-VI-based calculations.  $\langle F \rangle_{1/2/3/4}$  are the experiment-calculation mean square deviation factors, where  $\langle F \rangle_1$  is the ITEP experiment- ENDF/B-VI calculation difference;  $\langle F \rangle_2$  is the VNIIEF experiment- ENDF/B-VI calculation difference;  $\langle F \rangle_3$  is the ITEP experiment- JENDL-3.2 calculation difference;  $\langle F \rangle_4$  is the VNIIEF experiment- JENDL-3.2 calculation difference. The gaps indicate lack of the appropriate experimental or calculated results.

Table 35. The calculation-experiment mean squared deviation factors.

Reaction	ENDF/B-VI rev 7.				JENDL-3.2			
	21-1-1-5(M2)		21-2		21-1-1-5(M2)		21-2	
	ITEP	VNIIEF	ITEP	VNIIEF	ITEP	VNIIEF	ITEP	VNIIEF
$^{235}\text{U}(n,f)$	1.15	1.17	1.06	1.25	1.14	1.16	1.06	1.25
$^{238}\text{U}(n,\gamma)$	1.13	-	1.17	-	1.09	-	1.21	-
$^{239}\text{Pu}(n,f)$	-	1.11	-	1.19	-	1.10	-	1.19
$^{237}\text{Np}(n,f)$	-	1.53	-	1.37	-	1.10	-	1.13
$^{238}\text{Pu}(n,f)$	-	1.08	-	1.06	-	1.04	-	1.03
$^{240}\text{Pu}(n,f)$	-	1.14	-	1.11	-	1.15	-	1.12
$^{241}\text{Pu}(n,f)$	-	1.05	-	1.03	-	1.05	-	1.03
$^{242m}\text{Am}(n,f)$	-	1.20	-	1.27	-	1.20	-	1.28
$^{243}\text{Cm}(n,f)$	-	1.05	-	1.15	-	1.20	-	1.33
$^{245}\text{Cm}(n,f)$	-	1.02	-	1.01	-	1.10	-	1.13
$^{247}\text{Cm}(n,f)$	-	1.45	-	1.27	-	1.28	-	1.10
$^{55}\text{Mn}(n,\gamma)$	1.18	-	1.15	-	1.18	-	1.15	-
$^{63}\text{Cu}(n,\gamma)$	1.22	-	1.10	-	1.21	-	1.11	-
$^{197}\text{Au}(n,\gamma)$	1.12	-	1.10	-	1.15	-	1.10	-
$^{176}\text{Lu}(n,\gamma)$	1.26	-	1.21	-	-	-	-	-
$^{115}\text{In}(n,\gamma)$	1.08	-	1.14	-	1.02	-	1.05	-
$^{115}\text{In}(n,n')$	1.47	-	1.35	-	1.30	-	1.19	-
$^{115}\text{In}(n,2n)+$ $^{113}\text{In}(n,\gamma)$	1.58	-	1.07	-	1.95	-	1.28	-
$^{27}\text{Al}(n,\alpha)$	1.37	-	1.37	-	1.31	-	1.43	-
$^{64}\text{Zn}(n,p)$	-	-	-	-	1.12	-	1.05	-
$^{64}\text{Zn}(n,\gamma)$	-	-	-	-	1.12	-	1.12	-

With the view to detailed analysis of the results obtained, the  $^{235}\text{U}(n,f)$  reaction rates in positions "0" and "1" for fuel channel were calculated using formula (17) and Tables 16 and 17:

- 24-18, 28-18, 30-18 (projection X, lattice 21-1-5(M2)),
- 34-14, 34-16, 34-20, 34-22 (projection Y, lattice 21-1-5(M2)),
- 28-18, 30-18, 34-18 (projection X, lattice 21-2),
- 34-14, 34-16, 34-18, 34-20, 34-22 (projection Y, lattice 21-2).

Tables 36 and 37 present the results. For convenience, the tables present also the  $^{63}\text{Cu}(n,\gamma)$  reaction rates from Tables 18-21 and the calculated values of the same reactions. In the case of lattice 21-2 and central channel (34-18), the reaction rates were measured in four positions, namely, "0" and "2" for projection Y; "1" and "3" for projection X.

Table 36. Experimental and calculated  $^{63}\text{Cu}(n,\gamma)$  and  $^{235}\text{U}(n,f)$  reaction rates ( $1/(\text{g}\cdot\text{W}\cdot\text{s})$ ) in lattice 21-1-5(M2) on projections X and Y.

L, cm	$^{63}\text{Cu}(n,\gamma)$		$^{235}\text{U}(n,f)$	
	Calc. R, $10^5$	Experiment ( $R \pm \Delta R$ ), $10^5$	Calc. R, $10^7$	Experiment ( $R \pm \Delta R$ ), $10^7$
Projection X				
24-18 "1"	3.24	2.72±0.06	1.03	0.85±0.03
24-18 "0"	3.71	3.56±0.08	1.24	1.13±0.04
28-18 "1"	5.02	4.94±0.11	1.67	1.56±0.05
28-18 "0"	4.94	4.69±0.10	1.63	1.44±0.05
30-18 "1"	4.86	4.81±0.11	1.59	1.48±0.05
30-18 "0"	5.37	5.10±0.11	1.77	1.54±0.05
Container 4 (96.5 mm)	4.77	5.19±0.16	1.53	1.68±0.05
Container 3 (72 mm)	4.50	4.90±0.15	1.44	1.66±0.06
Container 2 (46.5 mm)	4.28	4.79±0.15	1.37	1.56±0.04
Container 1 (0 mm)	4.15	4.71±0.15	1.33	1.56±0.05
38-18 "0"	5.37	5.10±0.11	1.77	1.54±0.05
38-18 "1"	4.86	4.81±0.11	1.59	1.48±0.05
40-18 "0"	4.94	4.69±0.10	1.63	1.44±0.05
40-18 "1"	5.02	4.94±0.11	1.67	1.56±0.05
44-18 "0"	3.71	3.56±0.08	1.24	1.13±0.04
44-18 "1"	3.24	2.72±0.06	1.03	0.85±0.03
Projection Y				
34-22 "1"	4.60	4.58±0.10	1.54	1.43±0.05
34-22 "0"	4.77	4.54±0.10	1.55	1.42±0.05
34-20 "1"	5.69	4.93±0.11	1.74	1.52±0.05
34-20 "0"	5.22	4.98±0.11	1.62	1.53±0.05
Container 4(96.5 mm)	4.77	5.19±0.16	1.53	1.68±0.05
Container 3(72 mm)	4.50	4.90±0.15	1.44	1.66±0.06
Container 2(46.5 mm)	4.28	4.79±0.15	1.37	1.56±0.04
Container 1 (0 mm)	4.15	4.71±0.15	1.33	1.56±0.05
34-16 "0"	5.38	5.00±0.11	1.63	1.53±0.05
34-16 "1"	5.69	4.96±0.11	1.74	1.51±0.05
34-14 "0"	4.77	4.46±0.10	1.55	1.42±0.05
34-14 "1"	4.60	4.45±0.10	1.54	1.40±0.05

The experimental and calculated  $^{235}\text{U}(n,f)$  and  $^{63}\text{Cu}(n,\gamma)$  reaction rates from Tables 36 and 37 were used to plot their space distributions in lattices 21-1-5(M2) and 21-2 (Figs. 29, 30 and 31, 32, respectively). In the plots, the projection X data are represented symmetrically.

The results obtained indicate that the mean squared deviation factor between the experimental and calculated  $^{235}\text{U}(n,f)$  and  $^{63}\text{Cu}(n,\gamma)$  reaction rates on fuel channels at a 569.75-mm height above the top face of the lower fuel lattice is ranging from 6% to 13%. This fact, as well as the high convergence of the calculated and experimental  $k_{eff}$  values, has made it possible to conclude that the presented experimental data are sufficiently reliable.

Table 37. Experimental and calculated  $^{63}\text{Cu}(n,\gamma)$  and  $^{235}\text{U}(n,f)$  reaction rates (1/(g·W·s)) in lattice 21-2 on projections X and Y.

L, cm	$^{63}\text{Cu}(n,\gamma)$		$^{235}\text{U}(n,f)$	
	Calc. R, $10^5$	Experiment ( $R \pm \Delta R$ ), $10^5$	Calc. R, $10^7$	Experiment ( $R \pm \Delta R$ ), $10^7$
Projection X				
28-18 "1"	5.20	4.84±0.13	1.72	1.59±0.05
28-18 "0"	5.35	4.74±0.13	1.65	1.53±0.05
30-18 "1"	5.35	4.95±0.14	1.65	1.63±0.06
30-18 "0"	5.54	5.42±0.15	1.75	1.70±0.06
Container 4(96.5 mm)	4.87	5.29±0.13	1.55	1.67±0.05
Container 3(72 mm)	4.54	4.90±0.12	1.44	1.55±0.05
Container 2(46.5 mm)	4.17	4.51±0.12	1.32	1.36±0.04
34-18 "3"	3.64	4.08±0.12	1.18	1.24±0.04
34-18 "1"	3.74	4.11±0.12	1.20	1.27±0.05
38-18 "0"	5.54	5.42±0.15	1.75	1.70±0.06
38-18 "1"	5.35	4.95±0.14	1.65	1.63±0.06
40-18 "0"	5.35	4.74±0.13	1.65	1.53±0.05
40-18 "1"	5.20	4.84±0.13	1.72	1.59±0.05
Projection Y				
34-22 "1"	5.37	4.79±0.14	1.70	1.49±0.05
34-22 "1"	4.86	4.79±0.14	1.59	1.50±0.06
34-20 "1"	5.91	5.06±0.15	1.76	1.62±0.06
34-20 "1"	5.38	5.30±0.16	1.63	1.67±0.06
Container 4(96.5 mm)	4.87	5.29±0.13	1.55	1.67±0.05
Container 3(72 mm)	4.54	4.90±0.12	1.44	1.55±0.05
Container 2(46.5 mm)	4.17	4.51±0.12	1.32	1.36±0.04
34-18 "3"	3.81	4.12±0.12	1.23	1.26±0.04
34-18 "1"	3.77	4.22±0.12	1.24	1.28±0.04
34-16 "0"	5.38	5.20±0.14	1.63	1.63±0.06
34-16 "1"	5.91	5.26±0.14	1.76	1.71±0.06
34-14 "0"	4.86	4.78±0.13	1.59	1.49±0.07
34-14 "1"	5.37	4.61±0.13	1.70	1.50±0.05

The experiment-calculation comparison was also made by the conventional techniques, namely, by normalizing all the data to the  $^{235}\text{U}(n,f)$  reaction rate, thereby eliminating most of the possible systematic errors (primarily, the error in determining the MAKET facility power).

Figs. 33 and 34 show the measured reaction rates after normalization to the  $^{235}\text{U}(n,f)$  reaction rate. The calculation-experiment deviations presented in Table 38 have been calculated via formula (40) and show that, given the relative normalization, the experiment-calculation differences for the reactions of well-known cross sections are ranging from 3% to 35%<sup>2</sup>. This fact indicates the identical experiment-calculation convergence for the given two comparison methods, thus indicating the absence of any systematic errors when determining the MAKET facility power. The identical level of the experiment-calculation discrepancy in the actinide reaction rates demonstrated by the two methods is also verification thereof.

<sup>2</sup> The  $^{115}\text{In}(n,2n)+^{113}\text{In}(n,\gamma)$  reaction was disregarded as earlier.



Table 38. The mean squared deviation factors between the experimental and calculated reaction rates (the relative normalization).

Reaction	ENDF/B-VI rev 7.				JENDL-3.2			
	21-1-1-5(M2)		21-2		21-1-1-5(M2)		21-2	
	ITEP	VNIIEF	ITEP	VNIIEF	ITEP	VNIIEF	ITEP	VNIIEF
$^{235}\text{U}(n,f)$	1	1	1	1	1	1	1	1
$^{238}\text{U}(n,\gamma)$	1.05	-	1.10	-	1.08	-	1.20	-
$^{239}\text{Pu}(n,f)$	-	1.10	-	1.18	-	1.09	-	1.18
$^{237}\text{Np}(n,f)$	-	1.26	-	1.21	-	1.09	-	1.00
$^{238}\text{Pu}(n,f)$	-	1.12	-	1.08	-	1.16	-	1.11
$^{240}\text{Pu}(n,f)$	-	1.06	-	1.02	-	1.05	-	1.01
$^{241}\text{Pu}(n,f)$	-	1.16	-	1.11	-	1.15	-	1.11
$^{242\text{m}}\text{Am}(n,f)$	-	1.01	-	1.12	-	1.00	-	1.13
$^{243}\text{Cm}(n,f)$	-	1.15	-	1.01	-	1.01	-	1.17
$^{245}\text{Cm}(n,f)$	-	1.23	-	1.14	-	1.09	-	1.01
$^{247}\text{Cm}(n,f)$	-	1.76	-	1.44	-	1.54	-	1.25
$^{55}\text{Mn}(n,\gamma)$	1.04	-	1.09	-	1.04	-	1.09	-
$^{63}\text{Cu}(n,\gamma)$	1.06	-	1.06	-	1.06	-	1.06	-
$^{197}\text{Au}(n,\gamma)$	1.03	-	1.04	-	1.03	-	1.04	-
$^{176}\text{Lu}(n,\gamma)$	1.10	-	1.15	-	-	-	-	-
$^{115}\text{In}(n,\gamma)$	1.24	-	1.22	-	1.14	-	1.11	-
$^{115}\text{In}(n,n')$	1.30	-	1.31	-	1.15	-	1.15	-
$^{115}\text{In}(n,2n)+$ $^{113}\text{In}(n,\gamma)$	1.85	-	1.12	-	2.26	-	1.38	-
$^{27}\text{Al}(n,\alpha)$	1.23	-	1.29	-	1.21	-	1.35	-
$^{64}\text{Zn}(n,p)$	-	-	-	-	1.23	-	1.04	-
$^{64}\text{Zn}(n,\gamma)$	-	-	-	-	1.03	-	1.07	-

The accuracy requirements of the actinide fission cross sections can be found in Section C.1. Tables 39 (the absolute normalization) and 40 (the relative normalization) present the experiment-calculation differences for thermal and intermediate spectra generated in the SBM in different MAKET facility fuel lattices and obtained using the ENDF/B-VI and JENDL 3.2 libraries.

The tentative analysis (Table 39) of the experiment-calculation differences for two lattices and two normalizations has shown that:

1. the JENDL-3.2 and ENDF/B-VI libraries show about the same preference when used for  $^{235}\text{U}$ ,  $^{238}\text{Pu}$ ,  $^{239}\text{Pu}$ ,  $^{240}\text{Pu}$ ,  $^{241}\text{Pu}$ , and  $^{242\text{m}}\text{Am}$  in both lattices;
2. JENDL-3.2 is more preferable for  $^{237}\text{Np}$  and  $^{247}\text{Cm}$  in both lattices;
3. ENDF/B-VI is more preferable for  $^{238}\text{U}$  in lattice 21-2; both libraries show the identical agreement for  $^{238}\text{U}$  in lattice 21-1-5(M2);
4. it depends on a particular (absolute or relative) normalization if either library is preferred for  $^{243}\text{Cm}$  and  $^{245}\text{Cm}$ . A better agreement with experiment is given by ENDF/B-VI for the absolute normalization and by JENDL-3.2 for the relative normalization.

Any conclusive inference concerning the advantages of ENDF/B-VI and JENDL-3.2 can only be drawn from analyzing the results obtained with the FKBM-2M and BIGR fast-spectrum facilities.

Table 39. Preference in using the ENDF/B-VI and JENDL-3.2 libraries for two lattices in the absolute and relative normalizations.

Reaction	21-1				21-2			
	ENDF/BVI rev 7.		JENDL-3.2		ENDF/BVI rev 7.		JENDL-3.2	
	Abs. Norm.	Rel. norm.	Abs. Norm.	Rel. norm.	Abs. Norm.	Rel. norm.	Abs. Norm.	Rel. norm.
$^{235}\text{U}(n,f)$	+		+		+		+	
$^{238}\text{U}(n,\gamma)$	+	+	+	+	+	+	-	-
$^{239}\text{Pu}(n,f)$	+	+	+	+	+	+	+	+
$^{237}\text{Np}(n,f)$	-	-	+	+	-	-	+	+
$^{238}\text{Pu}(n,f)$	+	+	+	+	+	+	+	+
$^{240}\text{Pu}(n,f)$	+	+	+	+	+	+	+	+
$^{241}\text{Pu}(n,f)$	+	+	+	+	+	+	+	+
$^{242\text{m}}\text{Am}(n,f)$	+	+	+	+	+	+	+	+
$^{243}\text{Cm}(n,f)$	+	-	-	+	+	+	-	-
$^{245}\text{Cm}(n,f)$	+	-	-	+	+	-	-	+
$^{247}\text{Cm}(n,f)$	-	-	+	+	-	-	+	+

Table 40. Differences between the MAKET facility experimental data and the calculation results obtained with the ENDF/B-VI and JENDL 3.2 libraries (the absolute normalization).

Actinide	The found calculation-experiment difference (%); ENDF/B-VI / JENDL 3.2	The accuracy required by applications, %		Conformity of accuracy with application
$^{235}\text{U}$	16 / 15	RB*	0.2-0.3	- / -
		NR**		- / -
		RT***		- / -
$^{238}\text{U}$	15 / 15	RB	10	- / -
		NR	10	- / -
		RT	5	- / -
$^{239}\text{Pu}$	15 / 15	RB	0.5	- / -
		NR		- / -
		RT		- / -
$^{237}\text{Np}$	45 / 12	RB	10	- / -
		NR	10	- / -
		RT	5	- / -
$^{238}\text{Pu}$	7 / 4	RB	10	+ / +
		NR	10	+ / +
		RT	5	- / +
$^{240}\text{Pu}$	13 / 14	RB	10	- / -
		NR	10	- / -
		RT	5	- / -
$^{241}\text{Pu}$	4 / 4	RB	10	+ / +
		NR	10	+ / +
		RT	5	+ / +
$^{242\text{m}}\text{Am}$	24 / 24	RB	20	- / -
		NR	10	- / -
		RT	5	- / -
$^{243}\text{Cm}$	10 / 27	RB	50	+ / +
		NR	10	+ / -
		RT	5	- / -
$^{245}\text{Cm}$	2 / 12	RB	50	+ / +
		NR	10	+ / -
		RT	5	+ / -
$^{247}\text{Cm}$	36 / 19	RB	50	+ / +
		NR	10	- / -
		RT	5	- / -

\* Researches into radiation balance of nuclear power production; prediction of variations in the radiation properties of fuel in the thermal and fast reactors and in the ADS facilities.

\*\* Designing nuclear reactors with side transmutation of minor actinides (i.e., as small addends to reactor core, 1-3% of the prime fuel mass).

\*\*\* Designing and studying the job-oriented reactors (transmuters), whose fuel consists mostly of minor actinides (fast reactors and ADS facilities).

Table 41. Differences between the MAKET facility experimental data and the calculation results obtained with the ENDF/B-VI and JENDL 3.2 libraries (the relative normalization).

Actinide	The found calculation-experiment difference (%); ENDF/B-VI / JENDL 3.2	The accuracy required by applications, %		Conformity of accuracy with application
$^{235}\text{U}$	- / -	RB NR RT	0.2-0.3	+ / + + / + + / +
$^{238}\text{U}$	8 / 14	RB NR RT	10 10 5	+ / - + / - - / -
$^{239}\text{Pu}$	14 / 14	RB NR RT	0.5	- / - - / - - / -
$^{237}\text{Np}$	24 / 5	RB NR RT	10 10 5	- / + - / + - / +
$^{238}\text{Pu}$	10 / 14	RB NR RT	10 10 5	+ / - + / - - / -
$^{240}\text{Pu}$	4 / 3	RB NR RT	10 10 5	+ / + + / + + / +
$^{241}\text{Pu}$	14 / 13	RB NR RT	10 10 5	- / - - / - - / -
$^{242\text{m}}\text{Am}$	7 / 7	RB NR RT	20 10 5	+ / + + / + - / -
$^{243}\text{Cm}$	8 / 10	RB NR RT	50 10 5	+ / + + / + - / -
$^{245}\text{Cm}$	19 / 6	RB NR RT	50 10 5	+ / + - / + - / +
$^{247}\text{Cm}$	60 / 40	RB NR RT	50 10 5	- / + - / - - / -

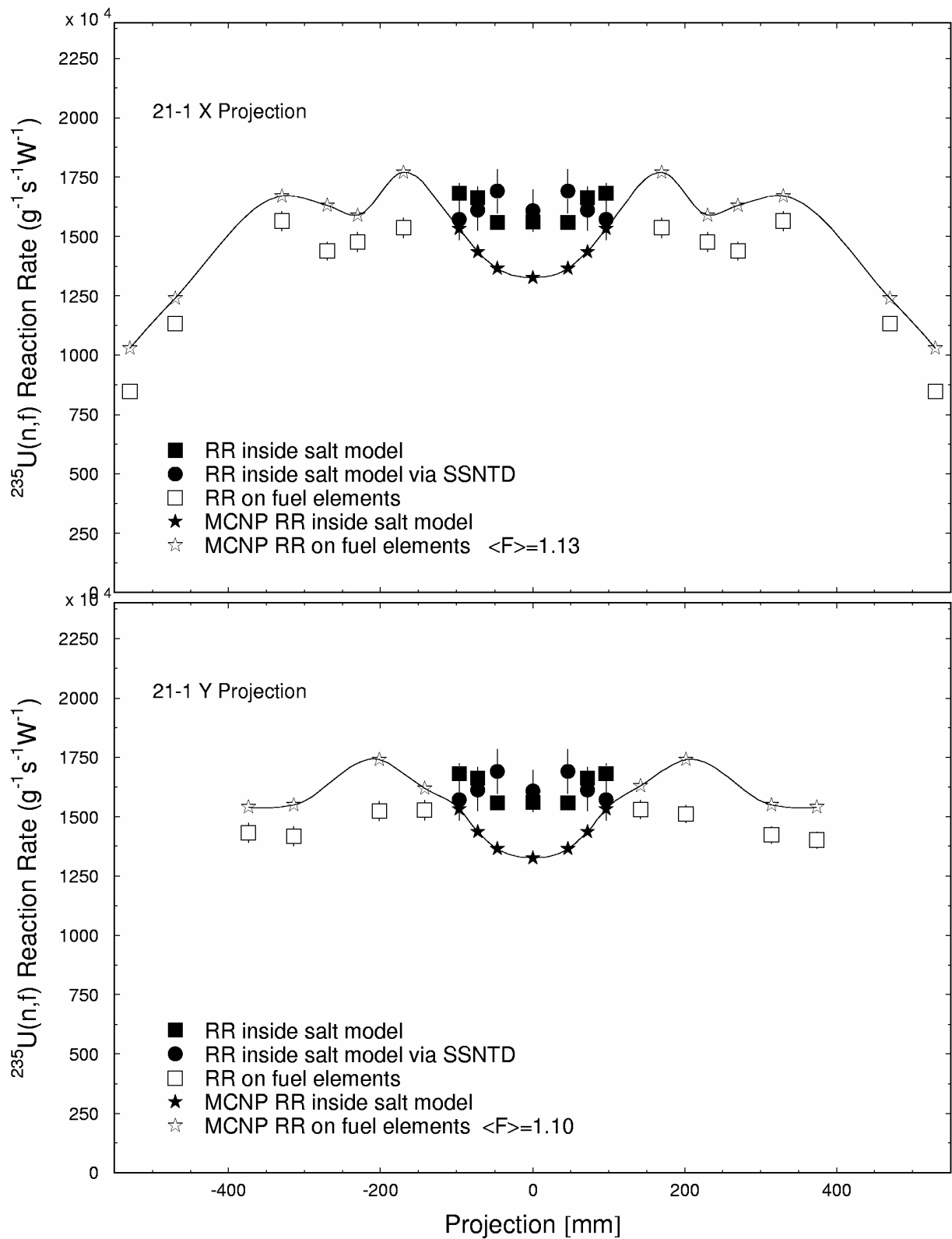


Fig. 29. The  $^{235}\text{U}(n,f)$  reaction rate distributions in lattice 21-1.

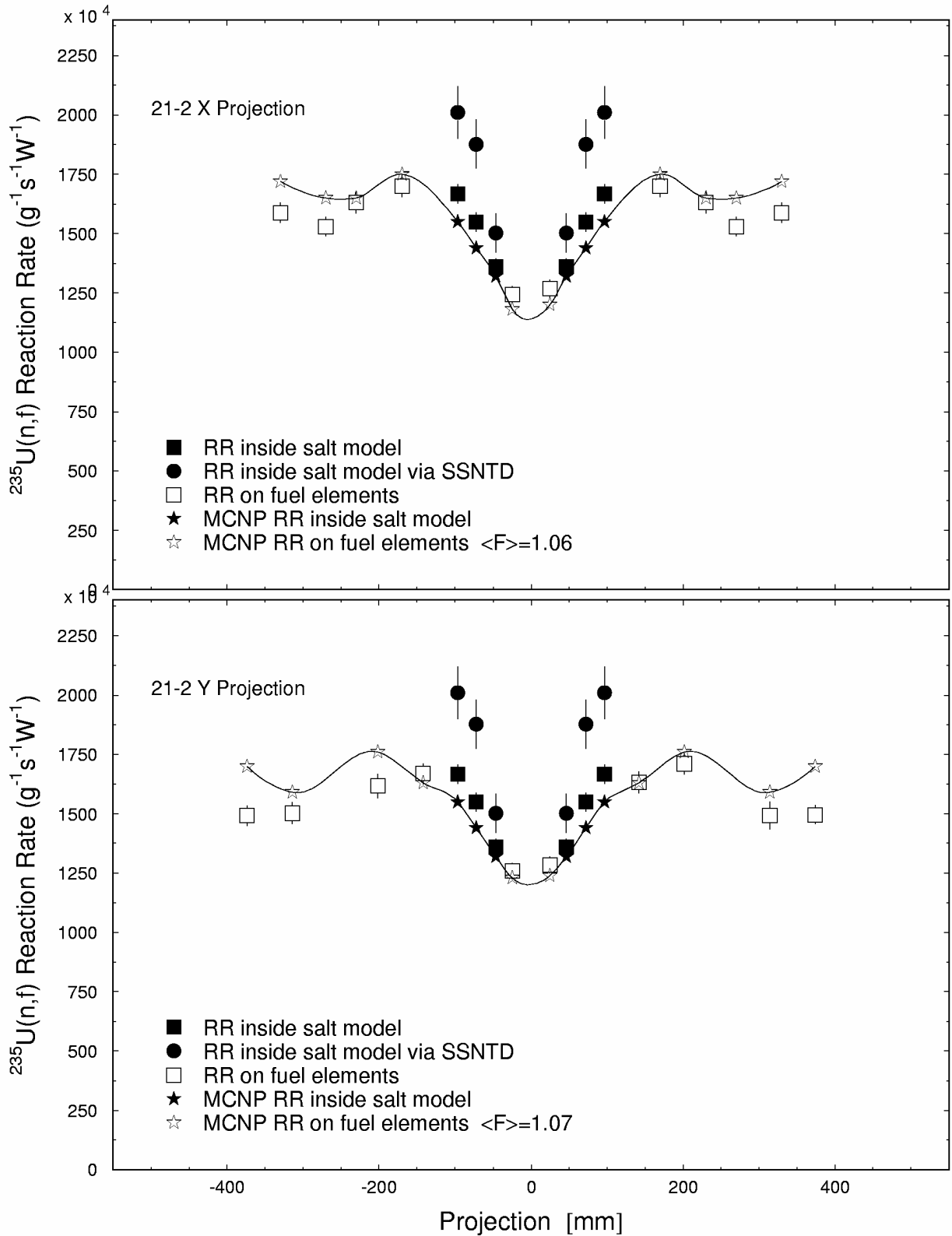


Fig. 30. The  $^{235}\text{U}(n,f)$  reaction rate distributions in lattice 21-2.

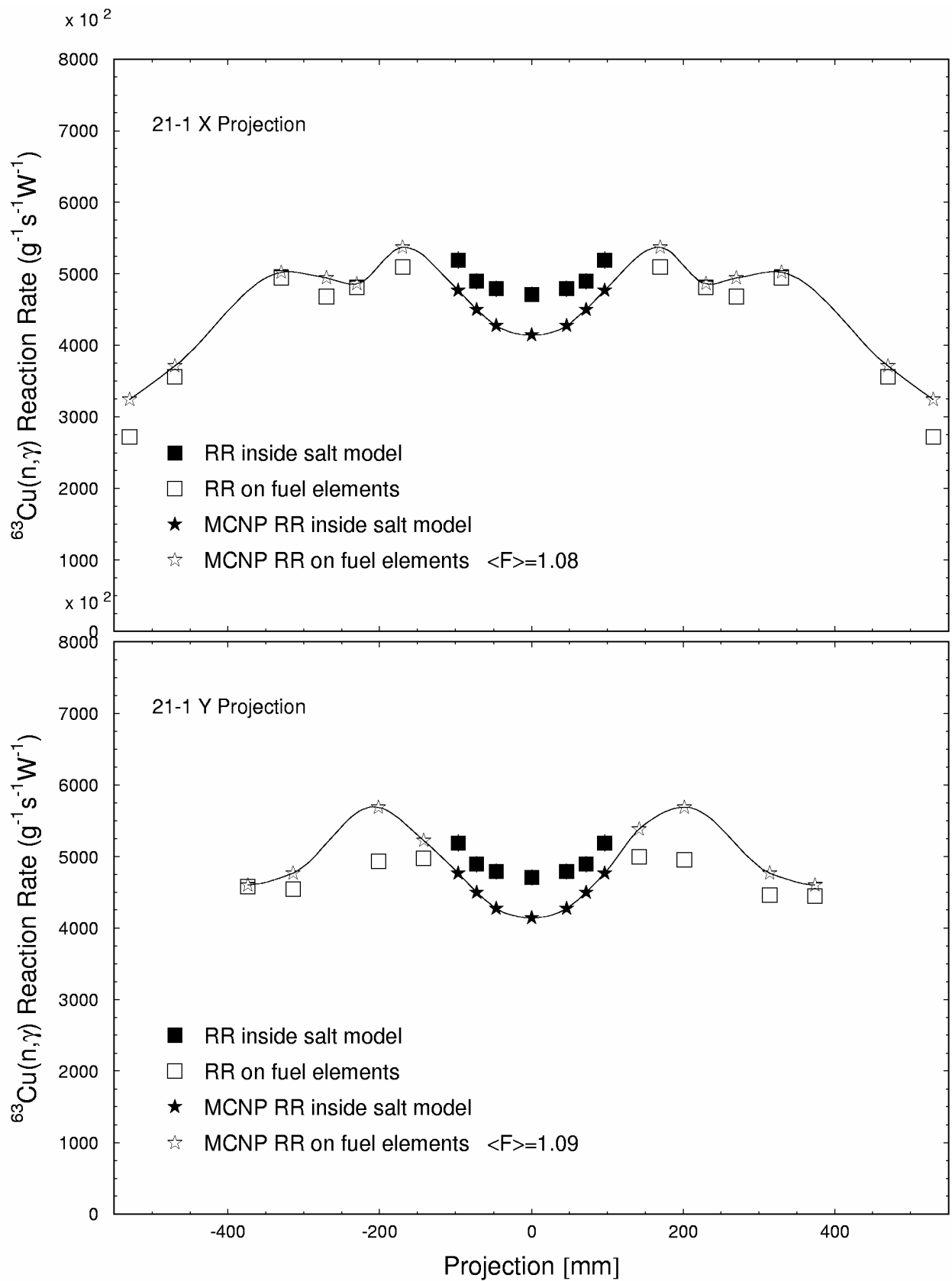


Fig. 31. The  $^{63}\text{Cu}(n,\gamma)$  reaction rate distributions in lattice 21-1.

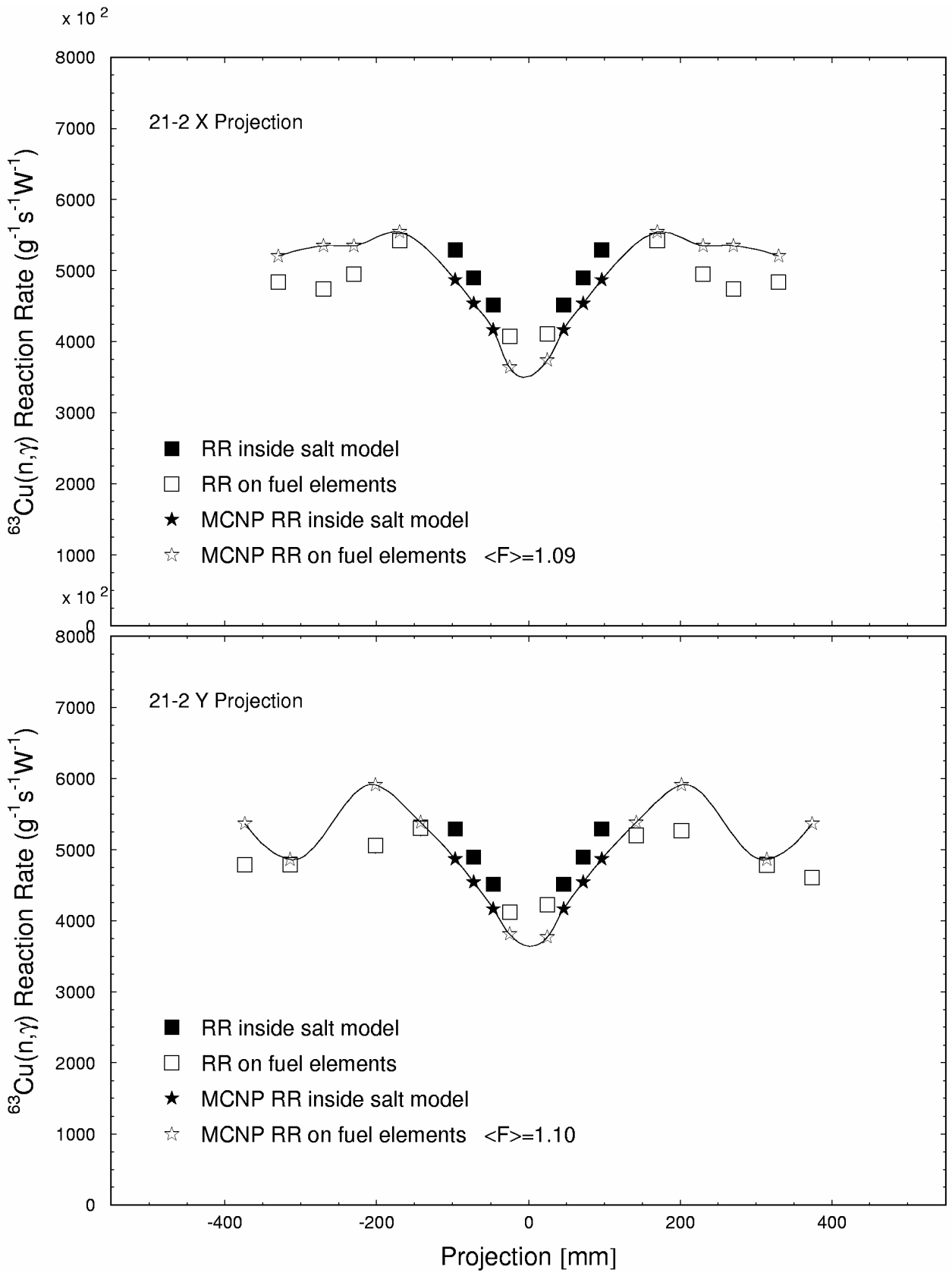


Fig. 32. The  $^{63}\text{Cu}(n,\gamma)$  reaction rate distributions in lattice 21-2.



### 21-1 Lattice

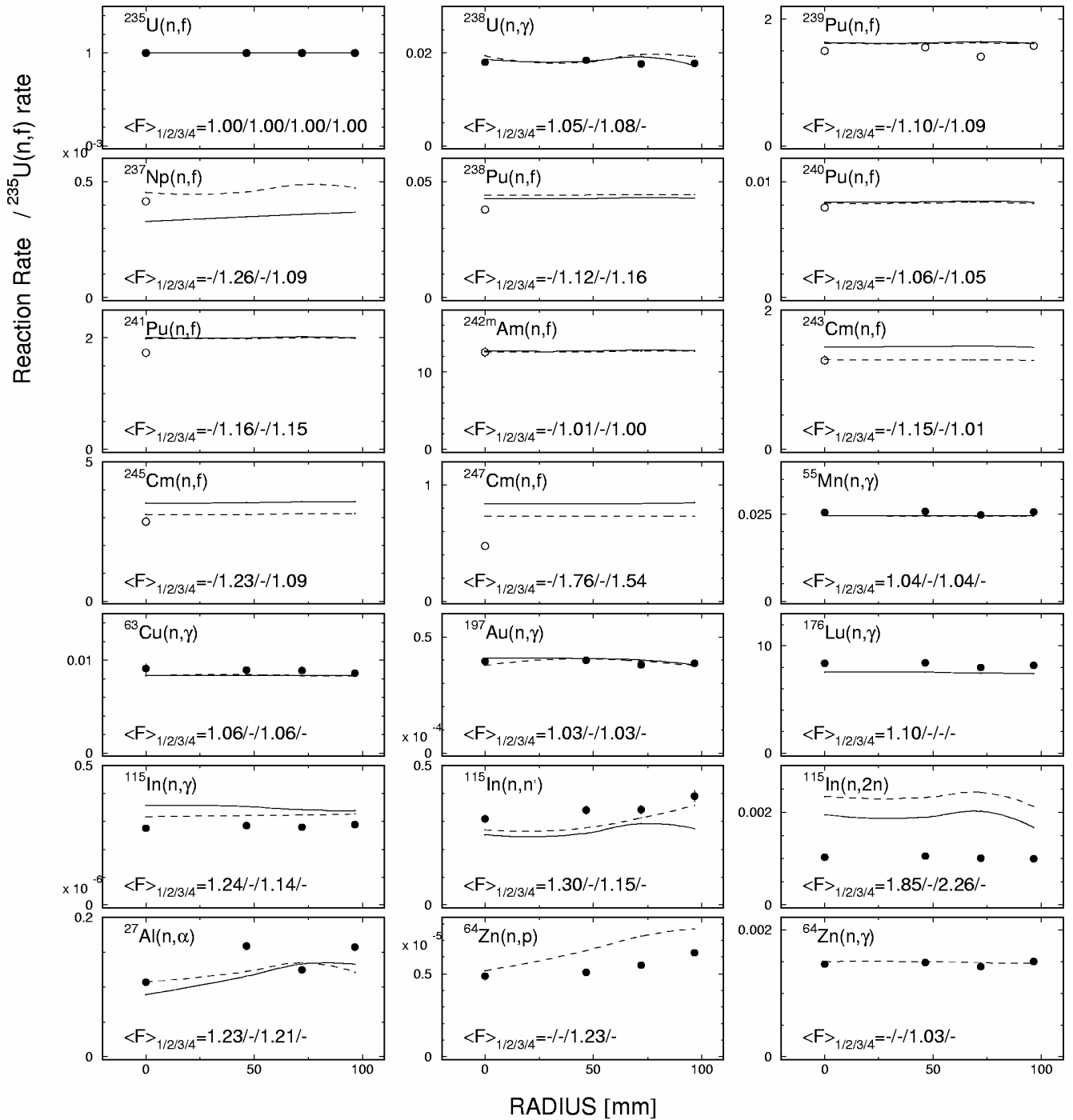


Fig. 33. The MAKET-measured and calculated reaction rates in the lattice with salt insert in central channel after normalizing to the  $^{235}\text{U}(n,f)$  reaction rate at the respective points. The black circles are the ITEP data. The light circles are the VNIIEF data. The dashed lines are the JENDL-3.2 –based calculations. The solid lines are the ENDF/B-VI–based calculations.  $\langle F \rangle_{1/2/3/4}$  are the experiment-calculation mean square deviation factors, where  $\langle F \rangle_1$  is the ITEP experiment- ENDF/B-VI calculation difference;  $\langle F \rangle_2$  is the VNIIEF experiment- ENDF/B-VI calculation difference;  $\langle F \rangle_3$  is the ITEP experiment- JENDL-3.2 calculation difference;  $\langle F \rangle_4$  is the VNIIEF experiment- JENDL-3.2 calculation difference. The gaps indicate lack of the appropriate experimental or calculated results.

## 21-2 Lattice

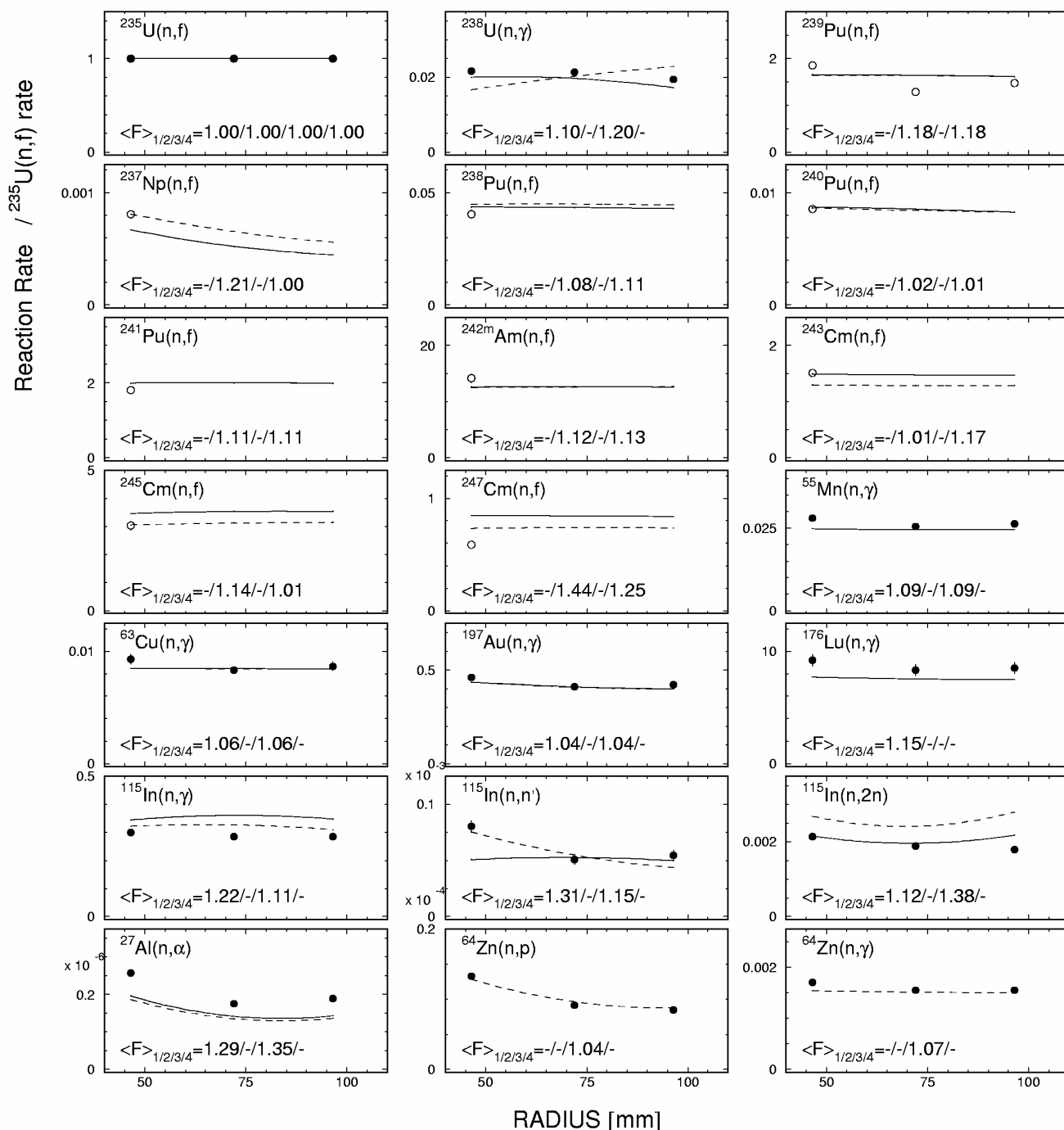


Fig. 34. The MAKET-measured and calculated reaction rates in the lattice with fuel elements in central channel after normalizing to the  $^{235}\text{U}(n,f)$  reaction rate at the respective points. The black circles are the ITEP data. The light circles are the VNIIEF data. The dashed lines are the JENDL-3.2 –based calculations. The solid lines are the ENDF/B-VI–based calculations.  $\langle F \rangle_{1/2/3/4}$  are the experiment-calculation mean square deviation factors, where  $\langle F \rangle_1$  is the ITEP experiment- ENDF/B-VI calculation difference;  $\langle F \rangle_2$  is the VNIIEF experiment- ENDF/B-VI calculation difference;  $\langle F \rangle_3$  is the ITEP experiment- JENDL-3.2 calculation difference;  $\langle F \rangle_4$  is the VNIIEF experiment- JENDL-3.2 calculation difference. The gaps indicate lack of the appropriate experimental or calculated results.

## 15. Certification of fuel

Prior to experimenting, some job-oriented operations were undertaken to certify the fuel elements. The in-situ certification was necessary because of the following.

In fact, the ITEP received a standard lot of experimental fuel elements composed of a definite number of cargo containers with a definite number of fuel elements. The manufacturer's certificate gives sufficiently accurate information on the quantity of fissile nuclear materials (FNM) in the lot as the whole. Therefore, the FNM content of each of the fuel elements could only be taken on an average, as inferred from dividing the total FNM lot quantity by the number of fuel elements in the cargo lot. Since but a fraction of the fuel element total was used in forming the lattices, the averaging was fraught with significant errors of determining the FNM content of each separate fuel element. The tentative measurements confirmed the problem. Thus, a necessity arose for the FNM contents of the fuel elements to be certified in-situ.

The problem was chosen to resolve by non-destructive test analysis. The analysis was made using the CANBERRA U-Pu InSpector spectrometric equipment and the purpose-oriented standards of uranium mass and uranium isotopic composition in fuel elements certified by the gravimetry and mass-spectrometry techniques. The following standard characteristics were certified: the  $^{235}\text{U}$  mass expressed in grams and the  $^{234}\text{U}$ ,  $^{235}\text{U}$ , and  $^{238}\text{U}$  atomic fractions of U expressed in per cent.

The geometric dimensions of the standards were the same as those of the fuel elements.

The U-Pu InSpector spectrometric equipment included:

- ◇ A low-energy Ge detector (LEGe) mounted on a portable cryostat.
- ◇ The U-Pu InSpector portable spectrometric workstation (a many-channel analyzer).
- ◇ A laptop to control the experiment and to process data.
- ◇ A stand (holder) to preserve the fixed geometry of the mutual LEGe-fuel element position.

The stand was to safely align a fuel element with respect to the detector and to permit vertical displacement of the fuel element, with the fuel element bottom-detector top distance being 10-mm stepwise variable from 40 mm to 600 mm. Besides, the fuel element could be kept fixed or turned about its length axis to exclude the effect of U non-uniformity over the fuel element volume.

The number of  $^{235}\text{U}$  nuclei was determined by the most intensive  $^{235}\text{U}$  185.7 keV  $\gamma$ -line. The  $^{235}\text{U}$  mass in the fuel elements and the mass determination error were calculated as

$$M = M_{st} \times \frac{S}{S_{st}}$$

$$\frac{\Delta M}{M} = \sqrt{\left(\frac{\Delta M_{st}}{M_{st}}\right)^2 + \left(\frac{\Delta S_{st}}{S_{st}}\right)^2 + \left(\frac{\Delta S}{S}\right)^2}$$

$M$  - is the  $^{235}\text{U}$  mass in a fuel element;

$\Delta M$  is the error of the  $^{235}\text{U}$  mass in a fuel element;

$M_{st}$  is the  $^{235}\text{U}$  mass in the standard;

$\Delta M_{st}$  is the error of the  $^{235}\text{U}$  mass in the standard;

$S_{st}$  is the counting rate in the 185.7 keV total absorption peak of the standard

$\Delta S_{st}$  is the counting rate error in the 185.7 keV total absorption peak of the standard;

$S$  is the counting rate in the 185.7 keV total absorption peak of a fuel element;

$\Delta S$  is the counting rate error in the 185.7 keV total absorption peak of a fuel element.

Table 42 presents the results of certifying the fuel elements used to form the fuel lattices.

Table 42. Results of certifying the fuel.

Channel	$^{235}\text{U}$ mass $M \pm \Delta M$ , (g)	The greatest deviation from the mean, %	The least deviation from the mean, %
24-18	92.66±0.20	2.05	1.92
28-18	92.74±0.20	1.96	1.40
29-17	91.95±0.20	1.62	1.16
29-19	92.78±0.20	2.78	3.69
30-16	92.78±0.20	2.09	2.57
30-18	91.83±0.20	2.09	1.37
30-20	91.88±0.20	3.53	1.44
31-15	90.85±0.20	1.73	2.22
31-17	92.37±0.20	2.02	2.65
31-19	90.68±0.20	3.40	4.28
31-21	92.95±0.20	3.80	2.92
32-16	91.63±0.20	2.67	1.17
32-20	91.08±0.20	1.42	1.68
33-15	92.18±0.20	1.80	2.10
33-21	92.05±0.20	1.87	2.84
34-14	92.10±0.20	2.67	3.15
34-16	91.66±0.20	1.42	3.38
34-18	90.60±0.20	2.81	4.58
34-20	92.14±0.20	2.54	3.36
34-22	92.17±0.20	2.59	1.66
35-15	92.36±0.20	2.82	2.21
35-21	91.91±0.20	2.54	3.73
36-16	91.83±0.20	2.45	3.04
36-20	92.31±0.20	2.78	1.81
37-15	91.27±0.20	2.82	4.37
37-17	92.42±0.20	1.97	2.01
37-19	92.80±0.20	2.24	1.55
37-21	92.65±0.20	2.23	2.00
38-16	91.84±0.20	1.05	3.68
38-18	91.36±0.20	1.93	2.28
38-20	91.65±0.20	3.35	1.10
39-17	91.02±0.20	3.01	3.05
39-19	92.39±0.20	3.84	2.75
40-18	91.74±0.20	4.73	3.55
44-18	92.42±0.20	2.75	3.48

The tabulated parameters, namely

- ◇ the total  $^{235}\text{U}$  mass of each fuel element and

- ◇ the greatest and least deviations (in %) from the mean  $^{235}\text{U}$  mass in the  $i$ -th fuel element,

demonstrate that the reactor core composition is uniform.

The total  $^{235}\text{U}$  load is  $3128.4 \pm 1.1$  g (34 channels) in lattice 21-1-5M(2) and  $3034.0 \pm 1.1$  g (33 channels) in lattice 21-2.

Table 43 presents the isotopic composition of U in the fuel elements.

Table 43. Isotopic composition of uranium.

Isotope	$^{234}\text{U}$	$^{235}\text{U}$	$^{236}\text{U}$	$^{238}\text{U}$
Atomic fraction in uranium, %	$0.72 \pm 0.01$	$90.05 \pm 0.05$	$0.13 \pm 0.01$	$9.09 \pm 0.03$

### References

- [1] Yu.E. Titarenko, O.V. Shvedov, M.M. Igumnov, E.I. Karpikhin, V.F. Batyaev, V.I. Volk, A.Yu. Vakhrushin, S.V. Shepelkov, A.V. Lopatkin, S.G. Mashnik, T.A. Gabriel. Experimental Determination of the Resonance Integral for  $^{237}\text{Np}$  in a Heavy Water Solution. Nucl. Sci. Eng., vol. 131, No. 1, 96-106, 1999.
- [2] Yu.E. Titarenko, O.V. Shvedov, M.M. Igumnov, E.I. Karpikhin, V.F. Batyaev, A.V. Lopatkin, V.I. Volk, A.Yu. Vakhrushin, S.V. Shepelkov, S.G. Mashnik, and T.A. Gabriel. Experimental Determination and Simulation of the Reactivity Effects and Reaction Rate Sensitivity to Different Ranges of Neutron Energy in Homogeneous Heavy Water Solutions of Thorium. Nucl. Sci. Eng., Vol. 130, No. 2, 165-180, 1998.
- [3] Model S502, Genie-2000 Basic Spectroscopy Software. V1.2A Russian; Model S561, Genie-2000 Batch Programming Support. V1.1.
- [4] R.R. Kinsey, et. al., Proc. 9th Int. Symp. of Capture-Gamma-Ray Spectroscopy and Related Topics, 8-12 October 1996, Budapest, Hungary.
- [5] V.D. Sevastyanov, G.N. Maslov, Yu.V. Permyakov. Development of methods for quality tests and certification of the standard fissile material samples, Izmeritelnaya Tekhnika (in Russian), No.9, 65-67, 1997.
- [6] V.D. Sevastyanov, V.I. Lyagushin, Methods for certifying the standard  $^{235}\text{U}$ ,  $^{238}\text{U}$ , and  $^{237}\text{Np}$  samples with a  $0.5\text{-}3$  mg/cm<sup>2</sup> target nuclide thickness, Izmeritelnaya Tekhnika (in Russian), No.11, 56-59, 1997.
- [7] M.T. Meek and B.R. Rider. Compilation of Fission Product Yields, NEDO-12154-2, Vallecitor Nuclear Center, 1977.
- [8] MCNP-4B, Manual, LA-12625M, 1997.
- [9] ENDF/B-VI rev.7 - IAEA-NDS-100 Rev.6.
- [10] JENDL-3.2 - IAEA-NDS-169 Rev.2.
- [11] R.E. MacFarlane and D.W. Muir. The NJOY Nuclear Data Processing System Version 91, LA-12740-M (October 1994). R.E. MacFarlane, "README": NJOY 94.66(105)", 1997.
- [12] R.E. MacFarlane. New Thermal Neutron Scattering Files for ENDF/B-VI Release 2, La-12639-MS, 1994.
- [13] International Handbook Of Evaluated Criticality Safety Benchmark Experiments, Nea/Nsc/Doc(95), 1997.

---

Nuclear Data Section  
International Atomic Energy Agency  
Vienna International Centre, P.O. Box 100  
A-1400 Vienna  
Austria

e-mail: [services@iaeand.iaea.org](mailto:services@iaeand.iaea.org)  
fax: (43-1) 26007  
telephone: (43-1) 2600-21710  
Web: <http://www-nds.iaea.org>

---